UNIVERSITÀ DEGLI STUDI DI PADOVA

DIPARTIMENTO DI SCIENZE CHIMICHE

CORSO DI LAUREA MAGISTRALE IN CHIMICA

TESI DI LAUREA MAGISTRALE

LIGHT-HARVESTING EUROPIUM ARCHITECTURES: FROM MOLECULES TO FUNCTIONAL MATERIALS FOR VERSATILE LUMINESCENT APPLICATIONS

Relatrice:

Prof.ssa Lidia Armelao

Controrelatrice:

Prof.ssa Elisabetta Collini

Laureanda:

Maria Francesca Cherchi

Anno Accademico 2023-2024

Abstract

The present thesis is dedicated to the synthesis of europium-based luminescent antenna complexes and oxoclusters and to their intriguing photonic applications, peculiarly triggered by ultraviolet photons. Specifically, their photophysical behaviour raises them as eligible candidates for contactless Luminescent Molecular Thermometers (LMTs) and for the currently blooming Luminescent Solar Concentrators (LSCs) scenario.

To this purpose, a pentanuclear Eu^{3+} oxocluster, whose stoichiometry is described by $Eu_5(DBM)_{10}(OH)_5$, where DBM indicates the β-diketonate ligand dibenzoylmethanide, was synthesized and crystallographically isolated.

Additionally, two discrete monometallic analogues, one consisting of $Eu(DBM)_3(H_2O)_2$ and the other of $Eu(DBM)_3(DME)$, where DME represents the ancillary bischelate dimethoxyethane, were prepared in order to compare their luminescent features with the increasing number of metallic atoms in the inner core.

The project is then declined into other three phases, namely the characterization of the realized luminescent molecules, their optimized embedding into PMMA matrix for the development of photoluminescent hybrid materials in a thin film configuration and, finally, the probing of their spectroscopical and functional responses. These latter aspects encompassed testing all the doped red-emitting films for their luminescence-temperature correlation properties and performance as LSC devices.

Exploring the temperature interval from 83 to 333 K, the relative thermal sensitivity parameter, S_r, exhibited values major than 1 (generally assumed as a quality criterion for these thermometers) approximately from 220 K to the end of the investigated thermal operative range, thus embracing the physiological temperature window.

Furthermore, the electrical outputs of silicon photovoltaic cells, edge-coupled to the LSC perimeter, are evaluated under simulation of solar irradiation.

Although further work is necessary to glean a deeper comprehension, these preliminary studies pave the way for the potential exploitation of dibenzoylmethanide Eu^{3+} systems for temperature sensing and as active components for LSCs, without noticing strong deviations among the investigated species' performances.

Index

Acronyms and abbreviations

α-AA	α-Amino Acid
abzm	di(4-allyloxy)benzoylmethanide
acac	acetylacetonato
AM1.5G	Air Mass 1.5 Global
ATR	Attenuated Total Reflectance
AVT	Average Visible Transmittance
ba	benzoate
BE	Binding Energy
BEnT	Back Energy Transfer
BIPV	Building Integrated Photovoltaics
bpy	2,2'-bipyridine
btfa	benzoyltrifluoroacetonate
CCD	Charge Coupled Device
CIELAB	*Commission Internationale de l'Eclairage,* L*a*b*
CRI	Colour Rendering Index
DBM	Dibenzoylmethanide
DME	Dimethoxyethane
DMF	Dimethylformamide
dpbp	4,4'-bis(diphenylphosphoryl)biphenyl
Em	Emission
ESI-MS	Electrospray Ionization Mass Spectrometry
Et	Ethyl
ET	Energy Transfer
Exc	Excitation
fba	2-fluorobenzoate
FF	Fill Factor
FT-IR	Fourier Transform Infrared
g	glyme
HDBM	Dibenzoylmethane
hfa	1,1,1,5,5,5-hexafluoropentane-1,4-dione
ILCT	Intra-Ligand Charge Transfer

hmp	2-(hydroxymethyl)pyridine
IR	Infrared
ISC	Inter System Crossing
LED	Light-Emitting Diode
LMCT	Ligand-to-Metal Charge Transfer
LMT	Luminescent Molecular Thermometer
LnTOC	Lanthanide-Titanium-Oxo Clusters
LSC	Luminescent Solar Concentrator
lum	luminophore
MIR	Middle Infrared
MOF	Metal Organic Framework
NIR	Near Infrared
NP	Nanoparticle
OAc	Acetate
OC	Open Circuit
O^{i}Pr	isopropoxide
ORTEP	Oak Ridge Thermal Ellipsoid Plot
O^{t}Bu	tert-Butoxide
PCE	Power Conversion Efficiency
PeT	Photoinduced electron Transfer
phen	1,10-phenanthroline
PL	Photoluminescence
PLE	Photoluminescence Excitation
PMMA	Polymethylmethacrylate
PV	Photovoltaic
pyrzMO	pyrazine *N*-oxide
QD	Quantum Dot
SC	Short Circuit
SC-XRD	Single Crystal X-ray Diffraction
SE	Sensitized Emission
SMU	Source Measure Unit
tbza	4-tert-butylbenzoic acid
THF	Tetrahydrofuran
TIR	Total Internal Reflection

TSP	Temperature Sensitive Paint
tta	thenoyltrifluoroacetylacetonate
Tyr	Tyrosine
UV	Ultraviolet
Vis	Visible
w	water
XPS	X-ray Photoemission Spectroscopy

CHAPTER I

Introduction

1.1. The aggregation of lanthanide ions into multinuclear hydroxo- and oxo-clusters

An extensive body of literature highlights the vast amount of research on luminescent lanthanide-based architectures with a declination spanning from monometallic and monomeric complexes until molecular frameworks and nanoparticles.[1, 2]

In this perspective, it is collocated the flourishing family of luminescent oxo- and hydroxo-cluster aggregates which, along with their discrete mononuclear counterparts, are generally implemented as optical unit into numerous photo-functional materials.[3, 4, 5] Accordingly, they have been destined for an abundance of applicative fields, like light-powered and electroluminescent devices and displays,[6] temperature sensing,[7] cell imaging,[8] molecular magnetism,[9] and catalysis.[10]

The idea of expanding the metal ions core to build such larger structures is not a mere pretext for creating more attractive topologies and shapes, but it leads to a new class of luminescent lanthanide systems. These assemblies are constituted of confined and rigid multinuclear metal cores enclosed by an envelope of organic ligands, with variable nuclearities (up to 140 metal ions) and dimensions (up to 6 nm).[11] Figure 1.1 resumes some structures with increasing nuclearity of molecular cluster containing Ln^{III} atoms.

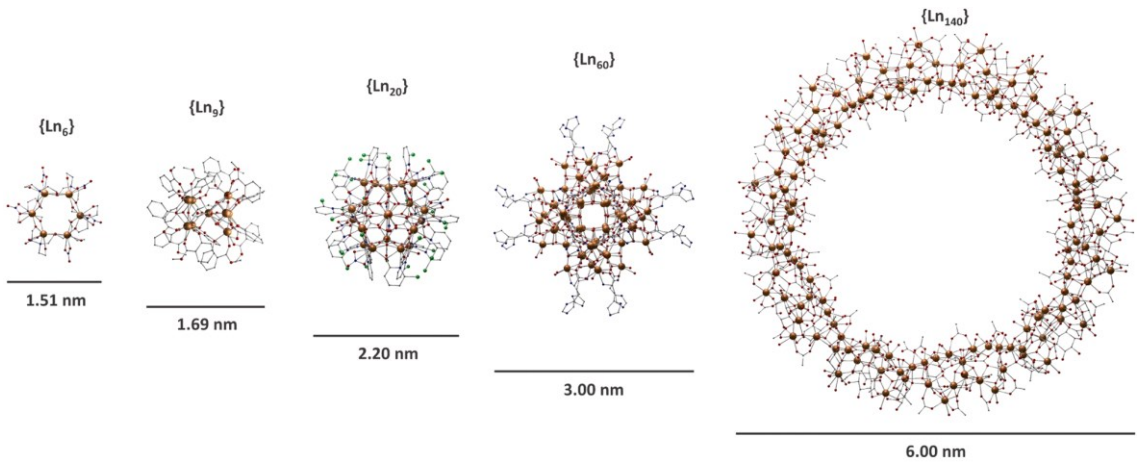

Figure 1.1. Selection of structures with increasing nuclearity of molecular clusters containing Ln^{III} atoms. Depiction redrawn from the review of ref.[12]

Such systems can be structurally viewed as a fruitful interplay between nanoparticles and monometallic molecular complexes. In fact, they can achieve extents comparable to those of nanoparticles while retaining the fine-tunability and uniformity of composition along with size and structure peculiar of molecular complexes.[12]

The synthesis of polynuclear lanthanide hydroxide and oxide complexes has proven to be challenging, since efforts to rationally design them are frequently accompanied by serendipitous self-organization events. As a result, only a limited degree of confidence has been attained in developing predictable and reproducible synthetic protocols.[13]

Certainly, even if their chemistry has not been developed as the one of transition metals clusters, some features can be adjusted by a rational choice of the precursor materials.

For instance, it was noticed that the type of lanthanide and the hindrance and flexibility of the polydentate ligands could somehow define recurrent evidences regarding the core motif,[4] and inhibit uncontrolled polymerization.[14] A library of lanthanide-based clusters have been obtained with a huge variety of shielding ligands: more compact moieties, like carbonates and simple carboxylates,[15,16] tend to articulate in more extended structure, whereas bulkier ones, as functionalized β-diketonates, impart an opposing effect on the amount of metal ions hosted in the cluster core.[14,17] Moreover, experimental conditions, such as the metal:ligand ratio, the choice of the solvent, the duration of the reaction and the nature of the deprotonating agent can influence the final product.

The nuclearity and geometry of the cluster core are also reliant on the ionic radius of the rare-earth ion.[14] Maintaining unaltered the bulkiness of the ligand species, the periodic lanthanoid contraction phenomenon orients the cluster construction towards a differently-membered core, intuitively leading to smaller nuclearities if larger cations are involved.

A systematic investigation of this effect was parallelly provided by Roesky's and Andrews' research groups using the dibenzoylmethane ligand.[14] Ions such as Pr(III), Nd(III) and Sm(III) preferentially afforded a four-membered planar configuration with each ion being nonacoordinated,[18,19] whereas Ho(III), Gd(III), Dy(III), Er(III) and Yb(III) were isolated as eight-coordinated pentanuclear structure.[20,21,22] Thanks to its central position in the *f*-block series, europium is the only element endowed with the borderline behaviour of organizing into either tetranuclear and pentanuclear arrangements.

Following the above-described relationships, a system containing 42 Eu^{3+}, Gd^{3+} and Tb^{3+} ions, together with ligands like acetate and *ortho*-vanillin (here indicated as L), gives the large cyclic nanotoroid $[Ln_{42}L_{14}(OAc)_{82}(OH)_{30}]$,[23] while substituted pyrrole-based polyanions leads to a divalent samarium cluster instead of the pentanuclear core.[24]

For the cluster core, two structural patterns are recurrently encountered: a cubane polyhedron relying on the central tetra-unit $[Ln_4(\mu_3\text{-}OH)_4]^{8+}$ and a square pyramidal shape originated from an ensemble of five *f*-block cations.[3]

Different combinations of these two cores can give more complex aggregates. Formally, the staggered fusion at the apical atom of two square pyramids generates a square antiprism with nonanuclearity, as witnessed by the hourglass-like $[Ln_9(OH)_{10}(hmp)_8(NO_3)_8(DMF)_8](OH)$ compound, where Ln is Dy or Eu and hmp stands for 2-(hydroxymethyl)pyridine.[25]

In turn, a tetradecanuclear polyhedron can be produced connecting two nonanuclear double pyramids, as reported for $[Ln_{14}(\mu_4\text{-}OH)_2(\mu_3\text{-}OH)_{16}(\mu\text{-}\eta^2\text{-}acac)_8(\eta^2\text{-}acac)_{16}]$, where Ln = Tb, Eu and acac = acetylacetonato, in the work of Wang and collaborators.[26]

A schematic depiction of the pentanuclear square pyramid and these two derived structural backbones is showed in Figure 1.2.

With the same logic, the heterocubane unit can be regarded as the building block for templating dodecanuclear or pentadecanuclear- if halide anions are implied - structures (see left edge of Figure 1.2).[3, 27]

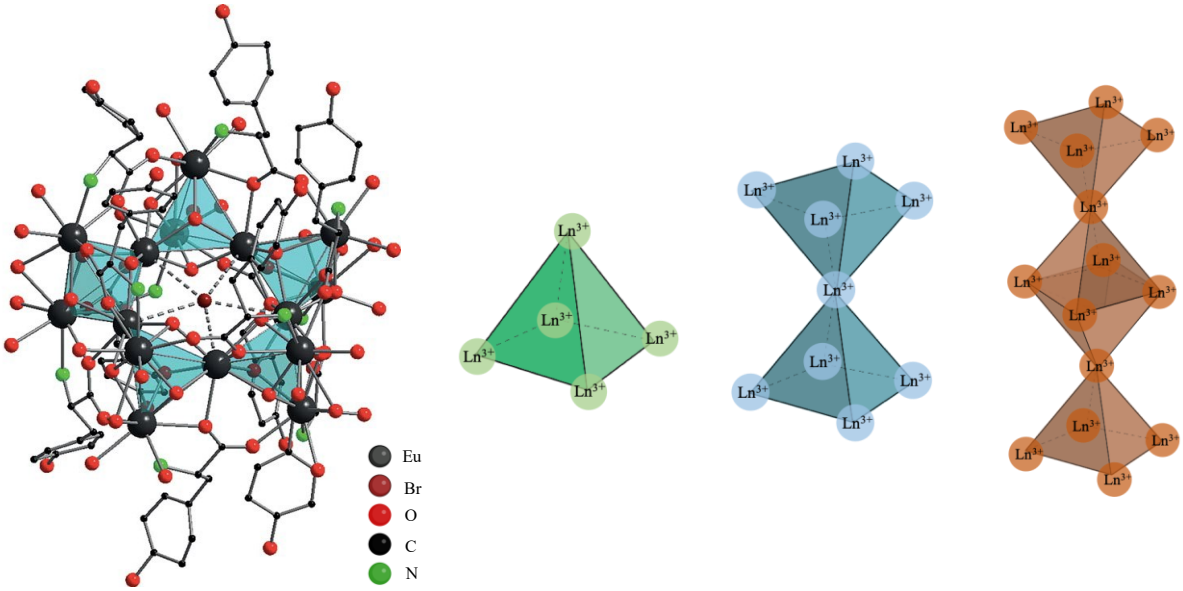

Figure 1.2. On the left part, a perspective view of the crystalline structure of the cation $[Eu_{15}(Cl)(L\text{-}Tyr)_{10}(OH)_{20}(H_2O)_5(OH)_{12}(H_2O)_8]^{2+}$,[27] where Tyr denotes the amino acid tyrosine, taken from ref.[3] Hydrogens, lattice water molecules and perchlorate anions are omitted for clarity. On the right side, an oversimplified vision of how the square pyramidal unit can associate to construct bigger motifs.

There are several evidences, that these single-sized lanthanide hydroxide and oxide clusters develop through a controlled hydrolytic route in basic pH environment even if a precise rationalization of their formation is still missing.[13, 28, 29]

From a historical perspective and similarly to what reported for mononuclear complexes, the most studied chelating group in lanthanoid cluster chemistry is represented by the β-diketonate family.[30]

Among the literature publications, one of the well-established procedures documenting the realization of a homometallic aggregate entails a pentanuclear core encapsulated by the dibenzoylmethane (DBM) chelate. The $[Ln_5(OH)_5(DBM)_{10}]$ cluster was attained for Ln equal to Y,[31] Eu,[20, 32, 33, 34] Tb,[33] Dy,[22] Ho,[20] Er,[20, 21] Yb,[21] while the replication of the synthetic procedure for Pr, Nd and Sm conduced to the tetranuclear cluster version,[18] according to the trend on lanthanide ions' size (these two square pyramidal and cubane motifs are illustrated in Figure 1.3). Remarkably, lanthanum, the bigger trivalent ion of the period, constitutes an exception, leading to a dodecanuclear hydroxo-bridged cluster.[35]

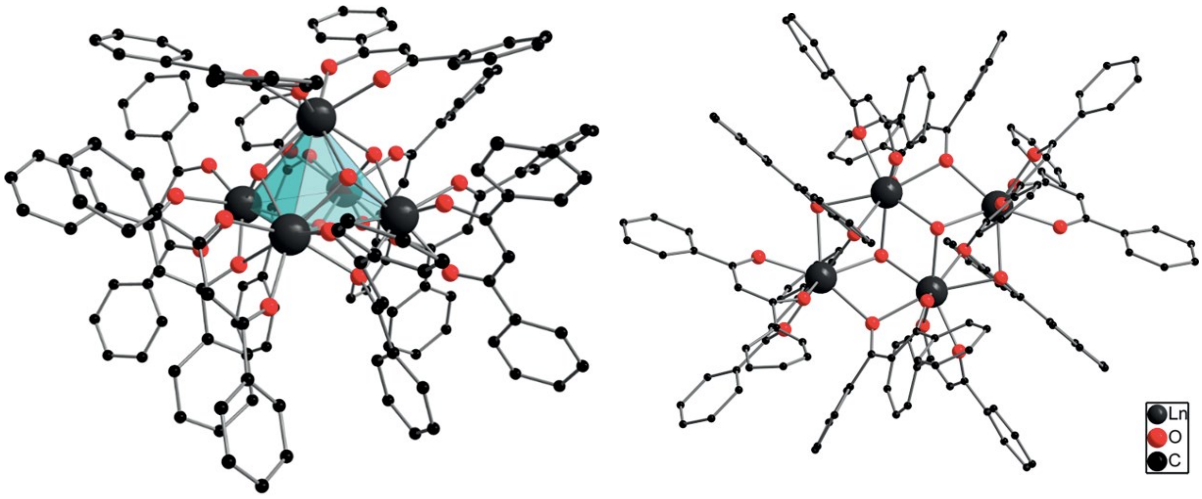

Figure 1.3. Reproduction of the pentanuclear (left side) and tetranuclear (right side) crystal structures found for the generic formulae $[Ln_5(OH)_5(DBM)_{10}]$ and $[Ln_4(OH)_2(DBM)_{10}]$, respectively. Images taken from ref.[38]

Inspired by these quite consolidated results, functionalized alternatives of dibenzoylmethane-based edifices have been proposed through derivatization of this diketonate or selective replacement of some unit of it with diverse polydentate species.[20, 36] To cite, also biologically active entities, like amino acids, have been employed to stabilize square-based pyramidal scaffolds with formula $[Y_5(OH)_5(\alpha\text{-AA})_4(DBM)_6]$, in which the shortening α-AA indicates D-phenyl glycine, L-proline, L-valine and L-tryptophan.[37]

Nevertheless, apart from their facile and more reproducible synthesis, these Ln(III)-dibenzoylmethane clusters have been studied most intensively for their promising physical properties in molecular magnetism.[3]

1.1.1. Towards more complex declinations of lanthanoid-oxo-/hydroxo-clusters

Although homometallic lanthanide-based cluster have been extensively considered since the late 1990s, it was only recently that more sophisticated heterometallic structures were pioneered.[12, 38, 39] The attractiveness of conjugating different lanthanide ions or mixing them with transition metals paved the way to finely tune the emission

colour output and manipulate the energy transfer process which dictates their photophysics.

Among the vastness of core compositions, the emerging branch of lanthanide-titanium-oxo clusters (LnTOCs) gained attention thanks to the possibility, not only of integrating the characteristics of two distinctive elements into a single molecule, but also to exploit their unique synergistic activity.[40]

Structurally, these lanthanide-containing polyoxotitanate cages are founded on a network of Ln–O–Ti bonds (an example of Eu-Ti based cluster is presented in Figure 1.4). The presence of Ti^{4+} is beneficial for the diminution of O–H groups, in turn substituted by O^{2-} bridges between the Ti and Ln centers. This factor impacts on the optical behaviour of these LnTOC systems since the hydroxyl group is a well-known quenching moiety for Ln luminescence.[41]

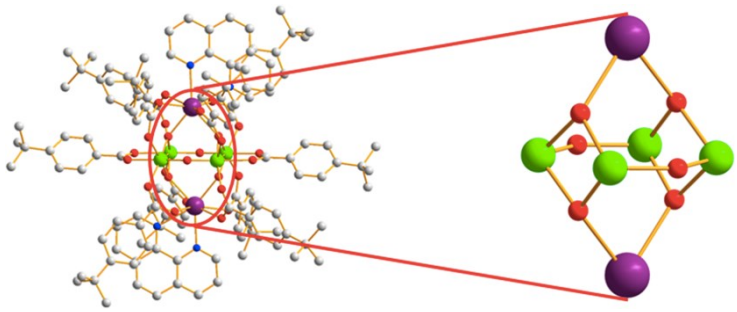

Figure 1.4. Solid-state structure of $[Eu_2Ti_4(\mu_2\text{-}O)_2(\mu_3\text{-}O)_4(phen)_2(tbza)_{10}]\cdot 4CH_3CN$, where phen specifies 1,10-phenanthroline, while tbza the 4-tert-butylbenzoic acid, together with a zoom of its Eu–Ti–O core.[42] Colour cipher: Eu purple, Ti green, O red, C gray and N blue; H atoms have been neglected.

Additionally, their exceptional luminescence performance (a 94.9 % quantum yield was individuated for a $[Eu_5Ti_4(\mu_3\text{-}O)_6(tbba)_{20}(Htbba)(THF)_2]$ species in the solid-state, as one of the highest values tracked for 3*d*-4*f* clusters)[43] is partway justified by the cooperative role acted by Ti^{4+}, as demonstrated in recent articles. Indeed, the lanthanide-titanium oxo core plays a strengthening function in the energy transfer mechanism initiated by the organic chromophore and can lessen the energetic request for Ln^{3+} photoluminescence sensitization (this latter phenomenon will be discussed in the following Chapter 1.2).[44] Actually, Li and collaborators suggested a Ti^{4+}-assisted excitation channel, specifically for $[LnTi_6O_3(O^iPr)_9(salicylate)_6]$ compounds, whose

formula was conceived for the entire series of rare-earth elements excluding Pm: the energy transfer from salicylate toward the *d* orbital of the titanium ion mediates an otherwise inefficient Ln^{3+} sensitization, if operated by the sole carboxylate unit.

To date, the incorporation of such cluster compounds into host matrices[45, 46] has been rarely investigated, in contrast to the more extensive research on mononuclear lanthanide complexes. In this latter case, the ability to preserve and transmit the individual properties of the luminophores within the substratum has proven valuable for applications such as light emitting and optoelectronic,[47] optical encryption,[48] and multitasking technologies.[49]

By blending features derived from both the organic and inorganic components, new functionalities can be integrated within polymeric substance also starting from multinuclear architectures: Andrews and coworkers firstly thought to englobe oxo/hydroxo clusters of the type $[Ln(OH)_5(abzm)_{10}]$, where Ln indicates Eu, Tb, Ho and abzm the di(4-allyloxy)benzoylmethanide ligand, as crosslinking agents for reinforcing mechanical and thermal properties of polymeric media based on PMMA, besides conferring their intrinsic magnetic and optical features to the final material.[45]

It is noteworthy also the study conducted by Hauser *et al.* on luminescent thin films of composite cluster-polymer nanoparticles.[46] Here, the nanoclusters $[Ln_5(OH)_5(DBM)_{10}]$ and $[Ln_4(OH)_2(DBM)_{10}]$ have been processed into different polymeric hosts, imparting to them their distinctive luminescence and being protected from water-based surroundings, so as to be useful for biomedical and optical devices.

Apart from these few studies, a rising call for lanthanide-based multifunctional materials has motivated researchers to pursuit versatile systems able to serve various operations at the same time. The recent advances in comprehending lanthanoid clusters' synthesis, outlined before, are contributing to elect this type of systems as novel candidates in the exploration of innovative hybrid inorganic-organic materials.[50]

1.2. Light-harvesting: the photophysics inside a Ln^{3+}-based luminophore

Trivalent lanthanide ions are recognized for displaying remarkable and unique photophysical properties, much so they have sparked interest in the field of luminescent materials and related applications that require long-lived emission and high color purity.[51] A deeper portrayal of the molecular-level mechanism which rules the

sensitization of their luminescence efficiency is of utmost importance to disentangle the subtle dynamics that elect them for light-associated purposes.

The principal spectroscopic features of *f*-block elements rely on long lifetimes up to milliseconds, large Stokes shifts and atom-like emission half-widths due to their characteristic intraconfigurational *f–f* transitions within their environmentally shielded 4*f* orbitals.[52] Indeed, the perturbation promoted by the ligand field or by the steric surrounding is significantly feebler than the spin-orbit coupling in affecting the electronic structure of rare earth ions;[53] this results in preservation within their complexes of the non-degenerate microstates of the free ion represented by their original term symbols.

Direct excitation of Ln^{III} cations is extremely inefficient and the electronic transitions confined into the 4*f* orbitals are demarcated by little electric dipole strengths.[54] Actually, these radiative transitions are parity-forbidden according to the Laporte's selection rule and, consequently, they manifest intrinsically weak extinction coefficients (around 0.1-10 $M^{-1}\cdot cm^{-1}$).[55]

Since the pivotal study of Weissmann in 1942, who firstly observed the luminescence enhancement of Eu^{III} by coordinating chromophores,[56] efforts have been made to achieve strongly emissive lanthanoid complexes.

According to the so-called *antenna effect* the luminescence of the trivalent ion is indirectly stimulated by a sequence of energy transfer (ET) steps incited by a sensitizer environment, generally a conjugated organic ligand or a photoactive *d*-block metal complex.[57] So as to adequately intensify the Ln^{III} emission, the antenna should possess a high absorption coefficient (ε), an efficient intersystem crossing (ISC) pathway and a triplet excited state having higher energy respect to the accepting manifold of the metal ion. It has been estimated that an energy difference of approximatively 1850-3500 cm^{-1} is sufficient to optimally transfer the energy excess from the surrounding chromophores to the lanthanoid and simultaneously avoid or reduce to a minimum the reverse back energy transfer (BEnT).[58] Indeed, if the feeding excited level of the chromophore approaches the accepting metal level, the excitation can retrace the same route and mechanism as its originating ones.

Unless the details of this photosensitization mechanism are still controversial, it is commonly accepted that it predominantly follows a well-established downhill dynamic.[59] As a consequence of a resonant light absorption, the unsaturated organic moiety is excited to its singlet manifold $^1S_x^*$. A rapid non-radiative relaxation to the

lowest-lying vibrational excited singlet state $^1S_1^*$ arises according to Kasha's rule; subsequently, the excited-state population is moved to the ligand-centered triplet level $^3T^*$ through intersystem crossing (promoted by the strong spin-orbit coupling of the lanthanoid ion) and, ultimately, migrates to the emissive excited state of the lanthanoid center. The light-conversion path is then completed by a spontaneous metal-centered radiative emission (the overall energetic cascade $^0S \rightarrow {}^1S^* \rightarrow {}^3T^* \rightarrow Ln^* \rightarrow Ln$ is resumed in the Jablonski diagram of Figure 1.5).

Both donor-acceptor distance-dependent Förster's multipolar and Dexter's electron exchange type models have been experimentally detected and theoretically modeled as possible channels governing $^3T^* \rightarrow Ln^*$ energy transfer.[60]

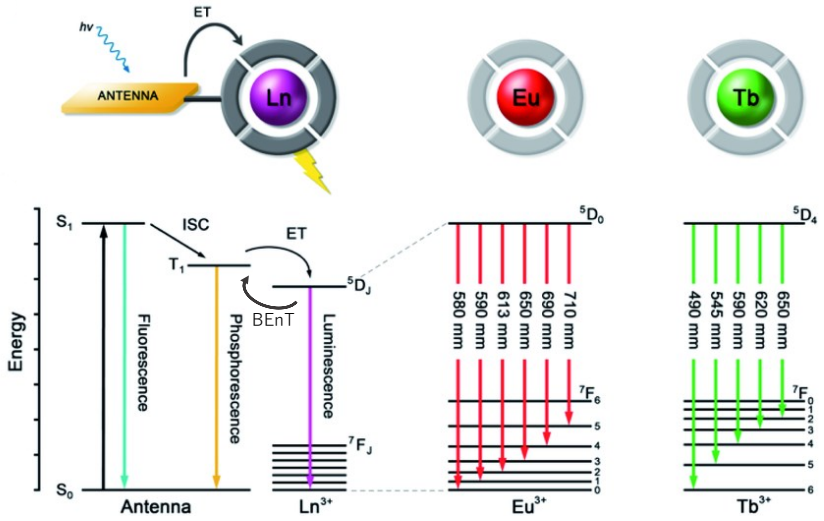

Figure 1.5. Jablonski diagram schematizing the possible energy flow in lanthanide-based antenna complexes, here specified for the red and green luminescence of the Eu^{3+} and Tb^{3+} ions. Acronyms legend: ISC = intersystem crossing, ET = energy transfer, BEnT = back energy transfer. This illustration is taken from ref.[61] with minute modifications for the sake of the discussion.

Besides the frequently encountered triplet-state-mediated path, the energy transfer may alternatively take place implicating ligand singlet state,[62] the simultaneous coexistence of the triplet and singlet intramolecular energy transmission,[63] or the recently proposed charge transfer ILCT and LMCT routes.[64]

The overall energy path concurs to define the efficiency of Ln^{3+} sensitized emission (Φ_{SE}), being governed by three separated contributions: the ISC efficiency (Φ_{ISC}), the

energy transfer efficiency (Φ_{ET}) and the intrinsic lanthanoid-centered photoluminescence quantum yield (Φ_{PL}^{Ln}), following the equation

$$\Phi_{SE} = \Phi_{ISC}\, \Phi_{ET}\, \Phi_{PL}^{Ln} \qquad Eq.1$$

The aforementioned light-harvesting phenomenon may be mitigated when other dissipative pathways dominate over the radiative transition probability.[65]

The main radiationless deactivation process is known as multiphonon relaxation and it is ascribed to high-energy vibrational quanta of quencher oscillators, mostly –OH ($\nu \approx 3600$ cm^{-1}), –NH ($\nu \approx 3400$ cm^{-1}) and –CH ($\nu \approx 2900$ cm^{-1}) stretches, either when present in the first coordination sphere or in vicinity of the rare earth ion.[66] Therefore, precluding optimal coupling between the emissive states of Ln^{3+} and these neighbouring energy-matched groups is an essential precaution to not have a dramatic drop in the sensitization efficiency. In order to reduce vibronic quenching, a clever solution can be to devise a suitable rigid and solvent-sheltering scaffold around the lanthanoid center. In addition, a protective environment should be used since usually the $^3T^*$ suffers to be quenched by O_2.

Ligand fluorescence or phosphorescence, whose observation implies incomplete complexation or inefficient energy transfer,[67] can also be regarded as an inhibiting mechanism for the metal-centered luminescence.

Finally, as introduced earlier, back energy transfer from the lanthanide emitting level to the triplet ligand state becomes probable and relevant when the energy separation $\Delta E_{T\text{-}Ln} \leq 1500$ cm^{-1}.[68] Henceforth, the ET efficiency strongly decreases due to this reverse pathway. This back and forth condition can be demanded if a luminescent system has to be employed for temperature sensing.[1] Indeed, alterations in this external variable can provoke the modification of different luminescence characteristics, among which the emission intensity, spectral position, decay and rise time, band widths, promoting the monitoring of the target body's temperature (the successive Paragraph 1.3.1. will be dedicated to this topic). As the most frequent cases are concerned, if the luminescent probe is invested by high thermal energy, it is admitted a facile depopulation of the lanthanide emitting level to the upper ligand donor state or a vibrational dispersion, causing an increasingly attenuation of the luminescence

intensity. Conversely, cold environments tend to impede this back-energy dissipation mechanism, thus enhancing the luminescence intensity.

Intermediate values of 1850 $cm^{-1} \leq \Delta E_{T\text{-}Ln} \leq 5000\ cm^{-1}$ are recognized as the confines for designing an intensely luminescent system at room temperature,[69] whereas, as the $\Delta E_{T\text{-}Ln}$ exceeds the 5000 cm^{-1} threshold, the excitation migration is repressed due to the high energy difference.

Furthermore, other less-encountered competitive pathways occur via photoinduced intramolecular electron transfer (PeT) from an excited ligand which includes amino groups near to the emitter ion,[70] intraionic charge-transfer state,[65] or via energy displacement events to a proximate dye or metal aqua ion.[71]

In essence, establishing design strategies for luminescent complexes is a paramount aspect in order to suppress the non-radiative and unwanted de-excitations (unless these are triggered by a chemical or physical observable towards its monitoring the sensor has been intended for), maximize the antenna effect and introduce asymmetry to facilitate Laporte-forbidden 4*f*-4*f* transitions.[1, 72, 73]

1.2.1. The eligibility of a photosensitizer: the β-diketonates case

The coordination chemistry of the *f*-block elements is dictated by the preferential formation of labile and predominantly ionic bonds with easily exchangeable anionic ligands and by the tendency to reach high coordination numbers.[52]

Exploiting the stabilizing chelating effect of polydentate systems together with the oxophilic and hard nature of the lanthanoid ions, an efficient and more stable complexation can be promoted by a wide variety of high electronegative donor atoms (binding preference O > N > S). Besides macrocycles,[74] carboxylates and multidentate organic chromophores,[75, 76] *β*-diketonates and their derivatives historically form the most proficient luminescence-harvester group, as singly charged bischelates.[77]

Exhibiting keto-enol tautomerism and a different acidity depending on the substituents, they easily undergo to *α*-deprotonation and the negative change of the resultant conjugated base can be partly delocalized in the lanthanoid ion, after the metal ion chelation.

They easily form neutral ternary tris-diketone-Ln^{3+} compounds in a 1:3 ratio, if the synthetical recipe aims to mononuclear complexes, as well as the tetrakis anionic complex if the ratio is 1:4.

Their aromatic and fluorinated versions powerfully compete with respect to the aliphatic ones in luminescence sensitization, and, together with auxiliary ligands, concur to saturate the Ln^{3+} coordination sphere, so to avoid any solvent interactions, as, for instance, the one with water molecules.[78] The coordination promoted by ancillary Lewis bases contributes instead to enhance the brightness of the complex[79] and extend the excitation wavelength towards the visible range.[80]

Additionally, vibrational relaxation conveyed by the surrounding medium can be repressed by incorporating rigidity, hydrophobicity and steric hindrance in the structure of the peripheral coordinating sphere.

From the viewpoint of ligation, 1,3-dicarbonylates can yield a variety of binding modes, encircling the metal ions in the outer shell.[81] They are both capable of stabilizing a mononuclear complex and driving the formation of finite-sized polynuclear hydroxo- or oxo-clusters.

As evinced from Figure 1.6, β-diketonates can realize four main interactions within multinuclear complexes, respectively classified as η^2-mode I, (μ-O)-η^2-mode II, (μ-O)$_2$-η^2-mode III and (μ-O-η)-mode IV depending on the precise lanthanoid-oxygen relation.

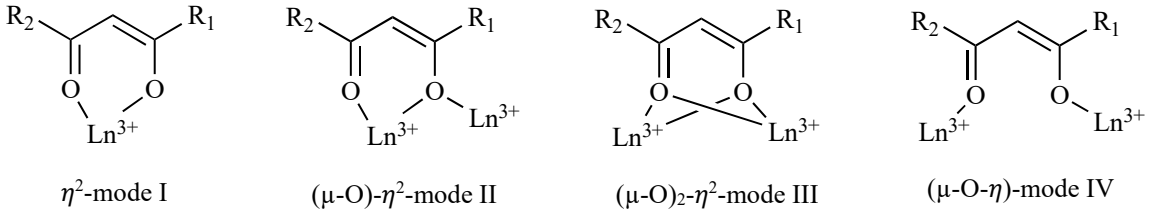

Figure 1.6. Selection of bonding modes played by a generic β-diketonate ligand in polynuclear Ln^{3+}-β-diketone complexes. The scheme was rebuilt from ref.[81]

As above explained, the β-diketonate excited singlet, triplet and ILCT states define the luminescence sensitization process.[82] When these dicarbonylates coordinate with a Ln ion, the corresponding ligand absorption band is not radically affected upon lanthanoid complexation, thus preserving the electronic environment of the antenna.

The β-diketonate triplet state, which is filled via ISC according to the most recurrent photosensitizing route, often resides at a lower energy than the feeding singlet state and, concurrently, aptly above the accepting emissive levels of the lanthanoid ion. Therefore, a deciding factor in the selection of the harvester is decreed by the relative energetic gap $\Delta E_{T\text{-}Ln}$, as exhaustively detailed in the previous paragraph.
An appropriate ^3T energy can be finely tailored with the choice of suitable functionalizations and an accurate scaffold design.[83]

1.3. The multifaceted application landscape of Ln^{3+} antenna compounds

Several reviews state that trivalent and multinuclear Ln^{III} compounds could act as active emissive species for a broad range of versatile applications, due to their attractive luminescent features.[2, 84] Given the functional properties discussed at the end of this thesis work, luminescence-based temperature determinations and energy harvesting devices are here described in more detail.
The scientific community is currently investigating the role of these lanthanide-containing substances in more complex configurations, specifically as additives within a host substrate, rather than in their pristine and isolated molecular form.[2]
The great focus deserved to these innovative hybrid materials is due to the possibility to diminish the emitters' luminescence quenching and photodegradation thanks to the entrapment process. Such confined environment offers to the lanthanide complex a shelter from moisture and atmospheric oxygen, known as triplet quenchers, and attenuation of vibrational dissipation, thus leading in principle to a more intense photoluminescence.

1.3.1. Luminescent molecular thermometers

Physical variable variations, namely pressure, temperature or mechanical stimuli, crucially determine the evolution and effects of a plethora of artificial and natural processes, either on a macroscopic and submicrometric levels. Particularly, accurate ways of temperature detection have glinted significant relevance in numerous research fields, extending from life science to microelectronics.[85, 86] To enumerate some examples, a

precise steady-state and transient visualization of thermal distribution over a surface is essential in aerospace, fluid dynamics, climate research and nanomedicine.[87]

Recent advancements have focused on more demanding techniques for measuring the temperature content in the target environments. Hence, contactless and non-destructive luminescent molecular thermometers have emerged and gained significant attention.[88]

The captivating conception of luminescence thermometry replaced traditional sample-contact thermometers and overcome their operative fragilities. Indeed, disadvantages of conventional probes includes the arduous temperature mapping at the microscale, especially when the specimen under investigation is reduced to such dimensional range, and their one-point revealing modality. To cite, self-adhesive nanosheets containing a Eu^{3+}-based thermosensor surmounted the spatial resolution even of IR thermal cameras, going down to single tissue fiber level.[89]

Therefore, the non-invasive category of optical advanced sensors has emerged over the latest decades, permitting also high-level spatial resolution up to nanometric domain and acquisition time briefer than one millisecond.[90]

In the framework of Luminescent Molecular Thermometers (LMTs), thought both in discrete or wider architectures, the temperature dependence of the luminescence properties of systems including organic dyes, semiconductor quantum dots (QDs) or lanthanide ion is monitored. [91]

Historically, organic fluorophores have been regarded to as the first and most accessible thermoresponsive systems.[88, 92]

Reportedly, one of their advantages is the high sensible thermometric response in the physiological temperature range, thus exploitable in biological and biomedical contexts. However, their frequent tendency to be thermally quenched at elevate temperature and to photodegrade usually precludes protracted real-time mapping of heat gradients.

More recent is the advent of QDs and Ln^{3+}-based materials thanks to their higher photo and thermostability.[87, 93, 94, 95]

Regardless of the emitter's nature, a luminophore's emission feature correlated to temperature changes (*e.g.* lifetime, transition intensity or peak position shift, as displayed in Figure 1.7) is defined as the thermometric parameter Δ.[96]

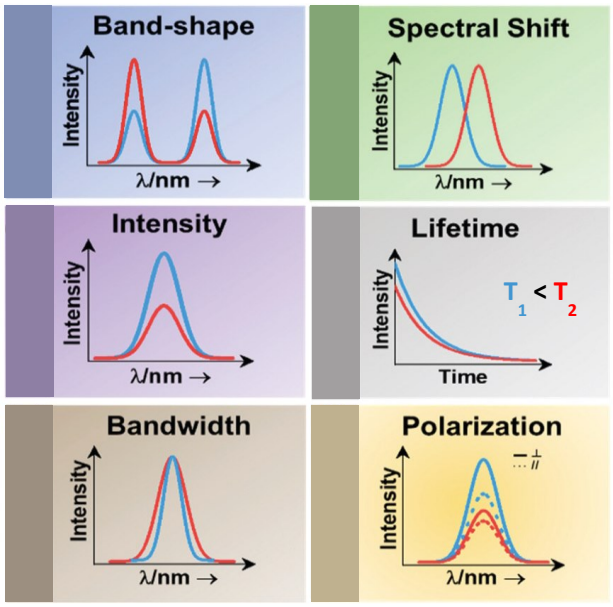

Figure 1.7. Luminescent thermometers classification according to the photoluminescence spectrum feature relatable to temperature changes. Each spectral parameter can be interpreted as Δ. Image adapted from ref.[98]

Among the main protocols to evaluate the temperature modifications in LMTs, the integrated intensity approach of a sole transition is normally preferred in single-emitting systems. Nonetheless, in certain situations, this measurement could be affected by illumination fluctuations and photobleaching issues. These limitations can be defeated by a ratiometric approach which, following the ratio of a pair of integrated intensities as the thermometric parameter, assures self-calibration using a second emissive transition as an internal reference.[97]

A universal comparison of the thermometric performance of every kind of thermal probe can be conducted through the figure of merit S_r, representative of the relative thermal sensitivity.[96] The usefulness of this metric lies in its entirely independence from the identity of the thermal probe. Indeed, the relative thermal sensitivity allows for comparisons not only between different LMTs but also among LMTs and thermometers that are based on distinctive thermal probes and physical principles. To derive S_r, the thermometer's performance is assessed by measuring the infinitesimal change of the thermometric parameter per degree of temperature, normalized by Δ itself, according to the following Eq.2:

$$S_r = \frac{1}{\Delta}\left|\frac{\delta\Delta}{\delta T}\right| \qquad [\% \cdot K^{-1} \text{ or } \% \cdot {}^{\circ}C^{-1}] \qquad Eq.2$$

In LMTs, it is usually conveyed that the threshold of $S_r > 1\ \% \cdot K^{-1}$ indicates a good thermometric response. Instead, the maximum S_r value reached by the thermosensor is expressed as S_m.[88] It is often required the complementary usage of more than one luminescent sensor, since it is rare that a single system possesses a broad applicative temperature range, i.e. a wide-ranging thermal sensitivity higher than unity.
Accordingly, the panorama of lanthanide-englobing LMTs is constantly under development, leading to more efficient molecular systems also for biological purposes.[98]

1.3.1.1. A brief spotlight on Ln^{3+}-based thermal sensors

Capable to emits lines from the UV to near-IR spectrum, lanthanide-including species can perform remote and non-intrusive temperature readouts covering a broad spectrum of values, from the cryogenic up to the physiological temperature scales. The first high-resolved thermal imaging using a lanthanide complex, namely $Eu(tta)_3$ (where tta denotes thenoyltrifluoroacetylacetonate) in deuterated PMMA, has been presented in 1983.[99] Since then, a variety of them has been developed in the past years and articulated in many distinctive fashions, such as in the form of up- and down-converting nanoparticles, metal organic frameworks (MOFs), chelate complexes, sometimes in combination with *d*-block metals, and even incorporated into a polymer binder or into a thermographic phosphor structure.[87, 100]
The luminescent thermometric response of a Ln^{3+} ion is strongly dictated by its antenna and ancillary ligands. Specifically, a small energy gap between the Ln emitting levels and the antenna triplet increases the likelihood of BEnT. Under these conditions, even slight temperature changes can significantly impact the back-transfer pathway, thereby altering the luminescence intensity.
This process is easily manipulated by molecular design: in fact, the energy gap between this couple of levels can be conveniently tuned by varying the sensitizer moiety or the rare earth nature. Moreover, other temperature dependent non-radiative deactivations can interplay with or dominate over the BEnT. Anyway, it is generally accepted as one of the most influent photophysical contribution for the thermometric efficiency (a case validating this observation is described for Tb^{3+} mononuclear complexes in literature).[101]

It has been observed that the levels' separation is strongly correlated with the amplitude and localization of the operative window along the temperature scale: the higher $\Delta E_{T\text{-}Ln}$ results, the greater the shift in thermal sensitivity towards higher temperature.

The studies including Ln^{3+}-based LMTs mostly blossomed in the early 2000s, concerning mononuclear complexes and inorganic nanoparticles, with the former almost exclusively facing *β*-diketonate antennae.[102]

Besides the choice of the photosensitizer ligand, a luminescent thermometer can modulate its operative range varying the central metal ion. To illustrate, by looking at the pair [HQ][Ln(btfa)$_4$], where Ln^{3+} designates Eu^{3+} or Tb^{3+}, Q the pyrrolidine and btfa the benzoyltrifluoroacetonate, the working thermometric frame moved from 100-220 K to above 300 K, in passing from europium to terbium.[103]

Successively, lanthanide-based metal organic frameworks and capsules have been proposed as more complex structures, often in the dual-centre version (so far, Eu^{3+}/Tb^{3+} or dye/Ln^{3+} mixes).[104, 105] Up to now, lanthanoid MOFs have reported one of the highest relative thermal sensitivities, either in the cryogenic and in the physiological temperature regimes (S_m = 31 %·K^{-1} at 4 K[106] and S_m = 16 %·K^{-1} at 300 K[107], respectively).

To seek thermosensing ability improvements, Miyata and colleagues remarkably made a dual thermostable sensor, combining the ratiometric sensing of Eu^{3+} and Tb^{3+} emission intensities, phosphine oxide likers as vibrational relaxation suppressors, and fluorinated harvesters (1,1,1,5,5,5-hexafluoropentane-1,4-dione, hfa) into a coordination polymer framework.[108] The resulting one-dimensional chain $[Tb_{0.99}Eu_{0.01}(hfa)_3(dpbp)]_n$ (Figure 1.8), where dpbp represents 4,4'-bis(diphenylphosphoryl)biphenyl, was found to be very stable under reversibly repeated thermo-cycles in the 300-400 K interval.

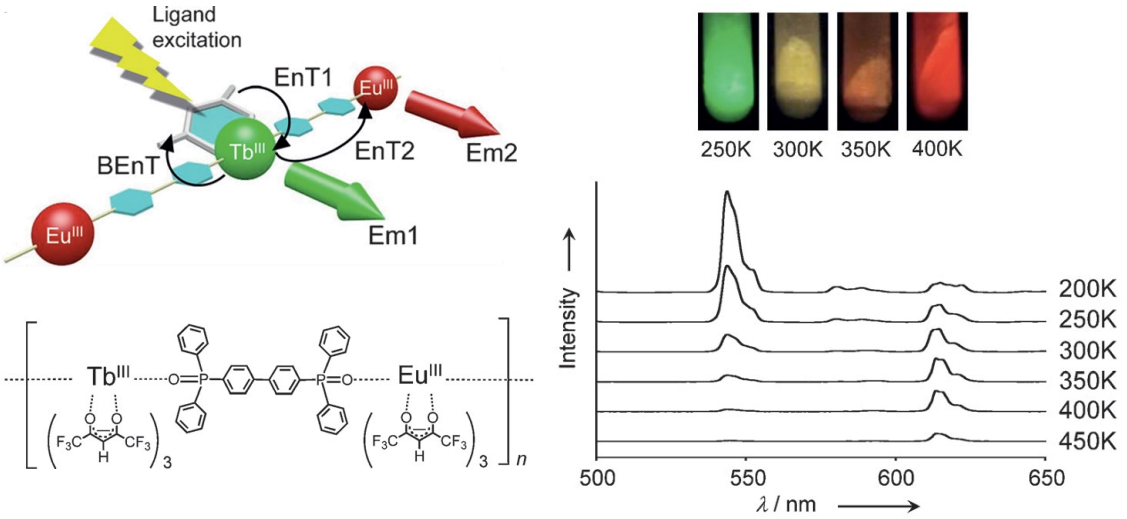

Figure 1.8. Left side: energy transfers and chemical structure of the polymer $[Tb_{0.99}Eu_{0.01}(hfa)_3(dpbp)]_n$ (EnT: energy transfer, BEnT: energy back transfer, Em: emission). Right side: photographs under 365 nm indicating the colour tuning of the material as the temperature changes and the corresponding temperature-dependent luminescence spectra in the solid state in the 200-450 K range. Images assembled from ref.[108]

Other promising and more recent systems for molecular luminescent thermometry included multicentre clusters,[12] exhibiting either small (Eu_8)[34] and large (as in the nanopillar Eu_{48} and Tb_{48} architectures)[109] nuclearities. Illustrative examples also belong to the lanthanide-titanium-oxo clusters category, where a linear correlation between temperature and emission intensity was noted for core compositions like Eu_2Ti_4, Eu_5Ti_4 and Eu_8Ti_{10},[43] Eu_9Ti_2 and Tb_9Ti_2,[110] $EuTi_9$ and $TbTi_9$,[111] with more pronounced thermometric sensitivity in the terbium counterpart for the last two cases.

Polynuclear structures have also been implemented as nodes to build up supramolecular MOF scaffolds, combining the components' properties and thus reaching unprecedent S_m values up to 32 % · K^{-1}.[112]

Parallel to the design of lanthanide-based thermometers at molecular level, their incorporation in solid matrices (hydrogels, NPs, polymeric films) has led to promising nanocomposite platforms with the enhanced desired characteristics at micron and sub-micron scales.[87, 91]

One of the pioneering works on these hybrid LMTs dates back to the 1980s, when temperature mapping was successfully achieved on integrated circuits using a thin polymethylmethacrylate film embedded with the europium(III) thenoyltrifluoroacetonate

complex.[113] The same luminophore was later investigated into various polymeric matrices,[95] and combined with other kind of ancillary ligands.[114]

Furthermore, in these hybrid materials, the antenna features, the Ln/antenna ratio in the complex, as well as the polymer nature and the concentration of the complex within the polymer matrix, influence the temperature-dependent luminescence decay. Among Eu^{3+} tris(β-diketonate) complexes, the ones bearing 1,3-bis(2-thienyl)-1,3-propanedione derivatives and dispersed into polystyrene nanosheets were found to have the highest thermal sensitivity values ($4\ \%\cdot K^{-1} < S_r < 5\ \%\cdot K^{-1}$) around room temperature.[102]

1.3.2. Luminescent solar concentrators

Despite solar energy is the most copious reserve on Earth's surface, yet there is a huge imbalance between our usage of it and its immense potential. Harvesting sunlight is regarded as one of the most effective and greenest strategies for addressing environmental concerns related to climate change. This approach leverages the ability of photovoltaic (PV) panels to convert solar electromagnetic radiation into exploitable electrical energy, making them one of the most valuable technologies for tackling this challenge.

Traditional semiconductor-based cells, like the silicon ones, typically reach conversion efficiencies of just over 20 %.[115] They operate in a drastically reduced performance under mutable weather conditions and are only effective at capturing light when perpendicular to the solar source, reducing their versatility.

Thus, in the prospect to assist this sustainable energy production, an increasing emphasis has been oriented to the renewed field of the more versatile building integrated photovoltaics (BIPVs).[116] Among these innovative ways to manipulate sunlight and complementarily cooperate with traditional photovoltaic technologies, luminescent solar concentrators (LSCs) have been offered as a solution to potentially serve as energy harvesting devices.[117]

The state-of-the-art of these photonic platforms is typically described as a bidimentional film or planar slate of glassy or polymeric material, within which the optical emitting centers are encapsulated (see Figure 1.9). These luminescent species possess the ability to capture the direct or diffuse incident solar radiation, re-emit it at longer wavelengths and concentrate this emission towards the substrate perimeter. This downshifted light is

waveguided through total internal reflection (TIR) within the host medium until it is directed to the edges of the system. At this point, the photons are collected by side attached PV cells and transformed into electrical current.

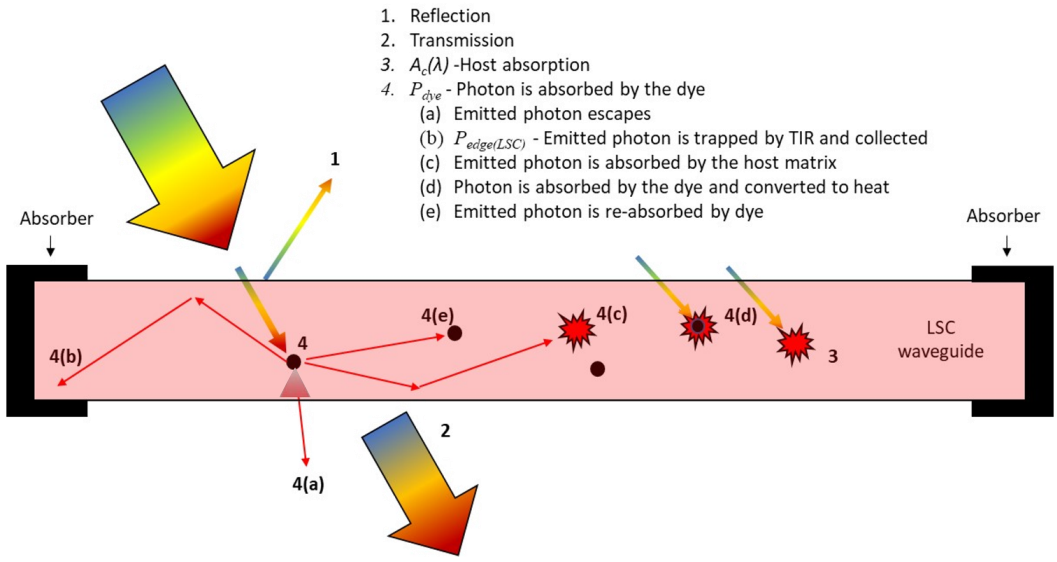

Figure 1.9. Schematic illustration of the main working pathway (TIR) and fate of photons incident onto a luminescent solar concentrator edge-couple with absorber PV cells. Reproduction from ref.[118]

Overall, a dual purpose is achieved, specifically the accumulation of electromagnetic energy from a large area to a reduced one and the conversion of it to a wavelength window more compatible with the PV acceptor's responsivity.[119]

The LSC concept dated from the late 70s,[120] but gained major consideration over the last decades as a technology implementable in urban architecture in order to turn building façades elements, principally windows, into active electrical power generators.[121] For this purpose, these auxiliary solar technologies need to be harmoniously merged with the external decorations of edifices and supply the ideal demand of realizing net-zero-energy infrastructures (see Figure 1.10).

To accomplish these two primary tasks, it is essential to carefully select an appropriate combination of the incorporated emitters and the host waveguide. The former constituents govern the photophysical properties, while the latter determines light transport. Together, they also impart unique aesthetic qualities to the resulting material, including transparency, flexibility, and coloration.

Since the fundamental roles of harvesting incident radiation and optimizing the optical conversion efficiency of the entire device are assigned to the emitting species, they must

meet crucial requirements.[119] Indeed, an ideal luminophore should ideally possess several key qualities: a wide spectral absorption range, a high extinction coefficient across the whole spectrum, a significant Stokes shift to minimize auto-reabsorption losses, easy dissolution in the host matrix, and emission frequencies that align with the bandgap of the PV system.

Within this framework, the literature reports three main categories of emitters, namely quantum dots, even with a core-shell structure,[122] natural pigments and organic dyes,[123] and metal complexes typically belonging to the *d* and *f* periodic blocks.[119, 124] Additionally, they are distinguished based on their selectivity or not towards ultraviolet or near infrared photons' stimulation.

To design highly transparent and colourless LSCs compatible with domestic and working environments, the most promising luminophores are embodied by lanthanide antenna complexes, mainly containing Eu^{3+} and Tb^{3+} ions.[119] This class of compounds is preferred due to high absorptivity, complete separation between the ligand absorption band and the emission one, and the exploitation of the ultraviolet portion of the solar spectrum. Conventional glass can absorb UV rays, which cause fading and yellowing of furniture, but it does not perform an energy conversion task. Therefore, a cover or replacement realized with an LSC layer would retrieve space for energy-producing panels.

Briefly comparing with the other above-mentioned species, organic chromophores possess significant drawbacks, including their tendency to absorb visible photons, making them unsuitable for the neutral appearance required for everyday BIPV installations. In addition, their small Stokes shifts give raise to undesired self-absorption events.[125] Similar considerations can be made for natural pigments: even if they are more ecological candidates, they are characterized by almost the same displeasing properties.

Concerning the inorganic realm, colloidal semiconductor nanocrystals, especially chalcogens and perovskites of Zn, Cd and Pb, manifest tunable size-dependent emissions but present a higher toxicity and easily undergo oxidation when processed in contact with the atmosphere and photoblinking.[119]

Correspondingly, the lightguide should fit distinctive peculiarities, ranging from significant transmittance in the visible and NIR spectral intervals, high refractive indexes, thermodynamic stability while subjected to the fabrication process and to the open-air exposition, as well as solubility compatibility with organic solvents and a wide assortment of luminophores.[126]

The initial choice of glass was soon abandoned, fundamentally due to its notable absorption in the 800-1000 nm window which interferes with a Si-LSCs systems. Nonetheless, its current utilization deals with the fabrication of luminescent thin-films concentrators,[127] having the role of a transparent substratum (see Figure 1.10d).

Commodity polymeric matrices, such as polyacrylates, polycarbonates and polysiloxanes, succeeded as preferred hosting matrices, thanks to their significant optical transparency, disposability and ease of processability.[128]

Focusing on the polyacrylate class, polymethylmethacrylate is a widespread and economically convenient option (see Figure 1.10a for an LSC prototype made of doped PMMA). To enumerate some of its qualities, it manifests transparency to visible photons, high refractive index so to minimize sunlight reflections and a fairly good photostability. It was also demonstrated an improved NIR transparency defined by an absorption coefficient of $2 \cdot 10^{-4}$ cm^{-1}, if its C–H bonds are subjected to fluorination.[121] Although PMMA exhibits brittleness, it offers valuable mechanical and thermal properties, including better resistance to temperature fluctuations compared to glass.[128] Consequently, it and its substituted variants were widely employed in previous LSC production, either in slab and film shapes.[129, 130]

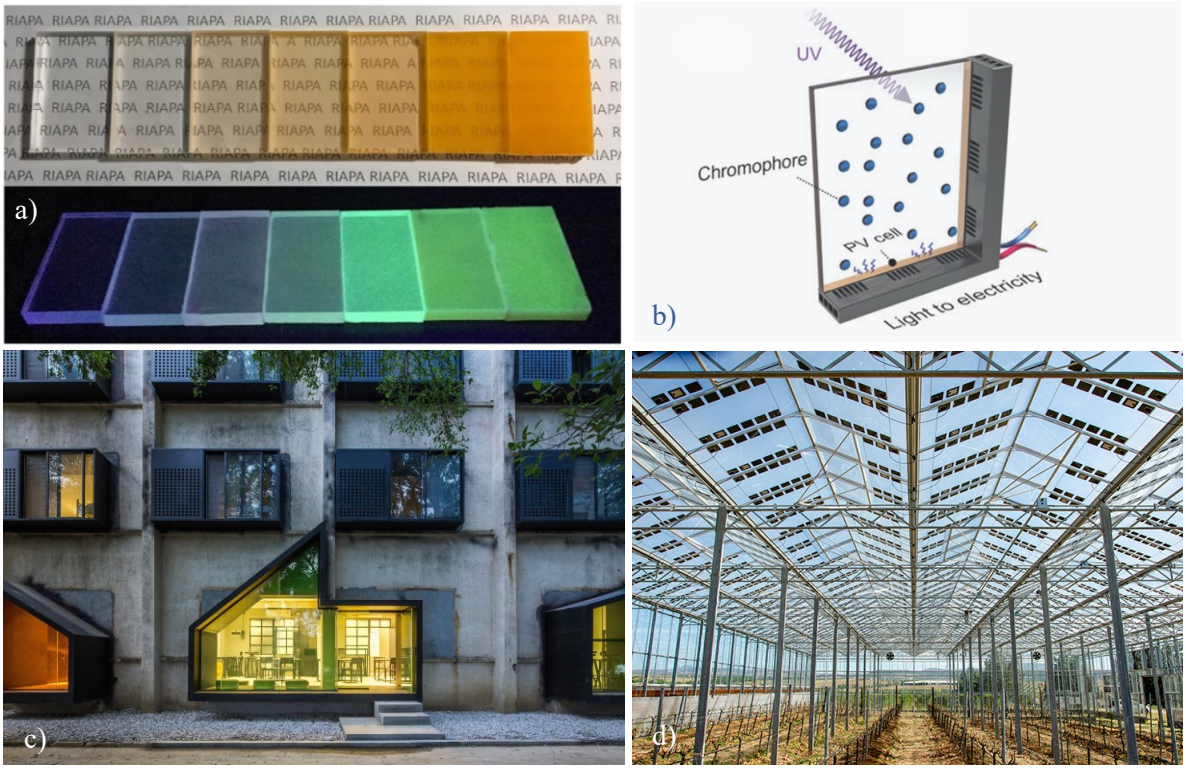

Figure 1.10. a) $CH_3NH_3PbBr_3$-doped PMMA waveguides with different degrees of transparency, seen under ambient and UV lighting.[131] b) Depiction of how a transparent luminophore-doped glass with PV cells coupled all around could replace an electrically-passive window, after a proper scaling up of the material. c) Coloured glass panels that adorn the external of the Youth Hotel, Shenzhen, could be turned into domestic electricity generators if modified to function as LSCs. d) More versatile colourless LSCs integrated into covering for agriculture purposes.

As just stated, a multitude of geometries and types of material components had been proposed, nevertheless it is also indispensable to provide a qualitative picture of the functional skills.[132]

The parameters commonly used to evaluate a LSCs operation are reviewed in literature and altogether contribute to define their power conversion efficiency (PCE).[133] This performative metric is quantified by the ratio between the maximum output power extracted at the LSC perimeter and the incident optical power. According to recently reported developments, the record value of PCE, 9.6 %, was achieved with a coloured upconverting dual panel LSCs, enclosing perylene and a functionalized tetrabenzoporphine palladium complex, coupled to perovskite solar cells.[123b, 134]

For the purposes of this thesis, a more detailed discussion of this and other important performance metrics, commonly used in PV evaluation, will be matter of the Experimental and Appendix sections.

Distinct optical and energy conversion losses are suffered from the LSC when it interacts with sunlight and compete with the wanted collimation route towards the PV strip (Figure 1.9). An ensemble of factors quantifies the portion of sunlight missed or gained at the edges: reflections by the exposed surface of the concentrator, dictated by its refractive index, the ratio of photons absorbed by the optically active stratum to the number of photons impacting on it, the thermally-dispersed and the escaping radiation, self-absorption, the photoluminescence quantum yield of the fluorophore and the transport efficiency.

All these optical efficiency contributions are arduous to ponder and to individually disentangle. Moreover, some of them can be overwhelmed through specific constituents' choice and procedure's improvement.[135]

For example, the detrimental luminophores' reabsorption, which obstacle the scale-up of the device, can be totally neglected in the favorable Ln^{3+} case which assures a null overlap integral between the absorption and emission bands.

The TIR guidance of photons can be enhanced by minimizing defects' absorption and scattering phenomena which would hinder a light travel straightforward to the luminescent layer's edges.[121] Due to the eventual meeting of trapped dust, air bobbles or precipitated luminophores' aggregates, a reduced portion of photons will be captured by the coupled PV modules and the LSC performance will be underestimated. Thus, optimization of the material's manufacture in order to create a homogeneous block is considered a fundamental precaution to fully exploit the solar concentrator's operation.

1.3.3. Other applications

Beyond the two areas covered in this thesis, the advanced applicative panorama of lanthanide-containing materials embraces many other diverse fields. Luminescence vapochromic devices,[136] anti-counterfeiting inks for protecting sealed documents,[137] fluorescent logic gates for molecular-based computing,[138] upconverters and laser materials are just a few numbers of them.[2]

Connected to the luminescence thermometric field, the instantaneous determination of the temperature distribution of a surface can be imaged also through temperature sensitive fluorescent paints (TSPs), where lanthanide complexes luminescence can be formulated to simultaneously sense variation of pressure or some analytes presence.[91, 139, 140] As dual or single sensors, they are typically conceived as small-molecule-based nanocomposites, whose impingement on a temperature-detectable system can be realized through spraying or brushing. Another remarkable characteristic is the possibility to be used for non-blurred imaging of objects in motion. Moreover, the versatility of the above-cited LSC units makes them declinable into various fields of application. Among them, they have been tested and proposed as alternative catalysts for photochemical reactions promoted by sun radiation, functional greenhouses roofing or garden fences, safety-enhancing lighting and charging resources.[141]

In this multitasking perspective, the generation of lanthanide-based optical materials, selectively or simultaneously suited for a multitude of technological and daily-life applications, represent a pioneering and constantly evolving research field.

CHAPTER II

Aims and outline of the thesis project

As remarked in the Introduction, Eu(III)-β-diketone compounds have been always recognized for their fascinating photophysical behaviour. The antenna effect, governing their unique emission properties, raises them as eligible candidates for luminescent multifunctional materials exploitable in light-driven applications, such as in the contactless luminescent molecular thermometers and in the emerging luminescent solar concentrators scenarios. Therefore, the main task of the present thesis is to provide a contribution in these versatile fields, particularly exploiting the emission properties of sensitized Eu^{3+} structures that are classified as selective UV-absorber luminophores.

Explicitly, the three prepared and then processed molecular systems consist of a pentanuclear oxocluster having formula $Eu_5(DBM)_{10}(OH)_5$, and two mononuclear complexes containing the same lanthanide ion and organic chromophore, individually denoted as $Eu(DBM)_3(H_2O)_2$ and $Eu(DBM)_3(DME)$ (where DBM stands for dibenzoylmethane and DME for dimethoxyethane bischelates). Thus, distinct nuclearities have been explored, also in order to make a comparison of their luminescence with the increasing number of metal ions in the central core. Published photophysical investigations on trinuclear Eu^{3+} β-diketonates supported increments in luminescence sensitization respect to their corresponding mononuclear entities.[142]

Additionally, this specific penta-oxocluster, which was studied in literature since its discovery dated in 1999, was never applied for the aforementioned roles. Rather analogous considerations can be done for the two monometallic structures, especially for the DME-coordinated species whose polymeric encapsulation was never thought as an alternative way for testing these particular performances.

In the prospect to prepare luminescent nanomaterials based on these molecules, the research project is divided into three main progressive phases, all detailed in the subsequent Chapter III.

The first part of the experimental work mainly deals with the synthesis of the above stated three europium-based luminophores and their characterization. The nature of these systems has been unraveled by a combination of UV-Vis absorption and infrared

spectroscopies, mass spectrometry, single crystal structural studies and X-ray photoelectron spectroscopy.

In the second part of the same Chapter, an improved fabrication procedure of luminescent hybrid materials in a thin polymeric film configuration is described. Finally, spectroscopic and functional responses of such doped layers were acquired. These latter aspects encompassed testing the doped red-emitting films for their luminescence-temperature correlation properties and conducting preliminary proofs for their potential implementation as luminescent solar concentrators devices.

The search for more accurate and sensitive molecular temperature sensors is a challenging and crucial task in countless technological developments and in all the situations in which a non-undermining and a precise tracking down to the nanometric scale is rigorously required. Among the variety of T-sensitive molecular systems, the scientific community has been particularly focused on luminescent lanthanide-including species, as one of the most efficient structures to monitor local heat transfers. Indeed, a conspicuous catalog of their thermal-responsive complexes in pure solid state is documented in literature, whereas they are still underexplored in their oxocluster versions, expressly when embedded (the majority of the reported thermal-responsive studies are essentially concentrated on their unprocessed solid-state form).[100] Moreover, the realization of their compact and uniform luminescent films can overcome the disadvantages of free powders to be hard to handle, easily dispersible, contaminative for the environment and to be difficult to recover.

The additional interest towards greener energy transition and alternative photovoltaic technologies has led to promote and reinvent new ways to harness solar light. Rare-earth mononuclear complexes started to be regarded as UV-selective luminophores for untinted LSC arrays, but cluster-polymer blends have principally involved *d*-block metals in the past.[143]

Generally, since pure lanthanoid-based structures are increasingly in demand for the aforestated luminescent tasks, it is indispensable to engineer new efficacious compounds and test the already-discovered ones.

Subsequently, this work intends to participate to these fields by designing the respective bulk materials of the synthesized molecules in order to transform them in a more exploitable form and to support potential future insights for these applicative destinies.

Conclusions and perspectives are defined in Chapter IV and, ultimately, the detailed experimental part is reported in Chapter V. A final Appendix section completes the present dissertation including supplementary data.

CHAPTER III

Experimental results and discussion

In the first part of the present Chapter, the synthesis and characterization of the obtained Eu^{3+}-based architectures are described. A brief overview of the literature disclosed procedures useful to prepare oxocluster-type structures enclosing *f*-block elements along with the criteria preferred to select the most qualified luminophores are provided.

Several techniques have been exploited to get details about the effective formation of such systems and to investigate their distinctive photophysics. Likewise, electrospray ionization mass spectrometry (ESI-MS) and X-ray photoelectron spectroscopy (XPS) have been employed to confirm the identity and the stoichiometric ratios between the atoms involved in the coordination cages. Moreover, through single-crystal X-ray diffraction (SC-XRD) analysis it was possible to elucidate the structure of different oxoclusters and compare the results with literature data.

Lastly, the vibrational pattern of the main ligand's functional groups and their features partly affected by the lanthanide centres proximity were probed *via* attenuated total reflectance (ATR) FT-IR spectroscopy. UV-vis absorption spectra for all the investigated compounds were also collected.

The latter part of this Chapter is dedicated to the incorporation method used for integrating the realized compounds into polymethylmethacrylate substrates with the purpose to prepare micrometric-thick films, hence creating luminescent functional materials. The polymeric film configuration was appositely planned to enlarge the applicability field of these luminescent species, basically by increasing their processability. This material processing will lead the final system to be contemplated for diverse functions in addition to the ones introduced into this project, expanding from temperature sensitive paints and anti-counterfeiting agents to miniaturized ultraviolet sensors.

After an exhaustive description of the methodology complied for attaining such thin layers, the characterizations devoted to their spectroscopical (absorption and emission responses) and functional behaviour as luminescent devices (LMTs and LSCs) are then discussed. These last experiments comprised temperature-dependent sensing tests in the 83-300 K range and electrical measurements in order to verify if they can be classified

as promising luminescent molecular thermometers and luminescent solar concentrators, respectively.

3.1. Synthesis and characterization of Ln^{3+} luminophores

As mentioned earlier, this research deals with the preparation and utilisation of photoluminescent europium *β*-diketonate systems, specifically of $Eu(DBM)_3(H_2O)_2$, $Eu(DBM)_3(DME)$ and $Eu_5(\mu_4\text{-}OH)(\mu_3\text{-}OH)_4(\mu\text{-}DBM)_4(DBM)_6$ - or more compactly $Eu_5(DBM)_{10}(OH)_5$ -, that will be labelled as Eu^w, Eu^g and $[Eu_5]$ throughout the text, respectively.[I]

Some other synthesized compounds, but not considered here for further applicative aims, will be introduced and correspondingly named, as they are encountered.

Initially, a rapid *excursus* on the distinctive categories of multinuclear antenna compounds of the Ln(III) ions taken into consideration will be outlined; thenceforth, a deeper focus will be oriented to the selected molecules' preparation and characterizations stages.

3.1.1. From nanoclusters to mononuclear complexes

Since lanthanoid-based oxoclusters have emerged as beneficial for their peculiar photophysical properties,[41, 43] the synthesis of various families of them was originally explored. In fact, their photophysics can be properly modulated using specific synthetical strategies in order to control the reduction of nonradiative dissipations, according to the target applications.

Different nuclearities, spacing from dimeric until oligomeric metallic cores, were considered, either containing homonuclear Tb^{3+} or Eu^{3+} ions and a heterogenic combination between them and transition metals (more precisely, Ti(IV) and Zr(IV)). Unless not reported in detail, this study comprehended a preliminary part devoted to the replication of several literature syntheses in order to obtain and then process one or more luminescent Ln^{3+}-based hydroxo- and oxo-clusters.

[I] The letter *w* identifies the water molecules' coordination; *g* symbolizes *glyme* which is the common name of dimethoxyethane; in the $[X_n]$ notation, *X* distinguishes the metal ion and *n* the nuclearity.

These classes of compounds were chosen for light-driven applications, adopting for the oxoclusters synthetic routes that do not always obey to a perfectly reproducible protocol. Failures in replicating the literature methods were sometimes faced, bringing up questions about their exact reproducibility under our laboratory conditions.

At the beginning, several procedures were dedicated to the realization of homometallic oxoclusters, modifying the antenna moiety picked from the variously-substituted bischelating *β*-diketonate and carboxylate families.

Among the rare earth series, molecular architectures based on Eu^{3+} or Tb^{3+} ions were preferred since they generally display the highest values of photoluminescence quantum yields.

Along with the homometallic-type, a library of mixed polynuclear species was surveyed, among which the currently emerging lanthanide-titanium-oxo clusters were individuated. The co-presence of Ti(IV) in the inner core helps to reduce the amount of competitive hydroxyl bridges, integrating in place of them Ln–O–Ti motifs that decrease the activation energy for photoluminescence sensitization (see Chapter I, Paragraph 1.1.1. for explanations).[44]

In the following lines, a few examples of these assemblies will be discussed along with the reasons considered to discriminate which of them had the requisites to experience the material processing.

A $[Tb_9Ti_2]$ LnTOC, formulated as $[Tb_9Ti_2(\mu_4\text{-}O)(\mu_3\text{-}OH)_{14}(acac)_{17}(CH_3O)_2(CH_3OH)_3]$ where acac indicates the acetylacetonate ligand, was elected as promising candidate for luminescent hybrid materials, due to its elevated quantum yield of *ca.* 35 %, life time of 663 μs and attracting luminescent temperature sensing properties in the pure powder form.[110] Its formation involved mixing a methanolic solution of hydrated $TbCl_3$ salt and acetylacetone with $Ti(O^iPr)_4$ and a deprotonating amine, then waiting for the final product to crystallize in a cool environment (2-4 °C). Several months were necessary to obtain green-emitting block-shaped crystals (see left part of Figure 3.1) which further grew with a very slow kinetic, conversely to the one week reported by Liu *et al.* Due to this prolonged time, it was decided to not consider this species for the continuation of the project.

Moreover, a solvothermal process, originally tailored for an ensemble of chiroptical europium-titanium oxoclusters, was exploited for novel achiral structures:[144] $Eu_2Ti_4(\mu_2\text{-}O)_2(\mu_3\text{-}O)_4(bpy)_2(ba)_{10}$ and $Eu_2Ti_4(\mu_2\text{-}O)_2(\mu_3\text{-}O)_4(bpy)_2(fba)_{10}$, where bpy signifies 2,2'-bipyridine and ba benzoate, while fba acts for 2-fluorobenzoate, are distinctly

denoted as $[Eu_2Ti_4]$ and $[Eu_2Ti_4]^f$ to differentiate the fluorinated species. A one-pot route was employed, consisting of reacting hydrated europium(III) acetate, a carboxylic acid, bipyridine, and $Ti(O^iPr)_4$ in acetonitrile, followed by heating the resulting suspension at 80 °C for two days.

Despite the ligands' substitution in place of the original ones, these new structures were reproducibly synthesized and separated as strongly red luminescent single cubic crystals (pictured on the right of Figure 3.1). Nonetheless, their solubility turned out to be extremely low whatever the solvent used. Hence, any effort to disperse them into a polymeric matrix was abandoned and only their SC-XRD structures will be examined in the next paragraph.

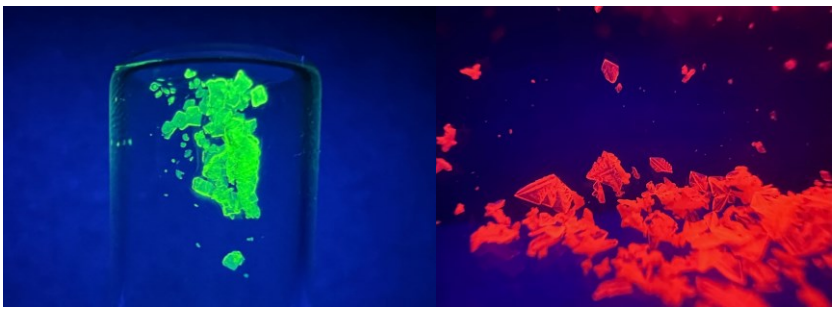

Figure 3.1. Photographs of crystalline samples obtained for $[Tb_9Ti_2]$ oxoclusters on the left and $[Eu_4Ti_2]$ on the right, seen under an ultraviolet irradiation centered at 365 nm (Spectroline® E-Series UV Hand Lamps).

Among the successfully obtained products, a pentanuclear europium oxocluster stabilized by dibenzoylmethanide units was selected thanks to its optimal solubility in chlorinated solvents which are also affine to the host matrix, ease of crystallization, and intense red luminescence qualitatively perceptible under UV irradiation. Its structure was originally reported in the paper by Xiong and coworkers, where an exceptional μ_4-OH bridging mode, unusual for Ln^{3+} systems, was detected.[32] However, this first-proposed procedure has the drawback to include no purification step, thus leading to the coprecipitation of a side product from the starting materials (method I in Figure 3.2). Indeed, even if this five-membered oxocluster was resolved via SC-XRD and corresponded with the literature deposited structure, a minor amount of a white powder product of *N*-methylmorpholinium chloride partially surrounded the crystalline one.

The inclusion of washing steps with methanol and hexane of the centrifugated precipitate and the base replacement, according to the approach proposed by Petit *et*

al.,[34] brought to a product with a hard tendency to crystallize (refer to reaction II in Figure 3.2).

Every successive attempt to substitute a single variable at a time, like the nature of the counterion of the starting Eu(III) salt, the type of the deprotonating agent, or a distinctive crystallization method, did not produce the desired results.

During the past decades, synthetic adjustments to circumvent the downside of impure precipitates were executed. It was suggested to supplement a filtration step in order to separate the chloride salt from the wanted product. In this prospect, two similar pathways were replicated, the only difference between them consists in the choice of the base and of the solvent (routes III and IV in Figure 3.2, correspondingly). One of them resulted in a combination unifying the methods described by Roesky and other researchers for an analogue pentanuclear yttrium hydroxo-cluster and for a series of tetranuclear lanthanide complexes.[18, 31] Despite the complete syntheses' discussion is specified in Chapter V, they briefly comprised a room temperature reaction, a dryness step and the dissolution of the resulting powder in toluene or dichloromethane to remove the side product by filtration.

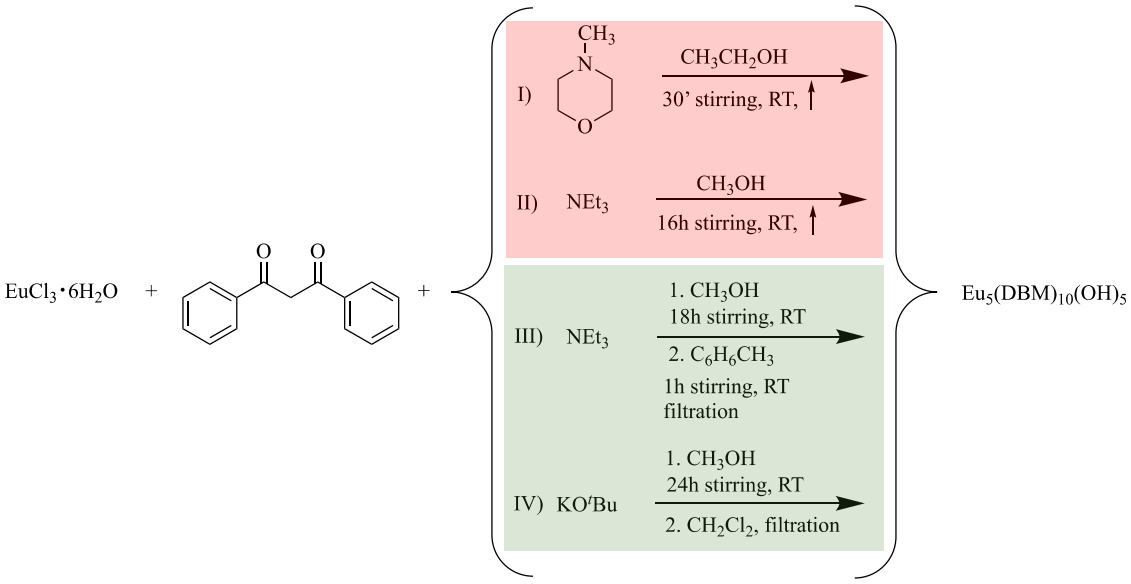

Figure 3.2. Schematic illustration of the passages proposed in the four selected literature procedures for the formation of [Eu_5]. The ones involving issues or a non-crystalline product are highlighted in pink, while the successful ones are in green.

By repeating these improved procedures, a molar ratio of 1:2 was employed for the Eu:HDBM couple. An excess of base guaranteed the quantitative deprotonation of the ligand in order to convert it into an effective chelate for the metal ions.

The organic functionality of dibenzoylmethane was essentially preferred for sensitizing the Eu^{3+} emission by virtue of the high molar absorption coefficient typically ascribed to the π-π* transitions of *β*-diketones.[82] Consequently, HDBM was declined either into other two simpler monometallic complexes to probe whether the increased Eu^{3+} atom content in an oxocluster assembly could truly affect the luminescent properties. Consolidated synthetical procedures were instead adopted for these systems' preparation and described in detail in Chapter V.

3.1.2. Structural determinations

Single crystal X-ray diffraction has been adopted to clarify the structure of all the obtained crystalline samples. Although this paragraph is devoted to [Eu_5] XRD results description, a short report for the other non-processable oxoclusters are described at the end. It is worth highlighting that these latter structures have been obtained for the first time in the framework of this thesis, to the best of our knowledge.

Pale-yellow single crystals of [Eu_5], grown after slow toluene evaporation according to reaction III, exhibited the same atomic organisation previously established for analogue systems.[32, 145] Indeed, the [Eu_5] cluster was resolved and refined in the spatial group $P2_1/c$ where the europium atoms assumed the expected square-based pyramidal motif. An isostructural arrangement has been elucidated in corresponding [Ln_5] compounds containing terbium,[34, 146] samarium,[145] erbium and holmium,[20] thus validating the preference of the more contracted lanthanide elements to self-organize into a five-membered square pyramidal core. Small differences were appreciated in bond lengths, due to the lanthanoid contraction passing from europium to other lanthanides. Albeit maintaining this core geometry, pentanuclear clusters of other rare earths elements manifest a divergent tendency to pack into a tetragonal space group *P*4*/n*, as testified for Yb and Dy.[22, 31]

The asymmetric molecular unit of [Eu_5], reported in Figure 3.3 together with a view circumscribing the inner Eu–O space, revealed an uncharged cluster constituted by five

europium atoms, five hydroxyl groups and ten peripheral dibenzoylmethanide ligands with two different coordination modes, terminal and bridging.

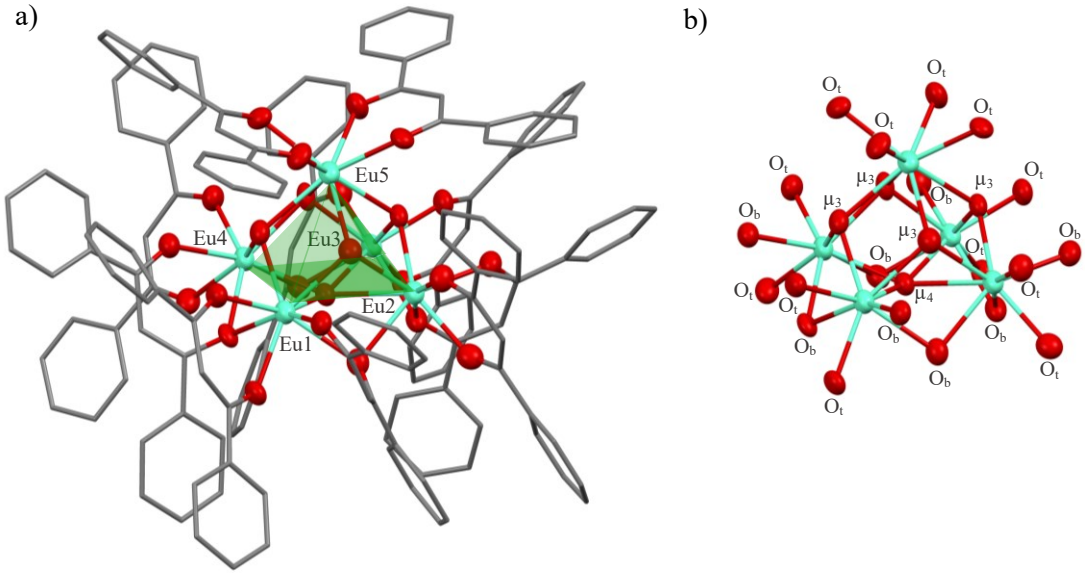

Figure 3.3. a) Structural representation of [Eu_5], seen along the b crystallographic axis. Colour code: C grey, O red, Eu light-green. Only Eu^{3+} atoms are labelled and the hydrogen atoms are omitted, for clarity. b) ORTEP perspective of the europium-oxygen core where ligands have been removed to highlight the squared pyramidal geometry. Only oxygens are marked according to their coordination mode (μ_3 and μ_4 belong to OH^- groups, O_t and O_b stand for the terminal and bridging chelations of DBM).

This discrete aggregate centrally accommodates five octacoordinated Eu^{3+} ions, located at the vertexes of a square pyramid. Specifically, the environment of the apical europium atom can be visualized as a slightly distorted square anti-prism, while the local symmetry of the four basal metals (labelled Eu1, Eu2, Eu3 and Eu4) is a bi-capped trigonal prism. The regularity of the entire pyramidal geometry is witnessed by the similarities in Eu–O distances, covering the range of 2.583-2.337 Å (a detailed list of the main internuclear distances is summarized in Table II in the Appendix).

As the distinctive coordinative ways of oxygen are concerned, a μ_4-OH group bridges all the four square-plane Eu^{3+} with an average bond length of 2.619 Å. The singular μ_4-OH bridging mode connecting basal lanthanoid ions was surprisingly noticed for the first time when this cluster was originally synthetized, whereas it is infrequently encountered in related *d*-block metal clusters.[32] Additionally, each basal ion joins two oxygen atoms from a bidentate dibenzoylmethanide unit, three from two bridging DBM

and, finally, two from μ_3-OH units. The top Eu5 atom, which lies on a four-fold symmetry axis, is instead bounded to four μ_3 hydroxyl groups and four bidentate *β*-diketonate ligands. Interestingly, the peripheral dibenzoylmethanide antenna overall displays a dual bonding interaction: four units participate with a (μ-O)-η^2-bridging chelating fashion and six are terminally bidentate (η^2-coordination). The triangular faces are formed by three metal ions linked together by μ_3-OH moieties, describing an average bond distance Eu–(μ_3-OH) of 2.393 Å. Then, each vertex Eu^{3+} is surrounded by three hydroxyl oxygens and four *β*-diketone oxygen atoms. The presence of hydroxy bridges originates from the starting lanthanide salt, $EuCl_3 \cdot 6H_2O$, whose more correct composition is embodied by the anionic species $[Eu(H_2O)_6Cl_2]^+Cl^-$: the action of the successively added basic reagent leads to a proton release from each water ligand, thus OH^- groups remain anchored to the europium centres.

Focusing on the Eu···Eu average distances, the basal ones revealed to be sufficiently shorter (3.635 Å) than the connection lying in the lateral edge of the pyramid (3.914 Å), in accordance to the trend individuated in the Yb and Er cluster (*viz.* respectively 3.7692 and 3.80 Å for atoms located at the side pyramidal part, while 3.4833 and 3.51 Å for those at the base vertexes).[147]

Globally, values of bond lengths and angles, which are presented in Table II of the final Appendix part, satisfactorily coincide with those reported for the earlier Eu_5 deposited structures and the isostructural compounds above-referred.

Looking at the intermolecular interactions in the packing network except van der Waals ones, no evidence of significant hydrogen bonding or π-π stacking was noticed.

Regarding the other structures, the green luminescent $[Tb_9Ti_2]$ crystals perfectly matched the recently-published orthorhombic compound defined by a *Pnna* space group.[110] The inner metal core $[Tb_9Ti_2(\mu_4\text{-}O)(\mu_3\text{-}OH)_{14}]^{19+}$ is disposed in a butterfly shape as the two cubane Tb_3Ti subunits associate. All around, seventeen acetylacetonate anions (showing a μ_1-η_1:η_1 and μ_2-η_2:η_1 kinds of chelation), two methoxide anions and three methanol ligands complete the coordination shell and counterbalance the positive charge to neutrality (check Figure 3.4 to have a look on its crystallographic organization).

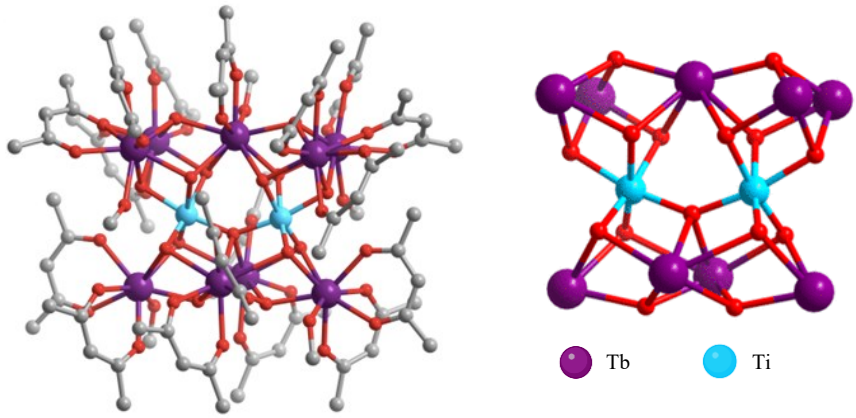

Figure 3.4. Ball-and-stick view of the crystal structure of [Tb_9Ti_2] on the left and the detail of its core on the right side. Carbon and oxygen atoms are represented with smaller grey and red spheres, respectively. The images were adjusted from ref.[110]

Instead, the cluster [Eu_4Ti_2] crystalizes into a monoclinic system with a $P12_1/n1$ space group. The elongated octahedral metal core contains the $[Eu_2Ti_4(\mu_2\text{-}O)_2(\mu_3\text{-}O)_4]^{10+}$ assembly where a discrete network of Eu^{3+}–O–Ti^{4+} connections are established with an average distance of 3.762 Å between the two metal cations occupying the core plane (the structural image is shown in Figure 3.5a). The absence of hydroxyl bridges in close proximity of the europium ions is supported by the Ti^{4+}: owing a high Lewis acidity and an intrinsically harder nature, titanium ions impart the preferential bridging coordination of O^{2-} respect to the OH^- groups.

Actually, four μ_3-O^{2-} anions indirectly mediate the connection between the four sixth-coordinated Ti^{4+} and the two apical Eu^{3+} ions along every side of the plane.

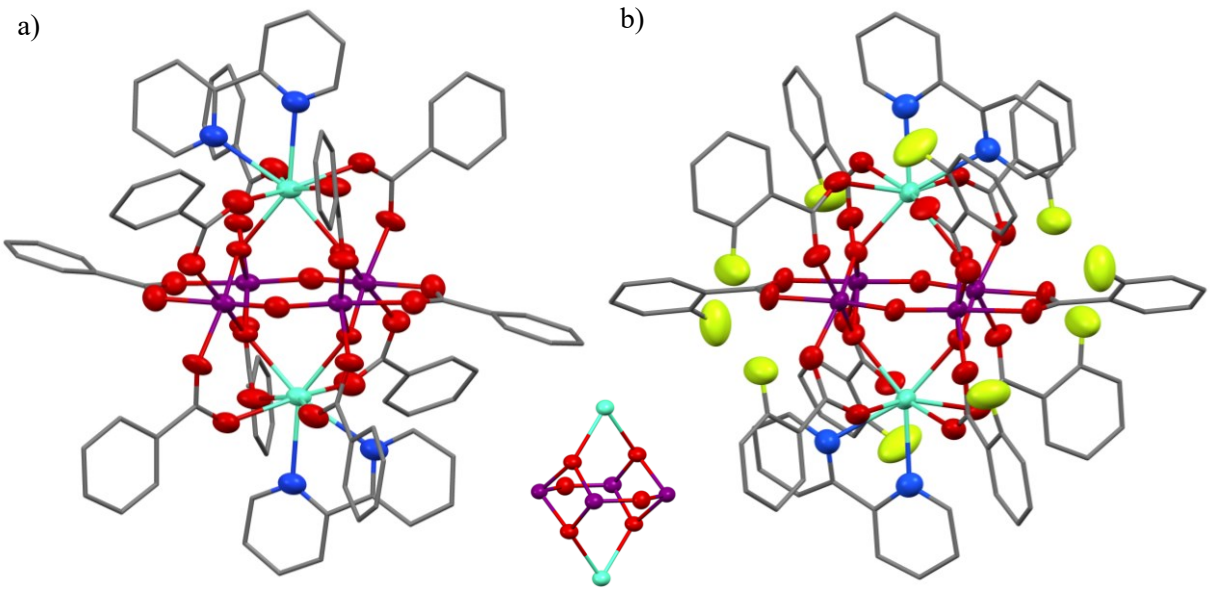

Figure 3.5. Crystal structures determined for [Eu_2Ti_4] (a) and [Eu_2Ti_4]^f (b). Colour legend: C grey, O red, N blue, F yellow, Eu light green and Ti violet. Hydrogen atoms have been omitted and all the non-carbon atoms are shown in ORTEP view for the sake of graphic clarity. In the central inset the Eu–O–Ti metal core is displayed.

The outer shell is protected and stabilized by coordination to oxygen- and nitrogen-donor ligands. Precisely, two N-donor bipyridine ligands and ten benzoates, both able to simultaneously exert an antenna effect contribution, are peripherally displayed.

Ultimately, inspection of the structure of the fair pink solvothermally-obtained [Eu_4Ti_2]^f crystals testified a triclinic $P\bar{1}$ motif, however with an atomic disposition equal to the previously one discussed (Figure 4.4b). The unique difference lies on the surrounding coordination sphere, where deprotonated 2-fluorinated benzoic acid moieties replace the benzoate ligands present in [Eu_4Ti_2]. As proven in Table IV of the Appendix section, all the bonds and angles between atoms inside the central core acceptably correspond to the unfluorinated analogue.

Both these latter structures adhere to the similar monoclinic and triclinic skeletons found for more complex chiral systems, likewise based on a carboxylate ligand and on an enantiomeric form of 4,5-pinene-2,2'-bipyridine.[144] Analogous Eu–O–Ti tridimensional scheme has been observed for cages containing Gd, Tb, Ce in place of europium and sheltered by diverse chelating ligands.[148]

The determination of their crystallographic structure reinforces the reproducibility of the related solvothermal procedures, but limits it solely to specific combinations of

derivatives of benzoic acid and differently functionalized bipyridine-like chromophores. If not, powders or unprecipitated products were obtained. In fact, the combinations between 2,2'-bipirydine with 1,4-benzenedicarboxylic acid and 2,6-difluorobenzoic acid, as well as the ones between carboxylic acid with 2,2'-bipyrimidine, 4'-(*p*-tolyl)-2,2':6',2''-terpyridine and 4-chloro-2,2':6',2''-terpyridine did not produce crystallizable and processable products.

Crystallographic tables with the details on all these europium crystal structures, along with tables showing the main bond lengths and angles are reported in the Appendix part.

3.1.3. Mass spectrometry analysis

The pentaeuropium oxocluster was examined via electrospray ionization mass spectrometry (ESI-MS) and its spectrum collected in the range 2000-3500 m/z is provided in Figure 3.6a.

Solutions with molar concentrations of *ca.* 10^{-4} M either in THF, chloroform and toluene were prepared and, since they revealed an analogous behaviour, only the analysis recorded for the THF solution is here presented and commented.

The molecular peak, estimated around 3077 m/z, was not identified due to the heavy tendency of the oxocluster to undergo fragmentation during the ionization process. As an example of signal assignation, the more relevant peak in terms of intensity falls at 2509.8 m/z and its associated experimental isotopic pattern is documented in Figure 3.6b. Here, the simulated profile pattern related to the monocharged $[Eu_4(C_{15}H_{11}O_2)_8(OH)_5LiNa]^+$ species is presented in red. This exemplificative fragment is indicative of the loss of one europium ion and two dibenzoylmethane ligands. A coherent agreement between the experimental and the calculated isotopic distributions was demonstrated, especially regarding the number of subpeaks and the whole fragmentation fingerprinting.

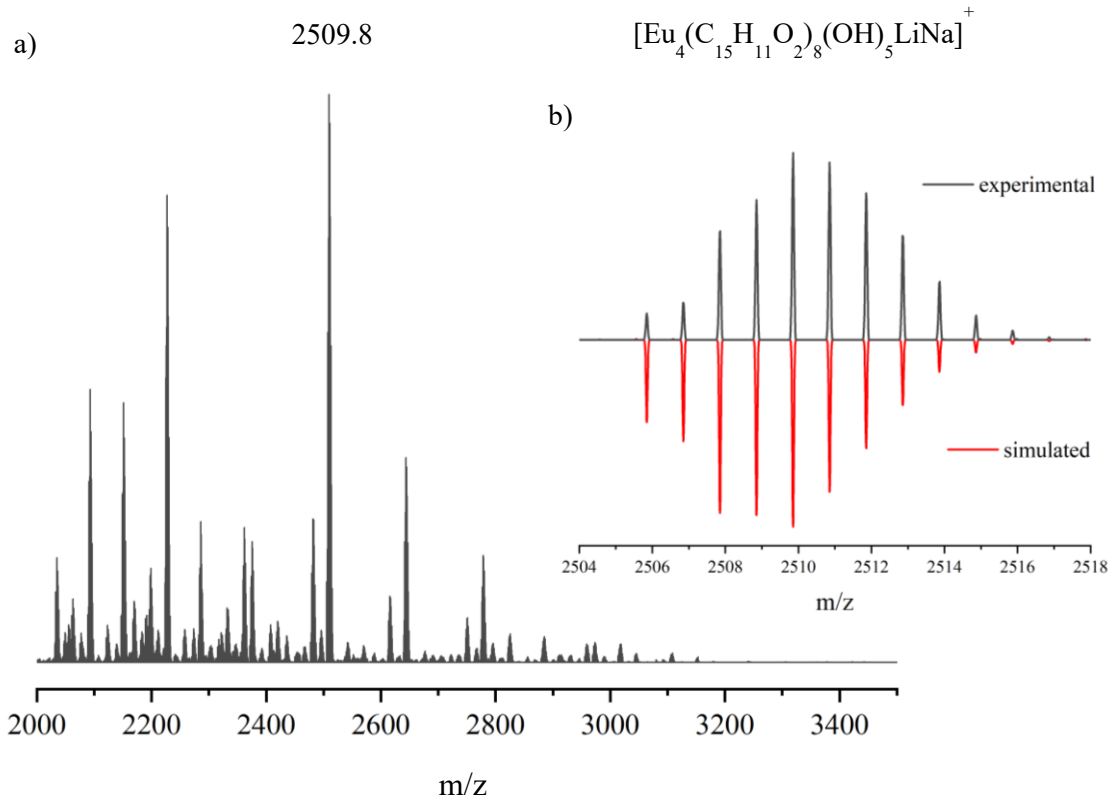

Figure 3.6. a) ESI mass spectrum in positive ion mode of [Eu_5] in THF. b) experimental (grey line) and simulated (red line) isotopic patterns of the peak intensity signal, reported in negative ion mode and centred at 2509.8 m/z.

3.1.4. Attenuated total reflectance FT-IR spectroscopy

Attenuated total reflectance FT-IR spectra have been acquired for the synthesized Eu^w, Eu^g, [Eu_5] powders and the pure HDBM ligand in the infrared region of 645-4000 cm^{-1}, as depicted in Figure 3.7a.

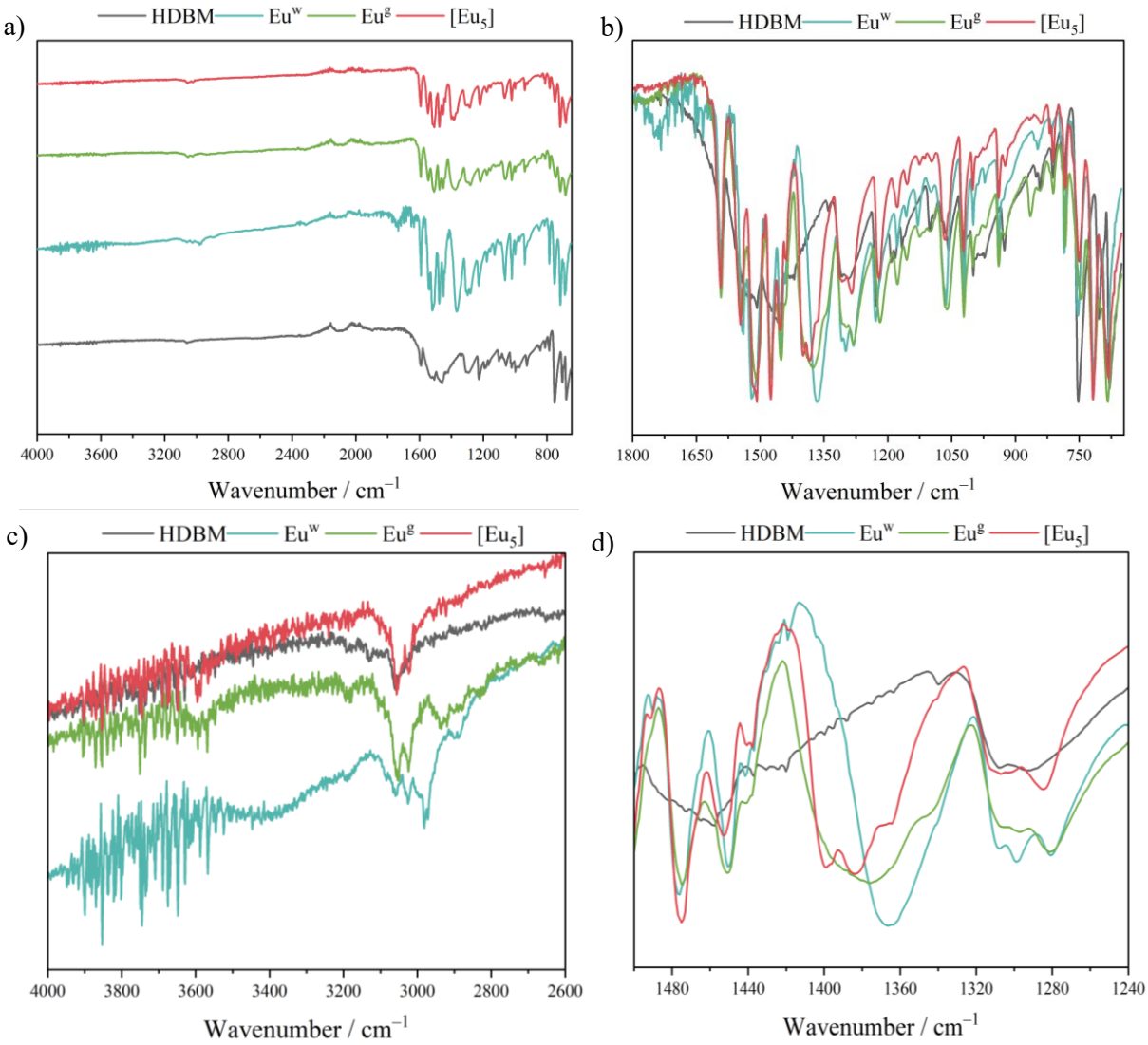

Figure 3.7. a) ATR spectra of solid state Eu^w, Eu^g, $[Eu_5]$ and HDBM in the infrared spectral domain. For ease of comparison, the spectra are shifted vertically. b) Normalized and superimposed ATR profiles in the zoomed 1800-645 cm^{-1} frequency frame. c) Expanded section of the 4000-2600 cm^{-1} range highlighting the broad signal of aqua ligands present in Eu^w and its absence in the other compounds' tracks. d) Enlargement of the 1500-1240 cm^{-1} region.

The region of major interest extends from 1800 cm^{-1} to the lower limit of the investigated window, where the respective spectral features of the different europium systems can be mostly compared (Figure 3.7b). In order to ascertain the nature of such species, the bands' assignment has been made through FT-IR characterizations of related compounds with corresponding nuclearity and similar coordinative spheres. All the three examined species showed similar profiles with minor differences compared to the free dibenzoylmethane ligand. These variations can be ascribed to the coordination

of the oxygen atoms to the europium ions. Indeed, as suggested by literature references, the characteristic peaks of the free ligand fall generally at longer wavelengths when included into lanthanoid complexes, in accordance with the changes in the enolate tautomer vibrations when creating a hexahydric ring chelation.[149]

The $\tilde{\nu}_{C=O}$ stretching vibration, representative of the diketonate antenna in the enol form, is detected at 1591-1593 cm^{-1}. It exhibits a narrow bandwidth, evidencing the enolic hydroxyl and carbonyl oxygens' donation towards the Eu^{3+} ions. This C=O signal feature is also distinctive of the expanded π delocalization in ternary complexes and clusters.[150]

Passing from the isolated ligand to the complexes of both degree of nuclearities, new features appeared in the vibrational spectra, whereas intensity and resolution of certain signals were enhanced. A broad and intense band in the 1399-1340 cm^{-1} region, absent in the HDBM spectrum, is exclusively attributed to the coordination compounds, as a single signal for the mononuclear complexes and as a barely discernible band structure for the multinuclear one (Figure 3.7d). This provides a useful diagnostic tool to differentiate oxocluster entities from their mononuclear counterpart, as formerly remarked.[145]

The only relevant frequencies in the infrared portion above 1800 cm^{-1} are the weak stretching of aromatic C–H bonds at 3100-2900 cm^{-1}, coming from the dibenzoylmethanide rings, which are better resolved into two peaks in the complexes and in the oxocluster (refer to Figure 3.7c).

Also, the large ligand band at 1494-1446 cm^{-1} is splitted into two components at indicatively 1476 and 1451 cm^{-1} for the europium species.

Focusing on the two mononuclear complexes, the broad O–H stretching band, spreading in the region of 3500-3290 cm^{-1} and attributed to the water's hydroxyls of Eu^{w}, disappeared in the ATR profile of Eu^{g} (Figure 3.7c). This evidence denotes that the bischelate dimethoxyethane has efficaciously replaced H_2O.

All the characteristic infrared bands of DBM bonding present in Eu^{w} are also met in Eu^{g} and [Eu_5] species, with their positions slightly shifted, some bathochromically and some hypsochromically, probably due to the ancillary ether influence and to the presence of an increased number of heavier atoms. Eu^{w} profile well fit the FT-IR response of the monohydrated $Eu(DBM)_3(H_2O)$ previously described in literature,[151] and, together with E^{g}, agrees with other reference lanthanoid DBM-based mononuclear complexes.[152]

3.1.5. X-ray photoelectron spectroscopy

X-ray photoelectron spectroscopy proved to be an extremely powerful tool for inspecting the identity of the obtained molecular systems. XPS analysis was carried out in the spectral portions of interest, *i.e.* O 1s, C 1s, and Eu 3d photoemission regions, and the determined atomic percentages were in good agreement with the expected composition and the literature analysis of similar structures based on different lanthanide elements.[153]

Concerning the qualitative identification in the O 1s and C 1s regions, a deeper investigation was attempted by a deconvolution procedure, revealing the underlying peaks' profiles which are hidden and superimposed in the total spectrum (see Figures 3.8 and 3.9b).

The O 1s signal of Eu^{g} is composed by a single peak indicating the diketonates' C–O groups (530.7 eV), whereas an additional one appears for the Eu^{w} and [Eu_5] species, characterizing the presence of water and hydroxyl-type oxygens, respectively.[154] Specifically, the Eu^{w} peak with binding energy (BE) of 532.7 eV identifies the coordinating water molecules, while the one at 531.9 eV [Eu_5] the bridging hydroxyl groups in the pentanuclear cage.

The absence in Eu^{g} of the characteristic peak belonging to the water's hydroxyl group clearly witnessed the ligand substitution between the two H_2O molecules and the bischelating dimethoxyethane ether.

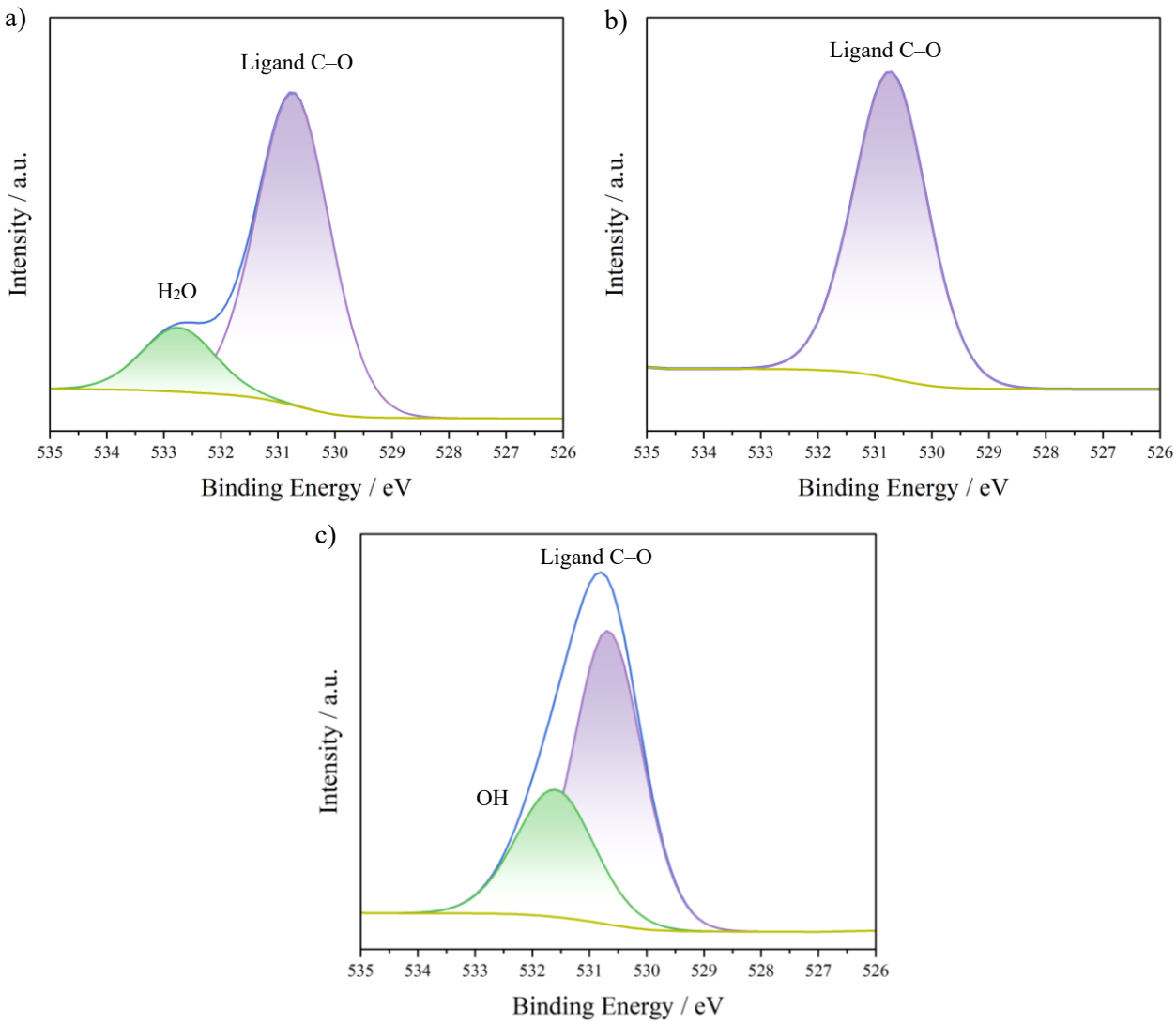

Figure 3.8. High-resolution XPS scans of the O 1s for Eu^{w} (a), Eu^{g} (b) and $[Eu_5]$ (c). Under the global fitting (blue solid line), the deconvoluted peaks ascribed to DBM (purple), H_2O or OH^- (green) stand out from the baseline (yellow track).

Figure 3.9 reports the stacked spectra and an example of peak fitting for the C 1s region. In all the three cases, the C 1s photoemission region was identified by a multicomponent intense peak, whose deconvolution revealed two spectral features, centred at the BE values of 284.3 eV (C_I) and 286.4 eV (C_{II}) and characterized by a significantly different intensity. The dominant lower energy component C_I is ascribed to the C=C/C–H bonds of the dibenzoylmethanide fragments, whereas component C_{II} is coherently associated to oxygen-bound carbon.[154] The intensity of the former BE peak is additionally affected by adventitious carbon's presence.[155]

A separated and low intense satellite peak extends at higher binding energies (291.1 eV), as expected for the π-π* shakeup, a signature typical of aromatic rings.

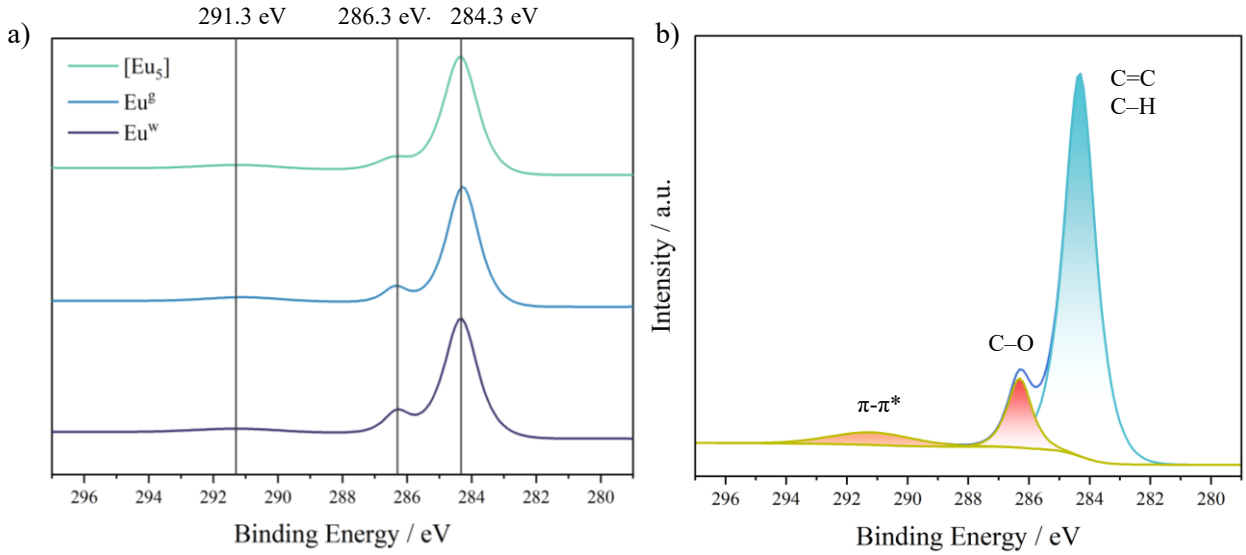

Figure 3.9. a) Normalized and stacked XPS spectra for C 1s of each compound, pinpointing the binding energy for the three peaks. b) High-resolution fitting of Eu^{w} C 1s as exemplificative of the deconvolution signals' analysis.

Considerations on the resemblances between all the samples' XPS spectra can be taken also for the Eu core-level profile, where the 3d orbital signal emerges from the baseline splitted into two separated peaks due to the spin-orbit coupling. This perturbation brings to two no-more degenerate states with total spin-orbital quantum number, *j*, of 5/2 and 3/2, whose maxima are positioned at 1134.1 eV and 1164.0 eV, respectively.[154] The spin-orbital splitting value for Eu^{3+} ions was found to be 29.9 eV. This evaluation and the binding energy values of the Eu 3d peak confirm unambiguously the europium +3 oxidation state. Furthermore, this BE finding was also consistent with the photoelectron outcome commonly found for europium(III) beta-diketonate species, as it is a function of the oxygen-donor ligand's nature.[156]

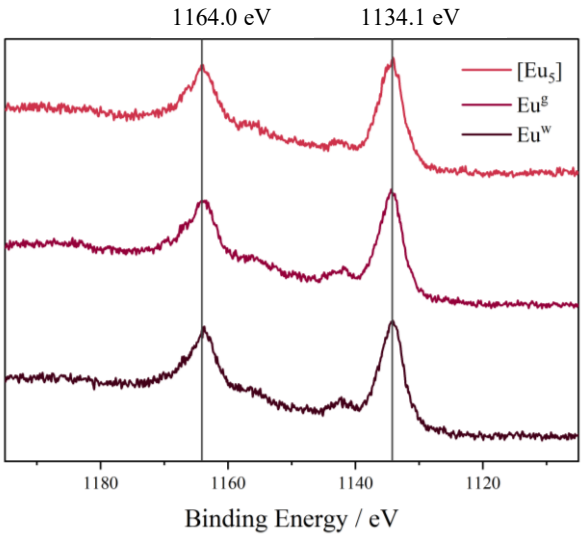

Figure 3.10. Array of the normalized Eu 3d XPS spectra of Eu^w (bottom line), Eu^g (central line) and $[Eu_5]$ (upper line).

The atomic ratios between the oxygen-containing moieties and europium ions inside each of the studied system were then determined and are shown in Table 1. The C 1s quantitative evaluation could not be performed because it suffers from an overestimation caused by adventitious carbon contamination.

As the stoichiometric europium-oxygen amounts are regarded, Eu^g satisfies the theoretical predictions of 1:2 ratio for the ancillary ether, but an unexpected 1:1.6 value was found considering the hydroxylic oxygens in Eu^w. This anomaly can be attributed to the coexistence of the monohydrated $Eu(DBM)_3H_2O$ and the dihydrated $Eu(DBM)_3(H_2O)_2$ complexes, eventually present in similar quantities.

Overall, the findings are consistent with the quantitative results of elemental analysis reported in the synthesis description of Chapter V.

Table 1. XPS compositional analysis, fitted parameters and Eu/O atomic ratio of the O 1s, C 1s and Eu 3d spectra of Eu^w, Eu^g and [Eu_5] compounds.

Sample	*Peak*	*Binding energy / eV*	*O/O ratio (calculated)*	*O/Eu ratio (calculated)*	*Group assignation*
Eu^w	O 1s	530.7	4.9:1 (3:1)	6.2:1 (6:1)	C–O
	O 1s	532.7		1.6:1 (2:1)	H_2O
	C 1s	284.3			C=C/C–H
	C 1s	286.3			C–O
	C 1s	291.2			π-π* satellite
	Eu $3d_{5/2}$	1134.2			
	Eu $3d_{3/2}$	1163.8			
Eu^g	O 1s	530.7		8.1:1 (8:1)	C–O
	C 1s	284.3			C=C/C–H
	C 1s	286.4			C–O
	C 1s	291.0			π-π* satellite
	Eu $3d_{5/2}$	1134.3			
	Eu $3d_{3/2}$	1164.1			
[Eu_5]	O 1s	530.8	3.9:1 (4:1)	4.1:1 (4:1)	C–O
	O 1s	531.9		0.9:1 (1:1)	O–H
	C 1s	284.3			C=C/C–H
	C 1s	286.4			C–O
	C 1s	291.1			π-π* satellite
	Eu $3d_{5/2}$	1134.0			
	Eu $3d_{3/2}$	1164.1			

3.1.6. UV-Visible absorption measurements

The room temperature absorption spectra of Eu^w, Eu^g and [Eu_5] in $CHCl_3$ solutions, whose normalized profiles are reported in Figure 3.11a, are equivalently dominated by a broad, lower-energy band due to the intra-ligand excitation $\pi \rightarrow \pi^*$.[157] This prevalent feature is centered at approximately 346 nm for both the mononuclear entities and for the pentanuclear oxocluster, corresponding to the absorption of the enol isomer of the

ligand.[149, 158] This singlet-singlet excitation extends roughly from 287 to 410 nm and shows essentially identical profiles for all the examined systems. Conversely, as anticipated from the inherently weak extinction coefficients associated with Eu(III) absorption, no discernible 4*f*-4*f* intraconfigurational transitions can be appreciated.

Nonetheless, the absorption spectrum of the free ligand (highlighted with a purple dashed line) presents a slight blue-shift with a maximum absorbance at 343 nm.[149] Overlapping the ligand absorption profile with those of the obtained europium compounds, the most notable difference observed is the flatter line shape in the 380-400 nm region. This is likely due to reorganization of the ligand's energy levels upon metalation, resulting in the appearance of shoulders at the less energetic edge of the UV absorption band in the spectra of the complexes.

Globally, the similarity between the absorption line shapes of the ligand and the europium compounds underlines that the coordination between the C=O groups and the heavy europium ions maintains unaltered the main electronic properties of the antenna moiety.

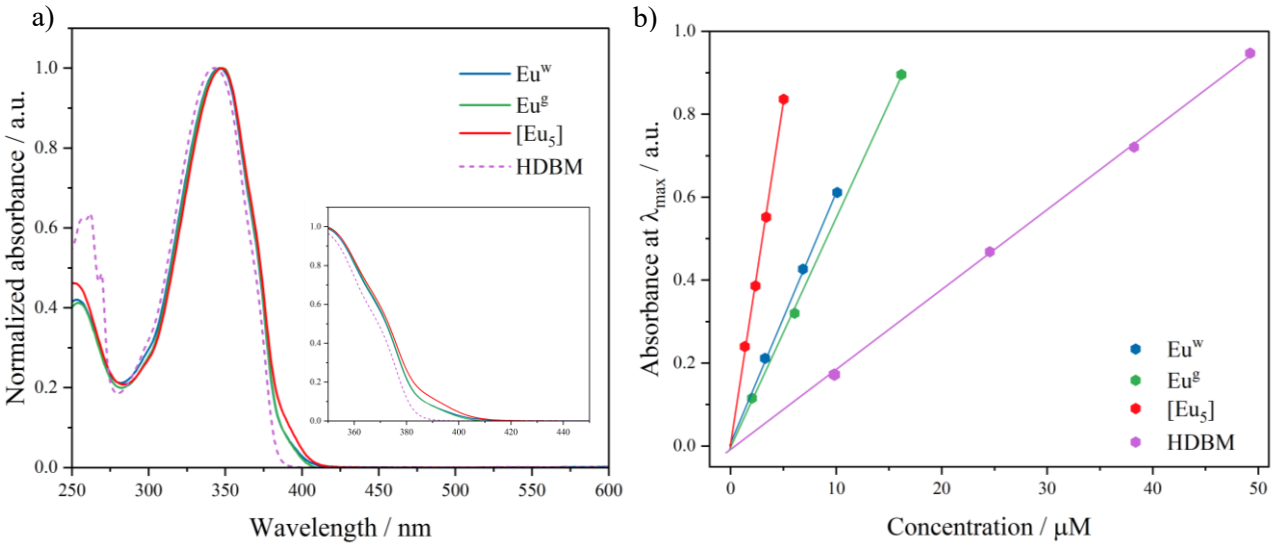

Figure 3.11. a) Normalized superimposed UV-Vis absorption spectra of the three Eu^{3+} compounds (solid lines) and of the uncoordinated ligand (dashed line) in chloroform solutions. Zoom of the bands' behaviour near the visible light end is given on the squared inset. b) Plots of the experimental correlation points between absorbance at λ_{max} and concentration, interpolated by a linear function. The R^2 values run around 0.99 for all the fitting curves and their slopes (ε) are listed in Table 2.

Recording absorption spectra on differently diluted solutions, it was possible to determine the molar extinction coefficients, ε, of the examined compounds. By linearly plotting the maximum absorbance at λ_{max} *versus* increasing concentration in the micromolar order of magnitude (Figure 3.11b), it was estimated an ε value for Eu_5 almost three times larger than those of the tris-β-diketonate E^w and E^g complexes, as foreseen from the higher number of chelating DBM units. Actually, as the steepness of the interpolation line demonstrates, an extinction coefficient of $166 \cdot 10^3$ $M^{-1} \cdot cm^{-1}$ was experimentally determined for [Eu_5].

Furthermore, since this strong molar absorption value at 347 nm resembles those reported for isostructural oxoclusters featuring different lanthanoid ions (with maximum absorption at 350 nm),[21] this empirical evidence further attested the formation of the Eu^{3+}-based oxocluster.

At variance, the mononuclear complexes exhibit ε values essentially three times higher than the one attained for HDBM, as predictable considering the number of ligand units in the systems.

The spectroscopic parameters are all together summarized in Table 2, while the individual absorption spectra varying with concentration are reported in the Appendix division. The relative errors on ε were computed from the interpolation fitting and are based on the absorption maximum for each compound.

Table 2. Molar absorption coefficients, ε, and their associated errors, $\delta\varepsilon$, calculated on the absorption maxima for the synthesized compounds and the pure ligand in solutions of $CHCl_3$.

Compound	λ_{max} / nm	$\varepsilon \cdot 10^3$/ $M^{-1} \cdot cm^{-1}$	$\delta\varepsilon \cdot 10^3$/ $M^{-1} \cdot cm^{-1}$
HDBM	343	19.1	0.1
Eu^w	346	61.3	0.7
Eu^g	346	55.1	0.5
[Eu_5]	347	166	1

3.2. Thin films deposition

After confirmation of the identity of the selected compounds, their pure powders were processed with the aim to turn them into more manageable and device-like samples.

Purposely, a geometry of flat layers with a 25 cm^2 superficial area was chosen to develop functional luminescent materials either for non-contact thermometers' and solar concentrators' applications. To this aim, we adopted the sample dimensions collectively suggested for an LSC prototype on laboratory scale[159] and studied the temperature-dependent photoluminescence behaviour.

Generally, even if the foremost challenging task for these films' preparation is represented by the processing itself, it is important to find a proper polymer and a mediating solvent which is able to disperse both the constituents of the composite material.

In our case, information regarding the choice of the polymeric matrix and the dissolving agent were taken from previous studies conducted by our research group.[160]

The dispersion of the luminophore into the appropriate matrix was accomplished by initially modelling the hybrid-composition material into a liquid coating, meticulously deposited onto a glass support to form a micrometric thickness layer. Polymethylmethacrylate (PMMA) was employed as host medium for the casting film procedure, considering its several appealing characteristics, suitable for the molecular thermometry and LSC requirements. The wide-spread and benchmarked use of this polymeric medium in doped materials is interrelated to its beneficial features, like commercially availability, inexpensiveness, promotion of lanthanide-based complexes' dispersibility, optimal photostability and high mechanical strength.[128] Its exceptional near optical transparency (above 300 nm) in the ultraviolet and visible ranges makes it suitable for not hindering lanthanoid-containing complexes' absorption. In addition, this polymer begins to reabsorb light in the remote infrared region, far beyond the emission lines of Ln^{3+} systems which can be clearly distinguishable.[161]

Hence, the choice of PMMA as the dispersion matrix was motivated by its ability to preserve the luminescence properties of the dispersed europium-based structures,[33,162] at variance to other common polymers, like polyethylene, that can affect their nature.[163] Moreover, its modest glass-transition temperature, T_g, of 105 °C allows to reach a good temperature frame for thermometric practicality and to sufficiently support hot weather conditions, indispensable for the outdoor use of LSCs panels.

Table 3. Selected physical properties of polymethylmethacrylate. Unless otherwise cited, data are reported as declared by suppliers.

Polymer	*M.W.* / g·mol^{-1}	T_g / °C	T_m / °C	η_{rid} / cm^3·g^{-1}	*n*	$\lambda_{cut\text{-}off}$ / nm
PMMA	350 000	105	320	150-160	1.49	330[164]

3.2.1. The casting method description

A literature-consolidated protocol was customized for the realization of thin polymeric layers and successively optimized to better revise the aesthetic aspect of them. Among the viable reference methods, a drop casting technique from chloroform solutions was adopted to primarily manufacture pristine PMMA samples, before starting to prepare the doped ones.[165] According to this procedure, the polymer is dissolved in a compatible solvent and the resultant solution is poured onto a supporting substratum, left expanding on it and solidifying via solvent evaporation to possibly generate an adhered or a free-standing film. Chloroform was preferred as intermediating solvent because of its uppermost compatibility with PMMA and the synthesized europium species.

Previous studies in our laboratory have been dedicated to evaluate the optimal polymer:solvent ratio in order to achieve a degree of volume and viscosity that contemporarily could balance the need of gradually spreading the solution and covering the entire area of the underlying plate.[160]

A high concentration of the polymeric material can result into inhomogeneous and reduced-extension patches along the substrate surface, with the eventual retention of air bubbles or accidental accumulation of clumps. To minimize these high-density issues, diverse weight concentrations have been explored for casting validation. From earlier attempts, it has been tested that, expressly for PMMA in chloroform, weight concentrations ranging from 7 % to 14 % resulted the ideal option to be employed. Therefore, it was selected a fixed amount of polymer (0.500 g), an optimal quantity also to be further combined with lanthanoid-including luminophores.

In the preliminary step of the fabrication of the casted layers, efforts were committed to progressively adjust some technique parameters to ideally obtain a flawless coating, with highly uniform texture and regular boundaries.

Quadratic-shaped glass tiles of 5.0 x 5.0 cm^2 surface area and 0.3 cm thickness were used as casting supports to guide the production of equal-sized films. These glass slides were horizontally anchored to Petri dishes with strips of paper tape, properly arranged all around their edges (see Figure 3.12 to appreciate the setting). This supplementary glassware is also advantageous to eventually collect the solution that might overflow from the lateral parts of the material.

The parallel inclination of the glass slabs respect to the countertop was checked before starting the casting operation. Apart from choosing suitable flattest Petri dishes, an accurate levelling of the plane and the compensation of eventual one-sidedness with pieces of paper were ensured. Otherwise, even tiny asymmetry might cause the immediate or while-drying flow of the solution over the substrate's perimeter.

Afterwards, the PMMA solution was poured from the vessel directly onto the glass base, beginning from the central region and steadily covering the external ones, until a homogeneous liquid stratum was obtained. Care was taken for not spilling the solution off the glassy block's sides, an inconvenience that would generate random-thick materials.

A pre-treatment of the glass slates with an aqueous hydrochloric acid solution managed to reinforce the adherence of the final film to the glass underneath, to contain the solution mobility and to circumvent future detachment from the support.

However, shortcomings have been met and bypassed in obtaining visually satisfying surfaces. The utmost way to realize plane and uniform films is to operate inside a climate chamber, perfectly cleaned and with a rigid atmospheric control to keep the material from dust deposition or other contaminations. Nevertheless, slow and ambient drying conditions have resulted adequate to accomplish the desired material's features: since the rate of solvent removal governs the final surface quality, enclosing the casting equipment with a proper shelter is a critical passage. It has been noticed that the use of aluminum foil of dimensions reasonably larger than the dish circumference to complete the aforementioned function caused random surface undulations. This made hard to control the uniformity of the film and facilitated air penetration beneath it. Beyond aesthetic matters, scattering and refraction phenomena could also arise while a bumpy material is subjected to an electromagnetic field and could affect the optical performances for which it is intended.

The encounter of pronounced surface defects has then required to thought at further procedure's refinement in order to attain reproducible smoother layers.

Hence, with the purpose of minimizing surface corrugations and roughly control the kinetic of polymer solidification, the solvent evaporation time was delayed, sealing the casted plates with funnels. At the beginning, the ones equipped with a large opening covered with a holed aluminum sheet were used. Though, those with a thinner neck occluded by a cotton swab revealed to be a better solution (photographs of the home-made casting apparatus are pictured in Figure 3.12).

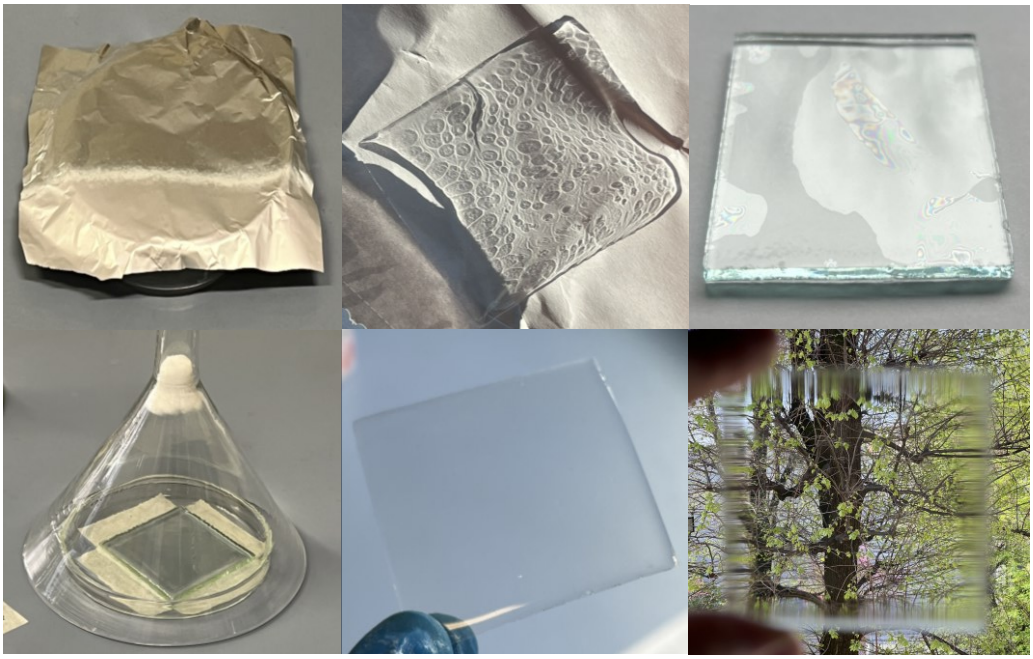

Figure 3.12. Pictures of stages and issues of the pure PMMA film making: the upper line attested the superficial imperfections and self-detachment of the film when adopting the aluminum-sheet-coverage method; in the lower line the improved method with a cottoned funnel cover, the resulting detached film and the visibility through it are shown.

Wholly, the interplay of these expedients was found to be qualitatively effective in preparing regular-shaped, partially flexible and evener materials all over their entire area.

The release of PMMA films from the glass plate was easily succeeded in a couple of minutes via sonication, while other samples were intentionally retained adherent to be later used as undoped benchmark for optical and electrical characterizations.

Thickness values were gauged with a micrometer along the central and peripheral sections of the film surface giving an average depth of 220 micrometers (± 13 μm), accompanied by an inhomogeneity extent of 5 % at most throughout the sample.

3.2.2. Luminescent polymeric films

Incorporating guest functional molecules into a proper substrate that does not interfere with their optical and structural properties is of paramount importance to ideally preserve, or at least marginally undermine, the luminophores' integrity and their light-interaction behaviour.

The settled casting methodology was replicated to make the doped PMMA films: their preparation consisted of simply blending the desired weight content of the luminescent species with the same fixed amount of PMMA previously identified for pure polymer samplings and using chloroform as solvent. It was possible to maintain unchanged the solvent choice, as it possesses likewise compatibility with the synthesized lanthanoid structures. Already-verified dopant concentrations for related europium systems (explicitly, binuclear Eu^{3+} quadruple-stranded cages bearing bis-β-diketonate ligands) were taken for grant to design the desired hybrid films.[130]

As the order of components addition is concerned, it was preferable to add the assessed polymer amount to the luminophore's solution while carefully tilting the vial to sidestep the formation of PMMA's hindering clumps at the interface. Although the monometallic species displayed instantaneous solubility in the mediating solvent, it took approximately one hour to the pentanuclear oxocluster to uniformly solubilize.

The last refined solvent-drying technique was efficiently employed to produce homogeneous and adhered doped films, without superficial defects.

As underlined before, it was more convenient to project a 5 x 5 cm^2 casting due to the fact it is simultaneously conforming to ordinary LSCs' laboratory volume scale and practical to derive smaller portions for LMTs assessments.

Moreover, particularly for the prior applicative purpose, aiming to obtain greatly transparent, neutral-colour devices is recognized as a fundamental aesthetic requisite if the concentrator is destined for not arty installations.[141]

The luminophores' concentrations based on the introduced polymer weight, namely 0.5, 1.0 and 2.0 % w/w (see Table 4), were thus chosen to respect these exterior qualities and their solubility capacities.

Table 4. Experimental information regarding luminophore weight concentrations (w/w_{PMMA}), Eu^{3+} molar contents (n_{Eu}), volume of the entire material (V_{film}, assuming quadratic side of 5 cm), average film thickness measured with a multimeter (d) and molar concentration of the luminophore respect to the film volume (C_M^{lum}) for the doped PMMA samples.

Emitter	w/w_{PMMA} / %	n_{Eu} / mol·10^{-6}	V_{film} / cm^3	d / μm	C_M^{lum} / mol·L^{-1}·10^{-4}
Eu^w	0.5	2.9	5.7	227	5.1
	1.0	6.0	6.1	245	9.7
	2.0	12.7	5.5	221	21.1
Eu^g	0.5	2.7	5.9	237	4.9
	1.0	5.6	5.1	205	10.9
	2.0	11.1	6.2	250	17.5
$[Eu_5]$	0.5	4.0	5.2	210	1.6
	1.0	8.0	6.0	239	2.7
	2.0	16.5	6.3	251	5.2

It is worthwhile that the doped films did not manifest any macroscopic deposits of luminophore inside the polymer guide, suggesting that higher weight quantities can be explored in future studies, before reaching the saturation limit of the compounds.

All films embedding Eu^w, Eu^g and $[Eu_5]$ at the selected concentrations showed the peculiar red luminescence of europium(III) under a UV radiation centred at 365 nm (Figure 3.13).

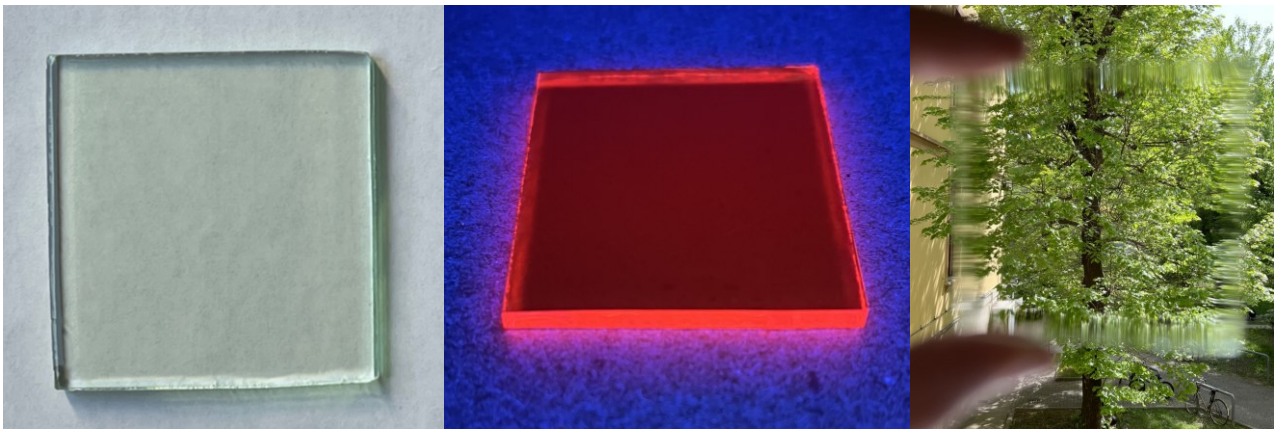

Figure 3.13. Digital photographs of an exemplificative casted film containing [Eu_5] at 2.0 % by weight of PMMA: on the left under natural light conditions, in the middle under 365 nm illumination (light source: Spectroline® E-Series UV Hand Lamp with Longlife™ filters), and on the right its eye-perceived transparency and colour neutrality under daylight.

3.3. Hybrid films characterizations

In the following subparagraphs, the materials' characterization results are discussed, from light-matter interaction measurements to functional properties under temperature and voltage changes. For the sake of brevity, the films will be, from here on out, renamed as Eu^{wy}, Eu^{gy} and $[Eu_5]^y$, where the apex *y* highlights in turn 05, 1 or 2 depending, respectively, on the luminophore's content among 0.5 %, 1.0 % and 2.0 % by weight.

3.3.1. Photophysical behaviour

Room temperature absorption, excitation and emission behaviours of the supported films in the UV-Vis spectral region have been investigated, as well as their photoluminescence lifetimes. The absorption profiles were not informative due to saturation reasons, attributable either to the elevated extinction coefficients of the entrapped luminophores and to their high loadings. Remarkably, this strong absorption capacity is, though, a sough-after prerequisite to develop an efficient luminescent solar concentrator.

No additional signatures were seen in the spectral region up to 800 nm, confirming the ascription of the absorption features exclusively to the europium-based emitters, without

interference from the host polymer. Also, the absorbance spectrum of the pure PMMA film was recorded, denoting optimum transparency down to 300 nm.

Assuming that the encapsulation process did not compromise the optical properties of the molecular guests, photoluminescence (PL) and photoluminescence excitation (PLE) spectra of the casted films were acquired and compared with those of their respective chloroform solutions. In this way, further inspections concerning the luminophores' integrity and chemical inertness upon embedding were captured.

When illuminated with ultraviolet light, all the films, as well as their pure precursor compounds, exhibited a bright-red luminescence, thanks to the efficient sensitization ability of the dibenzoylmethanide units. Actually, the photoluminescence responses showed that their antenna sensitized emissions (λ_{exc} = 380 nm which is near the maximum resultant from the excitation spectra portrayed in the insets of Figure 3.14) are all dictated by atom-like bands deriving from $^5D_0 \rightarrow {}^7F_J$ (J = 0-4) transitions, distributed in the visible light domain.

On the whole, the emission spectra were found to be identical for all the Eu^{3+}-doped materials with their line shape mainly dominated by the hypersensitive electric dipole $^5D_0 \rightarrow {}^7F_2$ transition at 611 nm, responsible for the red colour emission. The maxima of the other bands are placed at 578, 586-599, 647-657 and 700 nm, respectively related to the $^5D_0 \rightarrow {}^7F_0$, $^5D_0 \rightarrow {}^7F_1$, $^5D_0 \rightarrow {}^7F_3$ and $^5D_0 \rightarrow {}^7F_4$ transitions.

The intensity ratios and the shape of the involved multiplets are typical of europium β-diketonates and are demonstrative of low local symmetry around the lanthanide center,[55] which is consistent with the structural evidences of [Eu_5].[166]

Considering that the Eu^{3+} ion act as a spectroscopic probe for its local environment's modifications and observing a good superimposition between films and solution PL spectra for each complex (refer to Figure 3.15), we can hypothesize that their coordination spheres remain intact when the complexes are embedded in the materials.

It was already found in films developed for similar europium complexes that the number and position of these emission bands, along with their intensity distribution, are preserved by using PMMA.[167, 168]

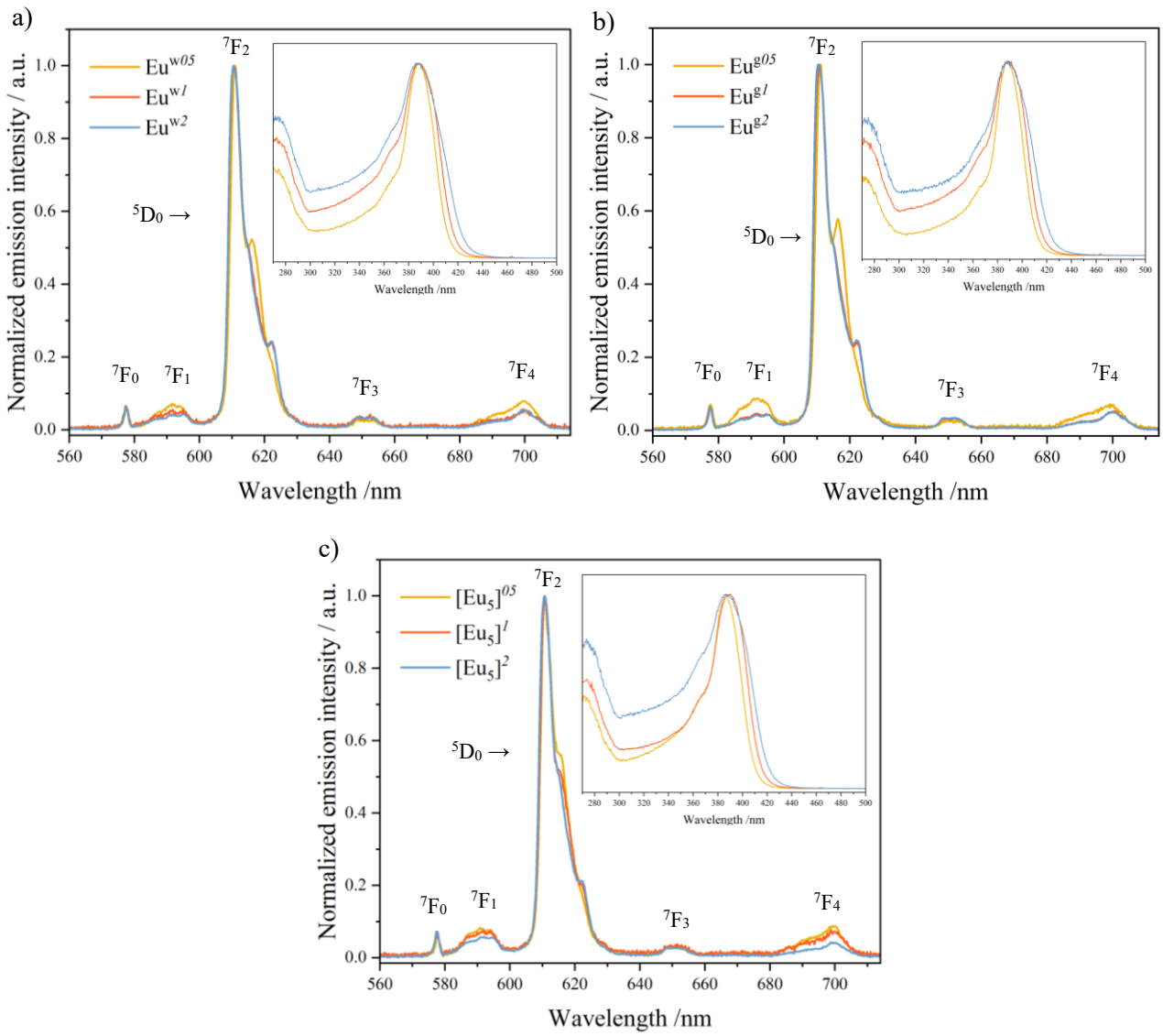

Figure 3.14. Luminescence (λ_{exc} = 380 nm) and excitation (λ_{em} = 612 nm, insets) spectra of Eu^{w} (a), Eu^{g} (b) and [Eu_5] (c) films varying the weight concentration.

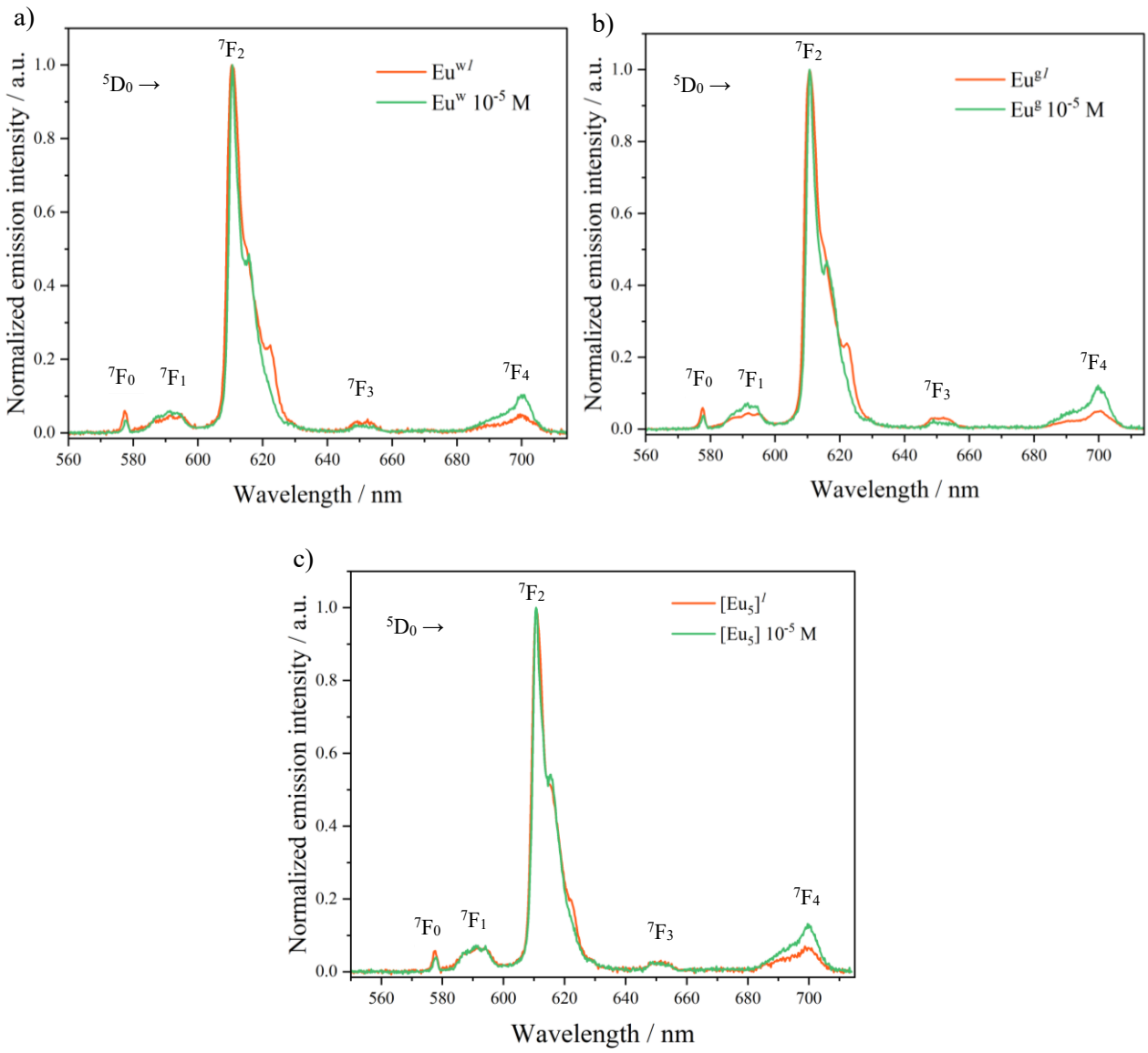

Figure 3.15. Normalized superposition of photoluminescence spectra of Eu^w (a), Eu^g (b) and $[Eu_5]$ (c), when doped in PMMA films (1 % by weight, orange line) and solubilized in chloroform (10^{-5} M, purple line).

The excitation spectra of the doped films, monitored at 612 nm, displayed a broad band in the 300-450 nm range, whose bandwidth tends to increase with the content of the luminophore.

The excited state lifetimes, listed in Table V (Appendix section), were derived from time-resolved $^5D_0$ decays curves and took values around 182-231 µs, regardless of the nature and concentration of the species.

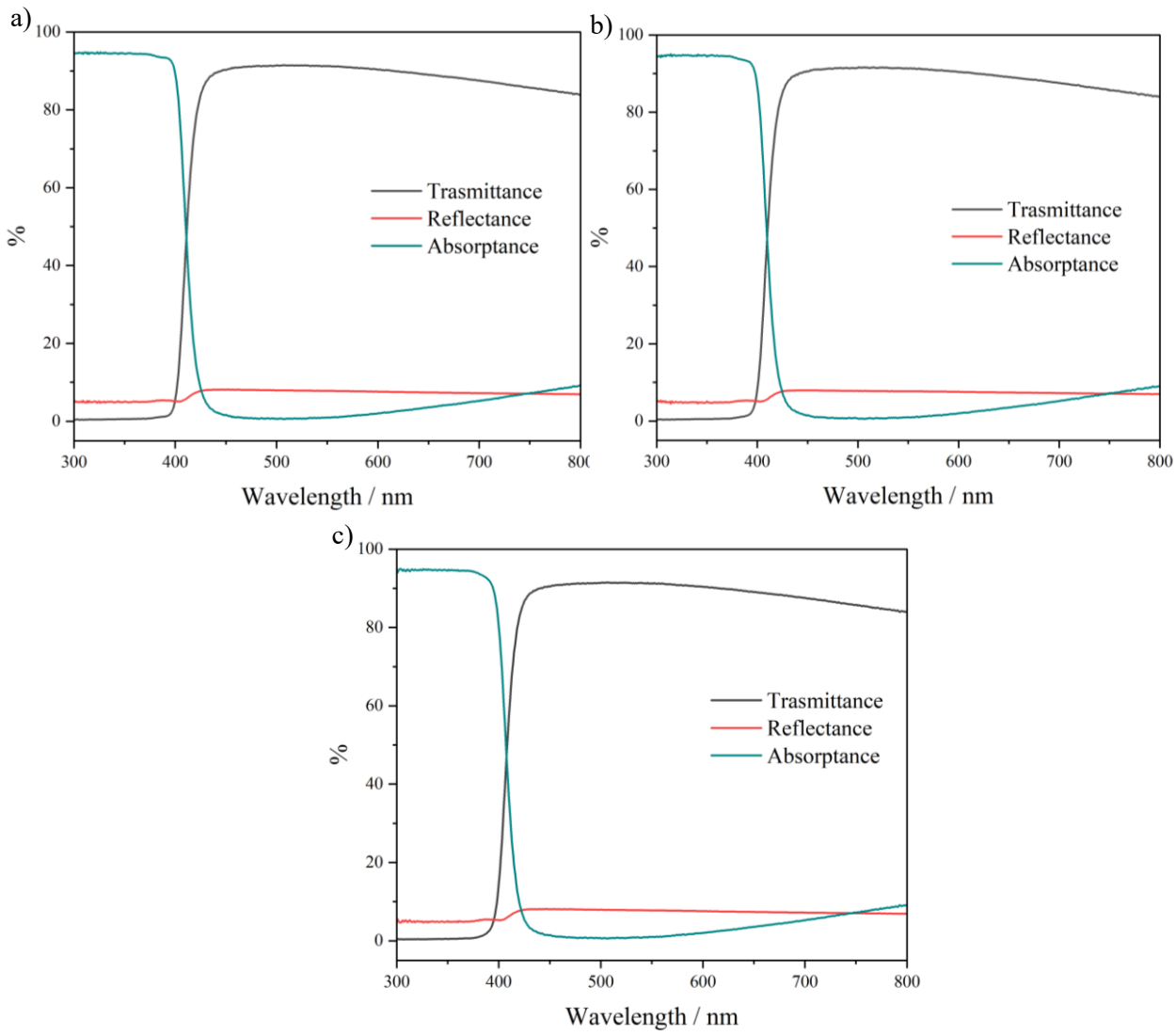

Figure 3.16. Superimposition of transmittance, reflectance and absorptance curves recorded for Eu^{wI} (a), Eu^{gI} (b) and $[Eu_5]^I$ (c).

Finally, the interaction of the materials with incident light was quantified in terms of diffuse reflectance and scattered transmittance.

In the 300-380 nm range, where the absorption bands of the DBM ligands are located, the transmittance is null. The $T_{\%}$ profile begins to raise at approximately 380-400 nm, then steeply reaches its maximum value at 420-440 nm, after which absorption is no longer the prevailing phenomenon.

The long-wavelength portion of the transmittance band is described by a flatter and smoother profile, except for the final section where a decrease in its percentage appears, as expected from the behaviour of pure glass.[169] Nonetheless, a transmittance greater than 92 % cannot be achieved due to the reflections occurring at the air/glass interface.

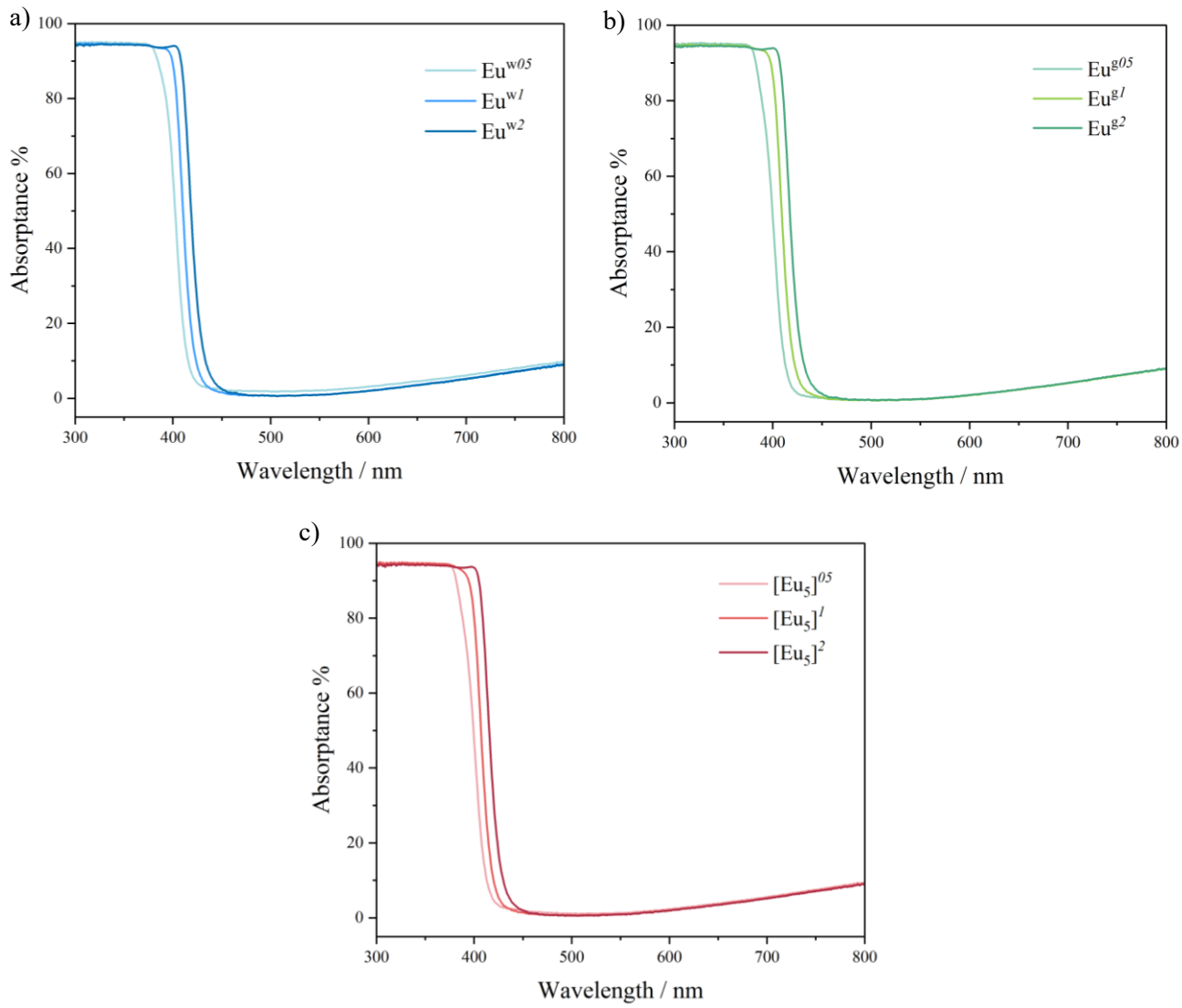

Figure 3.17. Absorptance spectra for Eu^{w} (a), Eu^{g} (b) and $[Eu_5]$ (c) films varying the weight concentrations.

Moreover, as demonstrated in Figure 3.16 and in the Appendix, increasing the luminophore content induced a slight bathochromic shift and a minimal enlargement in the zero-transmittance interval.

Instead, the reflectance signals attested the magnitude of incident light lost by reflection from the material's surface, so the minor possible value was preferred for the purposes of this thesis. Experimental evidences indicated a little increment in reflectance above 400 nm, while a residual value of approximately 4.5-5.5 % remained along the luminophore's absorption wavelengths. This constant contribution is entirely due to the presence of an air-sample interface encountered by the incident light during its propagation.

The absorptance curves were indirectly derived by subtracting the $T_{\%}$ and $R_{\%}$ plots from its ideal starting value of 100 %, according to the expression $A_{\%}(\lambda) = 100 - T_{\%}(\lambda) - R_{\%}(\lambda)$, thus leading to the resulting complementary spectra presented in Figures 3.16 and 3.17. In this latter graph ensemble, the absorptance shift towards higher wavelengths with increasing luminophore amount can be clearly seen.
Overall, these data emphasized the evidence that the host matrix and the light-material interaction do not impart any alteration to the optical behaviour of the dispersed fluorophores, reducing to the minimum unwanted reflection and transmittance effects.

3.3.2. Luminescent thermometric properties

Temperature dependent photoluminescence of the embedded molecular structures were investigated to determine their potential role as luminescent molecular thermometers. Consequently, emission spectra of the realized films containing different amounts of the luminophores (0.5, 1.0 and 2.0 % by weight of PMMA) were recorded in the 83-333 K temperature window, employing an excitation wavelength of 375 nm.
In Figure 3.18, temperature-dependent PL spectra for the $[Eu_5]^1$ film are reported. Irrespective of their composition (luminophore type and concentration), all the samples displayed a comparable behaviour. Therefore, general considerations valid for all the multifunctional materials will be drawn.
The recorded spectra showed the typical $^5D_0 \rightarrow {}^7F_J$ (J = 0-4) Eu^{3+}-centered transitions. The more the temperature decreases, the more the emission intensity of the Eu^{3+} ions increases. By lowering the temperature, thermally activated non-radiative deactivation channels became less favourited and emission intensity increases.[43]
Overall, the spectral profiles and the peaks' positions remained unaffected, demonstrating that the temperature variation did not induce any structural perturbations.
As specified before, square pieces measuring 1 cm^2 were obtained cutting the original detached films, so to ensure a better fit within the sample holder, as pictured in the insert of Figure 3.18a.

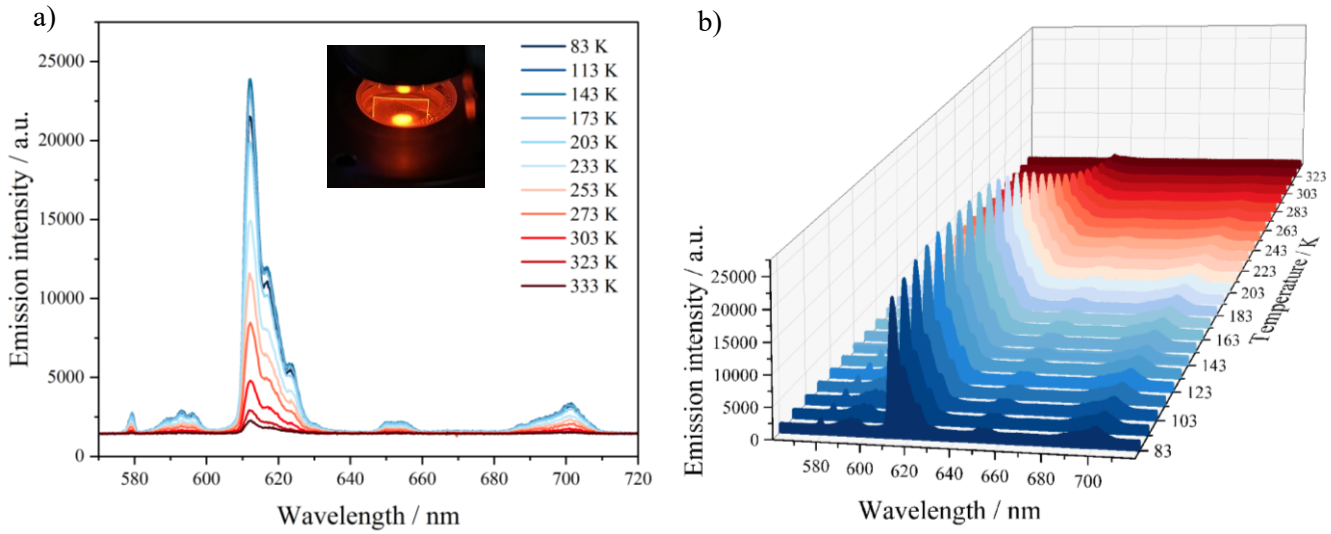

Figure 3.18. a) Superimposition of photoluminescence spectra recorded at different temperatures of $[Eu_5]^{1}$. A step of 30 K is on purpose chosen for the sake of pictorial clarity, with the addition of the zero- and the hotter temperature records. b) Three-dimensional perspective of the PL curves for the entire investigated temperature interval. The blue-red colour nuances intuitively obey to the temperature scale.

The integrated emission intensity of the most intense $^5D_0 \rightarrow {}^7F_2$ transition was chosen as the experimental thermometric parameter, Δ (see Chapter I, Paragraph 1.3.1 for its significance).[96] All the intensity-based calibration curves are provided in the Appendix division, which have been normalized to the maximum photoluminescence intensity in order to be compared. The Δ *vs* T curves are scarcely affected by the sample composition, indicating that the thermometric response is not significantly influenced by the quantity of emitters and, subsequently, by the presence of a diverse ancillary ligand. It is worth to note that all the examined compounds contain the same β-diketonate ligand (DBM).

These curves describe a sigmoidal shape but deviate from their plateau course at the lowest temperature values, approaching the cryogenic extreme. The drop at 83-132 K is barely noticeable respect to the more pronounced decline starting approximately from 190 to 310 K.

As defined in the Introduction, the S_r parameter ($= \frac{1}{\Delta}\left|\frac{\delta\Delta}{\delta T}\right|$, *Eq.2*, Chapter 1.3.1.) permits to compute the relative thermal sensitivity.[96]

Looking at the graphs in Figure 3.19, S_r exhibited values major than 1 % · K^{-1}, the threshold identifying a good thermomether,[88] approximately from 220 K to 320 K. Interestingly, the higher S_r values are observed in the physiological temperature range. In detail, Table 5 presents the temperature values at which each film exhibited a relative sensitivity greater than unity ($T_{Sr=1}$) and their respective maximum S_r value (S_m).

Table 5. Relevant thermometric data, extracted from the S_r *vs* T curves, for the analyzed doped films.

Sample	$T_{Sr=1}$ / K	S_m / %·K^{-1}	T_{Sm} / K
Eu^{w05}	221	4.0	313
Eu^{w1}	214	4.9	313
Eu^{w2}	215	5.0	313
Eu^{g1}	217	4.8	313
Eu^{g2}	214	4.4	313
$[Eu_5]^{05}$	220	4.3	313
$[Eu_5]^{1}$	219	4.3	313
$[Eu_5]^{2}$	225	5.0	313

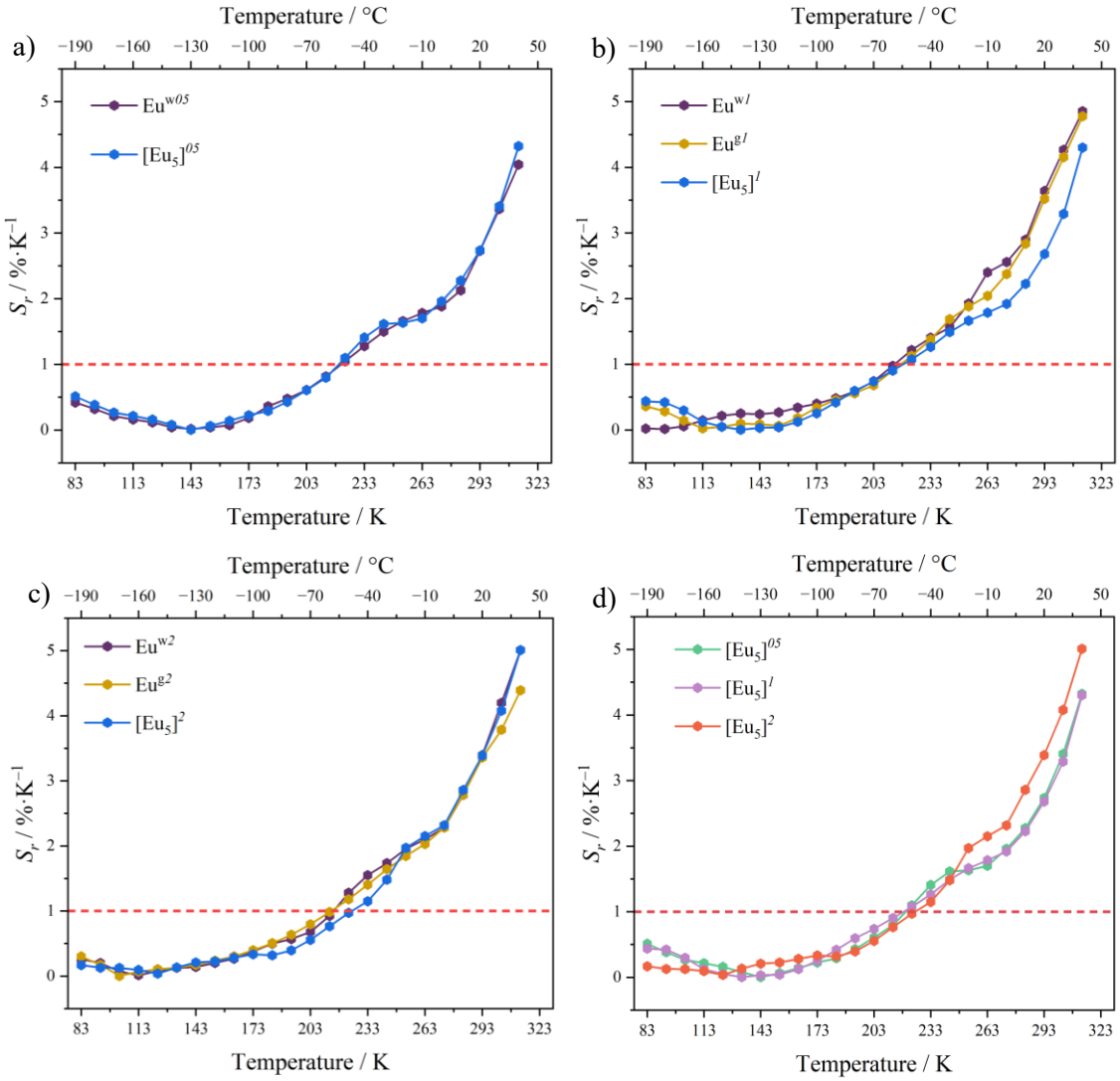

Figure 3.19. a), b), c) Comparison of relative thermal sensitivities for doped films at different weight contents. In the first chart, the Eu^{g05} plot is omitted since, due to sample's damage, its curvature deviated strongly from the ones of the other films with the same concentration and could not be considered as a valid result. d) Variation of the S_r *versus* T curve with the luminophore concentration for [Eu$_5$] films. Analogous sets for the remaining films are given in the Appendix.

Globally, all the characterized films showed a similar S_r behaviour and reflected the trend previously observed for the dimeric complex [Eu$_2$(DBM)$_6$(pyrzMO)$_2$] (where pyrzMO specifies pyrazine *N*-oxide) referring at almost the same temperature interval.[170]

Given that the variation of the ancillary ligand does not influence the thermometric properties of the Eu^{w}, Eu^{g} and [Eu$_5$] films, it is probable that the dibenzoylmethanide

ligand is the key fragment governing the thermometric behaviour. Eu^{w2} and $[Eu_5]^2$ samples displayed the highest S_m values of 5.0 % · K^{-1} at 313 K.

These findings evidence the practical usability of these materials as non-invasive luminescent thermometers, particularly within the biologically relevant temperature range of 200-300 K, where a high resolution is required.

3.3.3. Preliminary LSC functional studies

The fabricated materials can also be exploited as luminescent solar concentrators. In this prospect, current-to-voltage (I-V) and power-to-voltage (P-V) characteristic curves of LSC devices consisting in photovoltaic silicon cells edge-coupled to the concentrator were evaluated. As a proof of concept, only the intermediate concentration, namely 1.0 % w/w, was subjected to the electrical investigation.

The LSC devices were characterized under 1 sun AM1.5G irradiation. With this setup, a circular area having 5 mm diameter can be homogeneously illuminated. Both the cited solar simulation spectrum and the instrumental organization are discussed in the Experimental section, Paragraph 5.3.9. A pictorial schematization reproducing one of the considered LSC device, including the fundamental TIR pathway of the incoming photons, is provided in Figure 3.20.

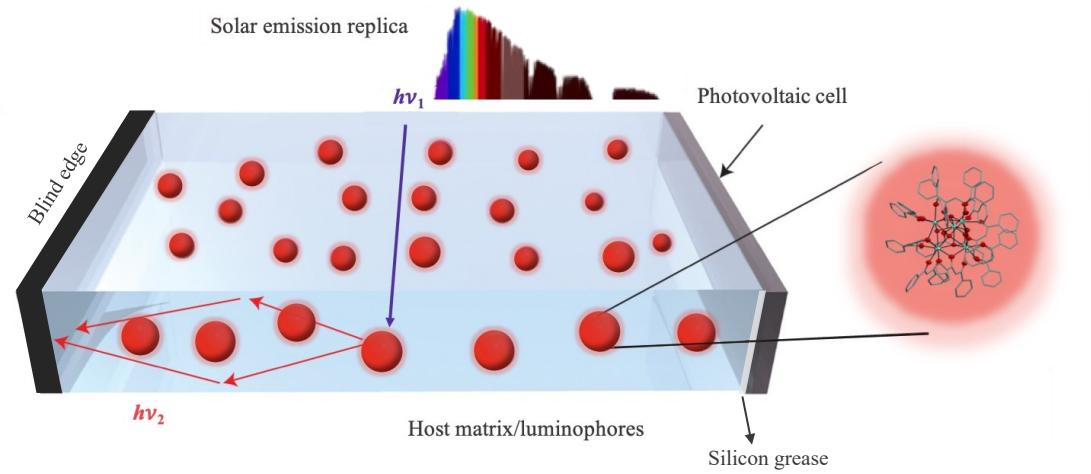

Figure 3.20. Illustration of the $[Eu_5]^1$ film optically coupled to a PV cell in the prospect of observing an enlargement slice of the doped micrometric material. The glass substrate was not drawn and only one of the three uncoupled edge is here covered, for the sake of visual clarity.

All the I-V curves were acquired with a Source Measure Unit (SMU). A special holder was employed for a monocrystalline silicon cell with nominal active area of 2.2 x 0.7 cm^2. The photovoltaic cell was cabled, vertically secured to the holder and protected up and down with a black polystyrene scaffold. The fixed and framed position of the cell allowed an easy sample positioning while assuring a reproducible measurement (Figure 3.21d, inset). Moreover, careful efforts have been devoted to shield the PV cell from direct illumination and to block the dissipation of the waveguided light from the concentrator's uncoupled sides using black tape. Ideally, perfectly reliable measurements can be only achieved if the PV modules accept photons exclusively from the allied emissive edge. Otherwise, if secondary light sources impinge on the silicon surface, a significative overestimation of the detected current could occur. Thus, artificial room light was switched off during the acquisition phase, so that to minimize this interference.

Additionally, silicon cells and LSCs were optically coupled using silicon grease spread on the edge of the functional material so to create an optical continuum in passing from the glass-adhered film to the PV surface. Such optical coupling condition assures a unilateral escalation of the materials' refraction indexes, ranging from 1.49 for PMMA to 3.98 for silicon. This phenomenon is used to prevent abrupt refractive coefficient's drops due to the presence of air (n = 1.00) between the LSC and the silicon solar cell that can be detrimental for the performance of the device.

Figure 3.21 displays the I-V and P-V diagrams for the 1.0 % w/w LSCs, each joined by the dotted ones of the reference glass tile. The short-circuit current (I_{SC}) values, derived from the intercept of the respective I-V curves, are also indicated.

All the three LSC generate a current of few hundreds of microamperes and, in particular, the device based on Eu^{gl} performs better than the other two (Figure 3.21).

A necked glass tile was used as reference to assess the contribution of the direct illumination of the solar simulator to the measured current values. The reference device, whose I-V and P-V profiles are reported with dotted lines in Figure 3.21, shows I_{SC} equal to 116.4 µA and a P_{max} of 14.5 µW. Europium-containing devices displayed higher values of I_{SC} and P_{max}. In particular, using Eu^{gl} as activator is possible to achieve I_{SC} = 363.7 µA and P_{max} = 72.2 µW (Figure 3.21, panel b).

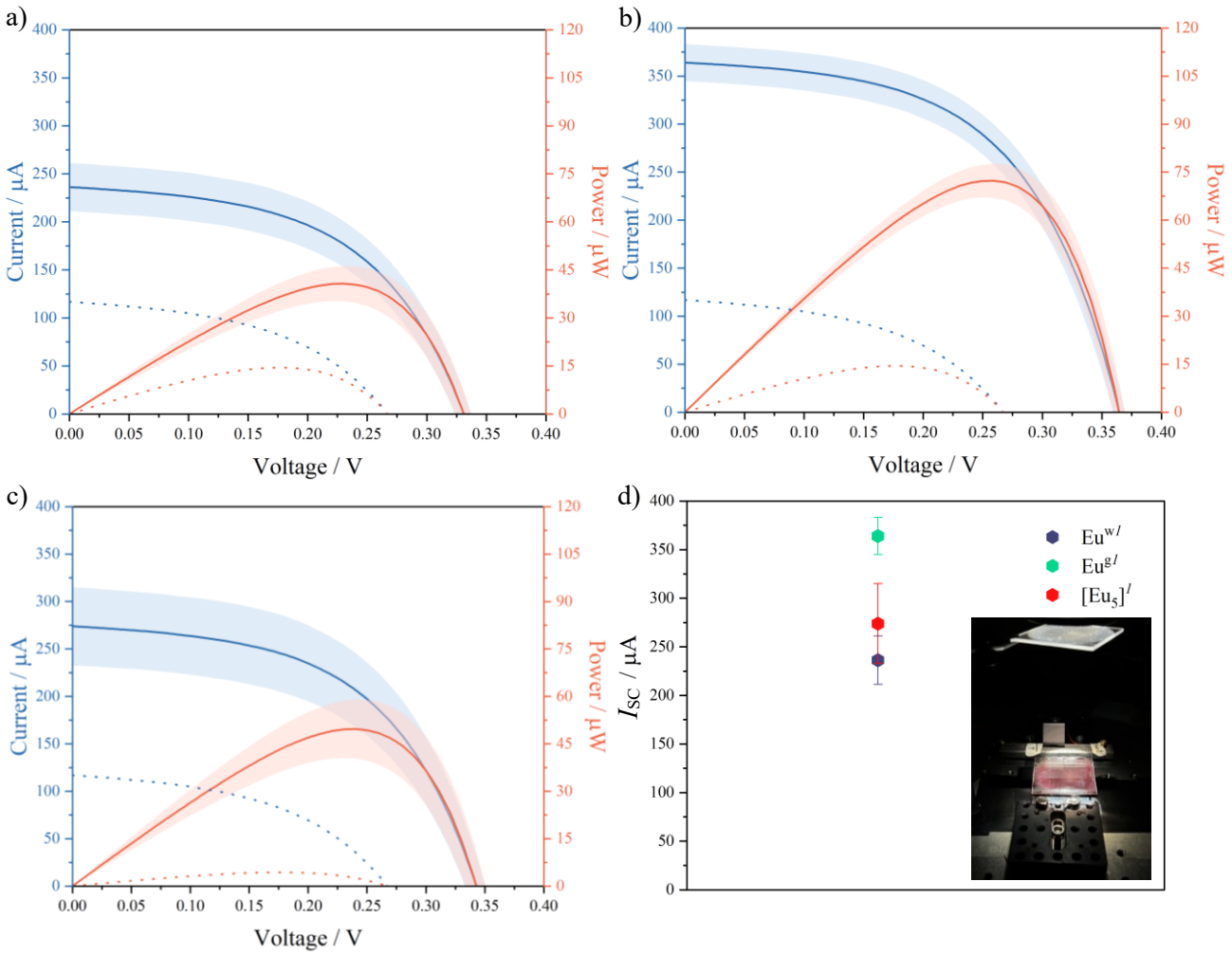

Figure 3.21. Mean curve (linear track) calculated on three repeated measurements and their standard deviation (shadowed area) for current and power performances of the LSCs made with Eu^{wl} (a), Eu^{gl} (b) and $[Eu_5]^l$ (c) glass-supported films. Dotted plots represent the blank response (the sole glass plate edge- and optically-coupled with the PV cell). d) Average value and their error bar of the short-circuit current at zero voltage detected for the three 1.0 % w/w samples.

Each experiment was replicated three times, and their mean values along with their standard deviation (shadowed area underneath the tracks) are collected in Figure 3.21. From the I-V and P-V plots just discussed, typical solar cell working metrics were extracted and resumed in Table 6, adhering to the terminology consolidated in LSC research[171] and to their evaluation protocol,[172] specifically for the PCE parameter.

The advantage of these smart materials lies in their potential use in urban contexts, where conventional photovoltaic panels cannot be installed without severely impacting the aesthetics of the urban landscape.

Table 6. Average values and standard deviations (only for the blank, absolute results are given) for working points and parameters relevant for standard solar cell characterization.

Sample	$J_{SC} \pm \sigma_J$ / mA·cm^2	$V_{OC} \pm \sigma_V$ / mV	$FF \pm \sigma_F$	$P_{max} \pm \sigma_P$ / mW	$PCE \pm \sigma_{PCE}$ / %
Glass	0.0047	267	0.46	0.0145	0.00232
Eu^{wl}	0.009 ± 0.001	331 ± 7	0.52 ± 0.00	0.041 ± 0.006	0.0065 ± 0.0009
Eu^{gl}	0.0146 ± 0.0008	364 ± 5	0.547 ± 0.006	0.072 ± 0.005	0.0116 ± 0.0008
[Eu$_5$]^l	0.011 ± 0.002	342 ± 9	0.527 ± 0.006	0.05 ± 0.01	0.008 ± 0.001

Alongside the electrical performance, the aesthetic of the materials for application in building integrated photovoltaic is an essential aspect. Provided the use of highly transparent PMMA matrix, it is the luminophore that decrees the aspect and optical quality of the entire collector. Since europium antenna complexes are classified as ultraviolet absorbers, they will not modify the intrinsic colour of the matrix in which they are embedded. Using PMMA, they allowed the preparation of transparent and colourless materials. To evaluate their aesthetic characteristics, quantitative parameters need to be considered, rather than relying solely on the subjective human eye perception.

In this context, the adopted figures of merit are the Average Visible Transmittance (AVT), Colour Rendering Index (CRI) and a* b* Colour Coordinates (CIELAB).[172, 173] These parameters were calculated from the transmittance spectra of the films.

AVT provides information on the transparency of the material, *i.e.* how much visible light can be actually transmitted by the LSC, while the CRI is a quantitative criterium of how accurately the colour of an object is preserved under certain illumination sources compared to standard conditions. Essentially, it represents a colour fidelity parameter.

Instead, CIELAB coordinates identify the colour of the material in a perceptually uniform space (a* gives the colour variation along the green-red axis and b* along the yellow-blue one).

The aesthetic parameters of the tested LSCs are reported in Table 7. The AVT, CRI, a* and b* values that a materials should possess for providing neutral colour applications, like the glass window are: CRI ≥ 85, CIELAB coordinates of -7 < a* < 0 and

-3 < b* < 7 and AVT > 88 %).[174] Indeed, 89-91 % values were found for the AVT metric, their colour rendering complies to the "excellent" CRI category embracing the 95-100 range, and the a* and b* coordinates refers to colour shades within the tolerable limits.

It was observed that at increasing loadings, particularly at 2.0 % w/w_{PMMA}, the samples exhibited a faint yellowish and vaguely perceivable colour, however fully tolerable by reference standards. At 0.5 and 1.0 % weight concentrations, the materials appeared completely achromatic, thus potentially able to seamlessly interchange glassy building elements.

Future studies should be dedicated to test all the remaining LSCs samples, giving that their aesthetical properties revealed promising for an advantageous deployment of them in ordinary architectural contexts.

Table 7. List of parameters distinguishing the aesthetical quality of an LSC device.

Sample	AVT / %	CRI	a*		b*	
Eu^{w05}	89.70	99.05	0.0000	- 1.11	0.0000	0.62
Eu^{w1}	90.79	97.94	0.0000	- 1.72	0.0000	1.83
Eu^{w2}	91.03	98.06	0.0000	- 2.88	0.0000	4.23
Eu^{g05}	90.90	99.12	0.0000	- 1.09	0.0000	0.45
Eu^{g1}	90.89	98.21	0.0000	- 1.60	0.0000	1.55
Eu^{g2}	90.68	98.20	0.0000	- 2.67	0.0000	3.77
$[Eu_5]^{05}$	90.27	98.98	0.0000	- 1.15	0.0000	0.71
$[Eu_5]^{1}$	90.82	98.52	0.0000	- 1.43	0.0000	1.25
$[Eu_5]^{2}$	90.76	98.41	0.0000	- 2.35	0.0000	3.18

CHAPTER IV

Conclusions and perspectives

This present work was aimed at bringing a contribution in two attractive fields of light-driven applications, particularly exploiting the intrinsic and widely considered photophysical properties of europium antenna systems.

Albeit the design and the photoluminescence characterization and applications of bis-*β*-diketonates of mononuclear Ln^{3+} complexes are widely studied, their oxocluster equivalent, as well as their dispersion into polymeric hosts, are a still relatively unexplored area. Therefore, within the frame of this thesis, particular attention has been paid to pursuing the synthesis of different variety of these extended structures, ending up in the easily-replicable formation of a pentanuclear europium-based oxocluster. Being protected by dibenzoylmethanide ligands, it presents five europium ions organized into a square pyramidal geometry, well adhering to the structural affinity of more contracted rare earths elements and to the earlier observed crystallographic motifs. Parallelly, two mononuclear complexes, namely $Eu(DBM)_3(H_2O)_2$ and $Eu(DBM)_3(DME)$, were prepared, the former being the direct one-metallic counterpart of the oxocluster and the latter a variety never reported in literature so far.

These synthesized red-luminescent molecules were characterized with ESI-MS spectrometry, ATR FT-IR, UV-Vis absorption and XPS spectroscopies. SC-XRD findings were attained exclusively for the exotic oxocluster, while the structures of the monometallic systems were deduced by the other characterization methods.

Through elaboration of existing procedures, the processability of the obtained compounds was expanded developing hybrid multifunctional polymeric-inorganic materials. Basically, they were entrapped in thin films of 5.0 x 5.0 cm^2 area and thickness of 200-250 μm, sticking on a glass platform and whose fabrication was refined within the scope of this thesis. Indeed, a controlled and gradual kinetic of solvent evaporation, roughly performed with an improved coverage setup, is a critical passage of the casting procedure in order to create homogeneous and high-quality films.

The polymeric matrix consisted of polymethylmethacrylate, which exhibited the desired transparency across the wavelengths relevant to the luminophores' absorption and emission spectra, thereby avoiding interference with their optical properties.

No detrimental effects have been noticed characterizing the doped PMMA films via luminescence spectroscopy, implicating that the fluorophores incorporation did not provoke substantial modifications concerning their photophysics. The emission spectra of europium complexes in solution and into the polymeric substratum are almost superimposed pointing out their successful incorporation into the selected matrix.

The supported films doped with europium complexes at different concentrations (0.5, 1.0 and 2.0 % by weight) were functionally tested as luminescent molecular thermometers and as LSCs.

Conserning luminescence thermometry, all the films performed well, having S_r higher than 1 % · K^{-1} for temperature values over 220 K. In particular, Eu^{w2} and $[Eu_5]^2$ showed the higher S_m value of 5.0 % · K^{-1} at 313 K.

Regarding LSC applications, the polymeric films doped with europium complexes displayed AVT, CRI and CIELAB chromaticity coordinates values close to those of the glass windows. In general, a clear double-paned insulated glass unit has AVT near 80 % and the one implemented in residential windows does not exceed 90 %, at best.[173] The AVT of the europium base-LSC is 91 %, and their CRI higher than 97 % approach that of the bare glass (100 %).

The outcomes for LMTs and LSCs did not differ significantly changing the emitter's nature, hence we cannot definitively favor one type over the other based on their performance. However, an environmental-friendly consideration can be made comparing the molar contents of europium involved. The Eu^w films utilized a lower amount of europium while still achieving similar thermometric and I-V responses. This could support a more efficient use of valuable material like a *f*-block element in the preparation of the functional devices.

CHAPTER V

Experimental details

5.1 Antenna compounds syntheses

All the reagents and the solvents used during the synthetic procedures and physical-chemical characterizations were purchased from commercial sources and used as received without further purification.

5.1.1. $[Eu_5(\mu_4\text{-}OH)(\mu_3\text{-}OH)_4(\mu\text{-}DBM)_4(DBM)_6]$ syntheses

The synthesis of the pentanuclear europium-dibenzoylmethane cluster, with the precise composition of $[Eu_5(\mu_4\text{-}OH)(\mu_3\text{-}OH)_4(\mu\text{-}DBM)_4(DBM)_6]$, has been accomplished adopting four different literature methods, as introduced at the beginning of Chapter III. Since only the last two illustrated synthetical approaches have succeeded with our laboratory's conditions, their products were subjected to characterizations and employed for the fabrication of heterogenic films. The literature receipts are here designated as method I, II, III and IV, following the mentioning order of the discussion in the Paragraph 3.1.1 and of the Figure 3.2 there included.

- Method I:

This synthesis has been realized following the procedure reported by Xiong and co-workers in 1999.[32]

In a 100 mL conical flask, hydrous europium chloride $EuCl_3 \cdot 6H_2O$ (122.6 mg, 0.33 mmol) and dibenzoylmethane (224.5 mg, 1.00 mmol) have been dissolved in 50 mL of ethanol with a stoichiometric amount of 1:3, giving a yellow solution. Next, *N*-methylmorpholine (0.67 mL, 6.09 mmol) has been added dropwise. After the system had been remained at room temperature and under magnetic stirring for 30 minutes, the solution has been filtered by gravity on a 6-µm-particle-retention paper disk, divided into four 25-mL bechers covered with pitted parafilm and left undisturbedly evaporating at room temperature for several days. The formation of cubic pale-yellow crystals occurred once the product has been recrystallized from toluene, qualitatively noticing

the peculiar europium red luminescent under 365 nm illumination. A white-yellow powder has precipitated together with the crystalline product.

- Method II:

The synthesis described by Petit *et al.* has been reproduced.[34] In an 8 mL vial, a 1:2 equivalent of $EuCl_3 \cdot 6H_2O$ (131.5 mg, 0.36 mmol) and dibenzoylmethane (136.6 mg, 0.61 mmol) has been solubilized in 5 mL of methanol. To this yellow solution, triethylamine (174 µL, 1.25 mmol) has been added, observing the immediate cloudiness and precipitation of a powder product by stirring the mixture at room temperature during 16 hours. A light-yellow powder has been isolated via centrifugation (6000 RPM for 3 minutes), however the washing step with a 1:1 quantity of methanol and hexane has led to its redispersion into the alcohol phase. After having been left under the fume hood for evaporation of the solvent and drying under dynamic vacuum, the precipitate has been subjected to different crystallization tests: neither slow diffusion of 1:1 CH_2Cl_2/C_xH_y stratifications (C_xH_y = *n*-hexane, toluene, cyclohexane, pentane, decane), nor slow evaporation and cooling of solution in dimethyl sulfoxide, dimethylformamide, methanol or chloroform gave crystalline materials.
The synthesis of the analogue species with 4,4,4-trifluoro-1-phenyl-1,3-butanedione ligand has been attempted, giving a visually brighter red luminescent product under ultraviolet rays' stimulation. Nevertheless, the adopted crystallization methods have produced only colourless and not luminescent needles, matching the structure of the $Et_3NH^+Cl^-$ side product, directly deriving from the combination of starting materials.

- Method III:

A combination of two literature procedures for pentanuclear lanthanide hydroxo-clusters has been unified for the [Eu_5] synthesis to define this third method.[18, 31] In a 50 mL one-neck round bottom flask, a yellow solution has been formed solubilizing $EuCl_3 \cdot 6H_2O$ (242.0 mg, 0.66 mmol) and dibenzoylmethane (262.6 mg, 1.17 mmol) in 8 mL of methanol. A separate solution of triethylamine (343 µL, mmol) in 2 mL of methanol has been added dropwise to the previous batch, turning its aspect into a more acid-yellow colour. Once left at ambient temperature and under magnetic stirring for 18 hours, the suspension has been evaporated, getting a yellow powder residue which has been dissolved into 15 mL of toluene and stirred for about one hour to selectively

solubilize the cluster. The product has been purified from the white salt $Et_3NH^+Cl^-$ by filtering the suspension on a paper disk of 6 μm particle retention. After six days some yellow crystals with dimensions suitable for SC-XRD analysis have formed on the vessel's walls.

- Method IV:

A recently refined synthetical route has been adopted for this last sample.[145] In a 50 mL one-neck round bottom flask, dibenzoylmethane (200.6 mg, 0.89 mmol) and potassium tert-butoxide (150.4 mg, 1.34 mmol) have been solubilized in 7.0 mL of methanol, forming a yellow solution. Keeping the system under magnetic stirring, a solution of $EuCl_3 \cdot 6H_2O$ (164.4 mg, 0.45 mmol) in 7.0 mL of methanol has been dropwisely added to the deprotonated ligand mixture (the Eu:HDBM:KO^{t}Bu ratio was 1:2:3), observing quite instantaneously the precipitation of a pallid yellow solid. The suspension stayed under magnetic stirring at room temperature for one day and subsequently evaporated to dryness. The residue has been isolated via redissolution in 7 mL of CH_2Cl_2 and filtration by gravity of the obtained yellow solution on a paper disk with 6 μm particle retention. Ultimately, the solvent has been evaporated from the filtered solution and a bright yellow solid has been yielded.
Noteworthy, the use of KO^{t}Bu as a deprotonating agent is preferable than the frequently adopted Et_3N in order to avoid the additional removal step due to the $Et_3NH^+Cl^-$ contamination. Yield: 177.2 mg (12.8 %). Elemental analysis: $C_{150}H_{115}O_{25}Eu_5$ (3077.347) calcd. C, 58.55 %; H, 3.77 %. Found: C, 58.61 %; H, 3.80 %.

5.1.2. $Eu(DBM)_3(H_2O)_2$ synthesis

The dibenzoylmethanide-based mononuclear Eu^{3+} complex has been prepared according to a previously reported literature method with little modifications.[148]
In a 100 mL conical flask, dibenzoylmethane (561.0 mg, 2.5 mmol) has been dissolved in 2.5 mL of ethanol and blended with 2.5 mL of a 1 M aqueous solution of NaOH. The resulting mixture has been subjected to magnetic stirring for approximately an hour and a half. Since a yellow suspension has been obtained, extra 2 mL of ethanol has been introduced to completely disperse the precipitate, heating at 40 °C for 15 minutes.

Afterwards, a solution of $EuCl_3 \cdot 6H_2O$ (458.3 mg, 1.25 mmol) in 2 mL of deionized water has been gradually introduced together with a further excess of this solvent (3 mL), noticing the instant formation of a yellow powder. After the mixture had been stirred overnight at room temperature, the precipitate has been isolated by filtration on a 6-µm-porosity paper disk, washed several times with deionized water and dried under vacuum over $CaCl_2$. Yield: 646.2 mg (60.2 %, based on $EuCl_3 \cdot 6H_2O$). Elemental analysis: $C_{45}H_{37}O_8Eu$ (857.7211) calcd. C, 63.01 %; H, 4.35 %. Found: C, 63.67 %; H, 4.31 %.

5.1.3. Eu(DBM)$_3$(DME) synthesis

In a 100 mL conical flask, the previously described Eu^w complex (149.5 mg, 0.17 mmol) has been mixed with dimethoxyethane, better known as *glyme*, (27 µL, 0.26 mmol) in 10 mL of CH_2Cl_2. The yellow solution has been refluxed for two hours at 45 °C, then evaporated to dryness. The resulting powder has been desiccated overnight under dynamic vacuum. Yield: 133.2 mg (83.8 % based on Eu^w). Elemental analysis: $C_{49}H_{43}O_8Eu$ (911.8125) calcd. C, 64.54 %; H, 4.75 %. Found: C, 64.59 %; H, 4.78 %.

5.1.4. [Tb$_9$Ti$_2$(µ$_4$-O)(µ$_3$-OH)$_{14}$(acac)$_{17}$(CH$_3$O)$_2$(CH$_3$OH)$_3$] synthesis

The titled oxocluster has been successfully obtained replicating a recent literature procedure.[110] A terbium(III) salt, namely $TbCl_3 \cdot 6H_2O$ (150.2 mg, 0.40 mmol), has been solubilized in 1.5 mL of methanol inside a 4 mL vial, at which resulting solution acetylacetone (Hacac, 102.5 µL, 1.00 mmol) has been merged. Sequential dropwise additions of $Ti(O^iPr)_4$ (12 µL, 0.04 mmol) and Et_3N (275 mL, 1.97 mmol) have turned the system initially bright yellow, then lighter. The obtained solution has remained at low temperature (2-4 °C) for a week, following the literature indication, then cooled at -18 °C for several weeks. After a month colourless block-shaped crystals started to appear and increased their size in a further couple of weeks. Their crystallographic structure has been confirmed through SC-XRD and manifested an intense green luminescence, perceived at naked eye when exposed under 365 nm radiation.

5.1.5. $[Eu_2Ti_4(\mu_2\text{-}O)_2(\mu_3\text{-}O)_4(bpy)_2(ba)_{10}]$ and $[Eu_2Ti_4(\mu_2\text{-}O)_2(\mu_3\text{-}O)_4(bpy)_2(fba)_{10}]$ syntheses

A solvothermal method has been adopted to prepare both these europium-oxo-titanium clusters,[144] initially consisting in combining the respective carboxylic acid with an europium(III) salt and 2,2'-bipyridine (bpy) in 5 mL of acetonitrile inside a 8 mL vial.
For $[Eu_2Ti_4]$, benzoic acid (Hba, 124.9 mg, 1.02 mmol), $Eu(OAc)_3{\cdot}xH_2O$ (17.1 mg, 0.05 mmol), bpy (16.0 mg, 0.10 mmol) have been used, whereas the reagents employed for $[Eu_2Ti_4]^f$ have been 2-fluorobenzoic acid (Hfba, 140.9 mg, 1.00 mmol), $Eu(OAc)_3{\cdot}xH_2O$ (16.7 mg, 0.05 mmol) and bpy (15.8 mg, 0.10 mmol).
To the resultant colourless solutions, $Ti(O^iPr)_4$ (36 µL, 0.12 mmol) has been introduced, suddenly generating a white precipitate. The milky suspensions have been put into an ultrasonic apparatus to better mix the reagents for 10 minutes, without attesting a solubility improvement, then heated to 80 °C for 36 hours. After that, the glass vials were cooled down to room temperature naturally. White plated crystals have been obtained for $[Eu_2Ti_4]$ and fair pink for $[Eu_2Ti_4]^f$, both revealing a strong red luminescence under a 365 nm radiation.

5.2 Film preparation procedure

The preparation of well-defined-shaped films either of pure PMMA and incorporating europium-based fluorophores has been accomplished through an earlier reported drop casting technique with slight modifications.[165]
Glass substrates, appositely cut with 25 cm^2 top area, were utilized as a reference platform above which the casting solutions have been dropped. Initially, they were washed with soap, rinsed with deionized water and immersed in a 6 M HCl bath, as described in literature.[175] After having been treated in the acidic solution for approximatively 15 hours, the plates were then removed and sequentially rinsed with deionized water, acetone and 2-propanol, insufflating air at the end of this latter cleavage in order to attain a dried and halo-free surface. Care has been taken in always exposing the upper face to all the washing and casting operations, the one that had been assuredly and completely covered by the acidic bath.

The treated slabs have been horizontally fixed with paper tape on Petri dishes and, in their turn, leveled on a laboratory counter. The dichloromethane solutions of luminophore and PMMA, whose quantities were clarified in previous discussion (see Chapter III, Paragraphs 3.2.1 and 3.2.2), have been stirred overnight to provide good homogeneity. A mild heating at 30-40 °C and a constant vigorous stirring were adopted to facilitate the dissolution process and to avoid polymer agglomerates on the solution's interface and vessel's walls.

Ultimately, the casting has been carried out ensuring that the solution would not spill off the slab's edges: to this aim, the pouring was meticulously stopped before reaching the glass' boundaries, thus leaving the liquid to spontaneously flow all over the surface. According to the last refined casting setup (see Paragraph 3.2.4), the samples were then covered with a large-diameter funnel with a cotton swab inside its entry in order to ensure a gradual solvent removal under ambient conditions.

The detachment of some films from the glass support was occasionally pursued via sonication.

5.3 Characterization techniques

5.3.1. Elemental Analysis

Carbon and hydrogen content determinations for Eu^{w}, Eu^{g} and $[Eu_5]$ compounds were performed by the internal CHNS analysis service at the Department of Chemical Science of University of Padova.

5.3.2. Single Crystal X-Ray Diffraction

The XRD data acquisition for structurally characterizing the obtained single crystals was carried out with an Oxford Diffraction Gemini E diffractometer, equipped with a 2K x 2K EOS CCD area detector, whose distance has been fixed at 45 mm, and sealed-tube Enhance (Mo) and (Cu) X-ray sources. Using N-paratone oil, an appropriately sized single crystal has been mounted on the top of a nylon loop sited at the head of a four-circle kappa goniometer. The acquisitions were run by means of the ω-scans technique using graphite-monochromatic radiation, Mo Kα or Cu Kα wavelength of, respectively, 0.71073 Å and 1.54056 Å and through the rotating crystal method. Diffractograms have

been collected in a 1024 x 1024 pixels mode, using 2 x 2 pixels binning. The diffraction intensities have been corrected for Lorentz/polarization effects as well as with respect to absorption. Empirical multi-scan absorption corrections using equivalent reflections have been performed with the scaling algorithm SCALE3 ABSPACK. The CryAlisPro program was employed for data collection, reduction, finalization and cell refinement. Accurate unit cell parameters were acquired by least squares refinement of the angular settings of strongest reflections, chosen from the whole experiment. The structures were solved by direct methods with Olex2 and by using ShelXT structure solution program by Intrinsic Phasing and refined with the ShelXL refinement package using least-squares minimization. In the last cycles of refinement, the ordered non-hydrogen atoms were refined anisotropically, whereas disordered partial occupancy non-hydrogen atoms were refined isotropically. Hydrogen atoms were included in calculated positions, and a riding model was used for their refinement.
Crystallographic data and structure refinements are summarized in Tables I-IV in the Appendix part.

5.3.3. ESI Mass Spectrometry

High resolution ESI-MS characterization was realized by analysing sample solutions at a concentration of the order of 10^{-4} M, either in THF, chloroform and toluene. The acquisitions were executed by Dott. Marco Roverso at the Department of Chemical Science of University of Padova.

5.3.4. Attenuated Total Reflectance FT-IR Spectroscopy

The vibrational characterization in the middle-infrared domain, MIR, (4000-650 cm^{-1}) was accomplished using Agilent Cary 630 FT-IR spectrometer, equipped with an interchangeable attenuated total reflectance accessory operating in the single-reflection mode.
A tip-of-spoon amount of the pure powders of the produced compound was deposited above the entire surface area of an IIa diamond ATR crystal as a 1 mm diameter interface between the sample and the infrared energy. A swivel press was lowered such

that its tip was in contact with the investigated solid and allowed the IR radiation emitted from the diamond window to interact with the compound.

The ATR spectra were recorded at room temperature, with a spectral resolution of 2 cm^{-1}, 8 scans and automatically corrected for the background response, which was represented by air. The acquisitions were computer-controlled using Agilent MicroLab PC software.

5.3.5. X-Ray Photoelectron Spectroscopy

X-ray photoelectron spectroscopy measurements were performed using a Thermo Scientific ESCALABQXi spectrometer with a monochromatic Al Kα X-ray source (1486.6 eV) operating at 200 W, a concentric hemispherical analyser and a spot size of 900 μm × 200 μm. The pressure in the analysis chamber was better than 10^{-7} mbar. A few milligrams of sample powder were attached to a sample holder, grounded to the instrument with double adhesive carbon tape. Charge compensation was applied by beams of combined low energy ion (Ar^+) and electron beams. No sample degradation was induced by the X-ray exposure. Survey scan was measured in a binding energy range of 0-1350 eV with a constant pass energy of 100 eV, at 1.0 eV/step, with a dwell time of 50 ms. High resolution spectra were recorded using a constant pass energy (25 eV), at 0.05 eV/step, with a dwell time of 50 ms. High-resolution XPS spectra were used for elemental state evaluation and quantification by means of the sensitivity factors provided by the manufacturer. Peak fitting was performed within the Avantage software after background correction using the smart-background function implemented in the same software and using pseudo-Voigt functions for synthetic peaks.

5.3.6. UV-Vis absorption, transmittance and reflection Spectroscopy

The electronic UV-Vis absorption spectra were acquired on a Cary 5000 UV-Vis-NIR spectrophotometer at 298 K and in a double-beam mode. The measurements were performed in the 250-800 nm wavelength range and with a spectral bandwidth of 2 nm. The luminophores solutions' spectra were recorded using quartz cells with 1 cm optical pathlength and subtracting the solvent contribution.

The absorption measurement of these solutions at different concentrations were essential to evaluate the molar extinction coefficients of the examined species, by applying the Lambert-Beer law and extrapolating the slope value from the respective linear fitting.

The effective absorptance ability of the doped luminescent films were indirectly evaluated measuring their scatter transmission and diffuse reflectance radiant flux's profiles. To this target, reflectance and transmittance spectra in the 250-800 nm interval were performed using the same instrument, though equipped with an internal diffuse reflectance accessory consisting of a poly(tetrafluoroethylene)-coated integration sphere.

Absorptance spectra have been derived as an energetic balance between the transmittance and reflectance contributions and its maximum ideal value of 100 %, for each wavelength number, following the formula $A_{\%}(\lambda) = 100 - T_{\%}(\lambda) - R_{\%}(\lambda)$. Ultimately, the materials' outputs were compared with the responses captured for an uncasted glass slate with the same thickness.

5.3.7. Room temperature Photoluminescence Spectroscopy

Room temperature photoluminescence spectra were executed with a Horiba Jobin-Yvon Fluorolog-3 spectrofluorimeter in a right-angle acquisition geometry both for the chloroform solutions and the processed films, with the latter facing the direction of the propagating incident beam. The instrument was equipped with double-grating monochromator in the excitation and emission sides coupled to a *R928P* Hamamatsu photomultiplier, a CCD detector and a continuous 450 W Xe arc lamp as the excitation source. The emission spectra were corrected for detection and optical spectral response of the spectrofluorimeter through a calibration curve supplied by the manufacturer. The excitation spectra were collected for the spectral distribution of the lamp intensity using a photodiode reference detector.

The luminescence lifetimes in the microsecond-millisecond time regime were measured with an experimental uncertainty of ± 10%, by means of a pulsed Xe lamp with variable repetition rate and elaborated with standard software fitting procedures. Three decay curves were collected on each sample, and reported lifetimes in the

Appendix section (Table V) are an average of at least two successful independent measurements.

5.3.8. Temperature dependent Photoluminescence analysis

Temperature dependent luminescence experiments (83-303 K) were carried out in backscattering geometry using a Horiba T64000 triple spectrometer equipped with a Peltier-cooled charge-coupled device detector (Horiba Synapse). An ultraviolet LED centered at 375 nm was used as excitation source, meticulously oriented in order to generate a rounded spot as exactly as possible at the center of the casted material. The spectrograph, equipped with 300 lines/mm gratings, was used as a single stage imaging monochromator.

The samples under investigation consisted on quadratic 1 cm^2 doped films, cut from the original fabricated ones and cautiously allocated in a round open chamber. Room artificial light has been switched off during the acquisition time and a black curtain has been set up around the sample's compartment to further guarantee that exclusively the LED beam hit their surfaces. The scattered radiation was collected through a 10x microscope objective (Olympus MPLAN, 10x/0.25).

Temperature dependent experiments were performed by means of a Linkam THMS600 heating/freezing microscope stage having temperature stability < 0.1°C over 83-873 K temperature range. Liquid nitrogen was used to gradually bring and temper the samples down to cryogenic temperatures.

Spectral elaboration was conducted with Horiba Labspec 6® software.

5.3.9. Electrical LSC characterization

Photovoltaic characterization occurred by evaluating the electrical responses of the device while light is incident upon the active region and comparing the outcomes with the activity of the sole silicon cell.

Current-voltage (I-V) curves of the LSC-PVs were collected using a custom-assembled setup under simulated solar irradiation (100 $mW \cdot cm^{-2}$, AM1.5G) and with a Keithley 2450 Graphical Source Measure Unit (SMU). Figure 6.1 illustrates the electrical

measurement apparatus' scheme equipped with a sample holder, appropriately constructed for aligning the LSC sample perpendicularly to the shaded PV cell, a voltage generator and an amperemeter, circuited with a photovoltaic module. Monocrystalline Si cells coupled to the LSCs were purchased from IXYS Corporation (series IXOLAR™ SolarBIT, model KXOB22-12X1F). During J-V measurements, LSCs and Si cells were optically coupled with optical grade silicone grease.

Figure 5.1. Schematics of the employed electronic circuit for measuring the performances of the developed LSCs films. The label *V* specifies the voltmeter, *A* the amperemeter and SMU designates the source meter unit.

Standard protocols for testing and comparing PV working cells require the use of a precise illumination at ambient temperature, as the so termed global horizontal AM1.5G solar irradiance. This spectral energy, defined as the power per unit area per wavelength (W/m^2nm in SI units) of the light source, is the most referenced solar spectrum replica that comprehensively account for the mutable amount of its energy incident on a certain spot on Earth's surface (see shadowed area in Figure 5.2). Indeed, it is unnegligible the consideration that the sunlight inconstancy is a function of latitude, local atmospheric conditions and daytime.

The acronym contains the AM abbreviation which denotes the air mass coefficient, namely the ratio of the direct optical path length penetrating the terrestrial atmosphere respect to the zenith optical path length. In another perspective, it demarcates the atmosphere thickness its radiation crosses from the sun's position to the earthly site. By definition, the total incoming solar power of this AM1.5G spectrum measures 1000 W/m^2, alternatively corresponding to "1 sun".

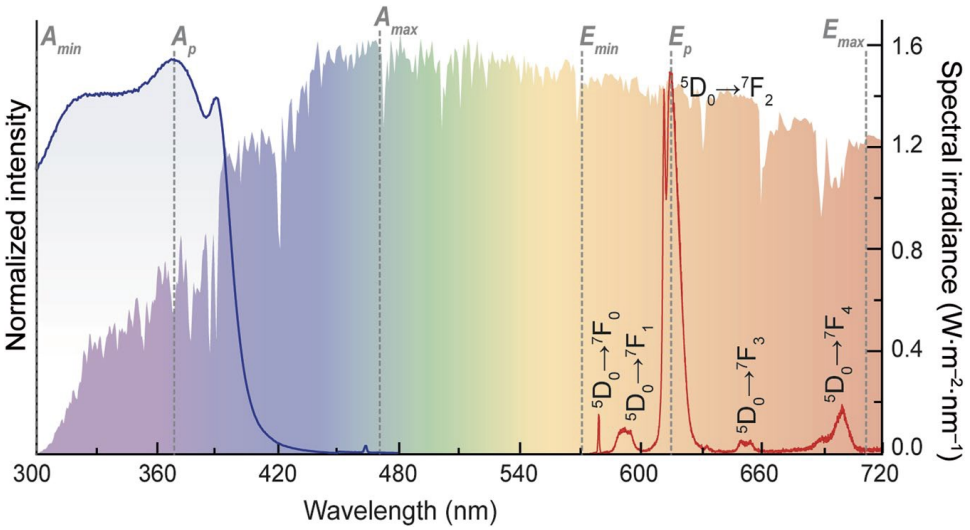

Figure 5.2. Example of the excitation (blue track) and emission (red track) spectra of a Eu^{3+}-based LSC, superimposed to the Air Mass 1.5 Global solar spectrum. A and E denotes excitation and emission, while the subscripts min, p and max represents the low-wavelength, peak intensity and high-wavelength values in the corresponding spectrum, respectively. Graphic reproduced from ref.[133]

An Xe arc lamp is traditionally engaged to mimic such solar radiation in PV testing, by the fact its optical emission well matches the above-cited benchmarked profile until 700 nm. Eventual spikes' line up can falsify the results from the moment the sun does not provide them, therefore, the NIR region ones are suppressed with apposite optical filters. The aesthetical optical figures of metric, namely AVT, CRI and colour coordinates CIELAB have been calculated using an input-output calculator developed by Yang *et al.*, freely attached to the related article and based on the upload of the transmittance and reflectance spectra.[172]

Additional Data and Figures

I. Chapter III, Paragraph 3.1.2: Crystallographic table and atomic labelling

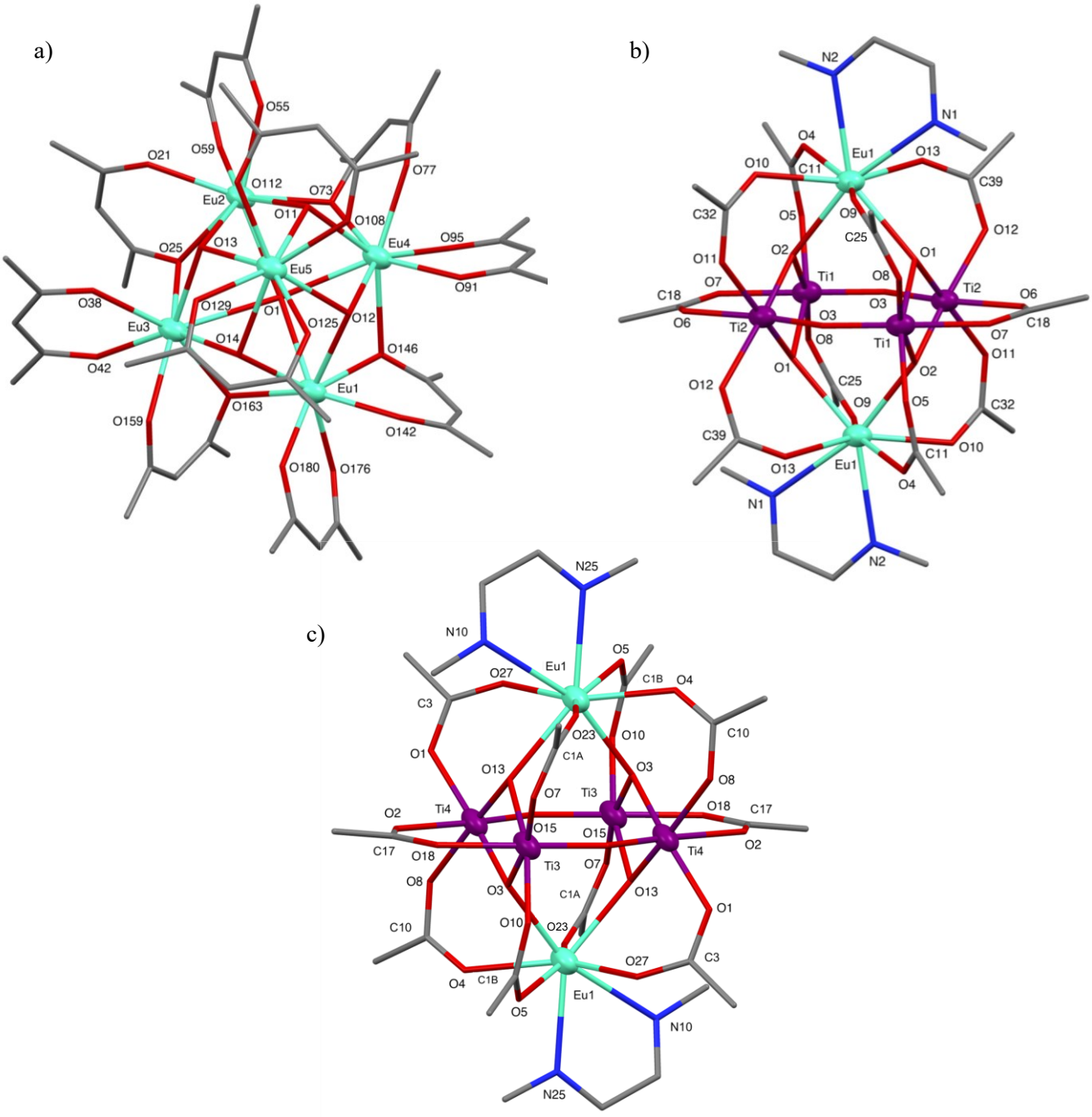

Figure I. Crystal structures of [Eu_5] (a), viewed from the top, [Eu_2Ti_4] (b) and [Eu_2Ti_4]^f (c) where hydrogens and aromatic rings were hidden for clarity reasons. Labels highlight the remaining atoms, following the nomenclature used in the successive II-IV Tables. Repeated numbers refer to symmetrically equivalent elements.

Table I. Crystal data and structure refinement details for [Eu_5], [Eu_2Ti_4] and [Eu_2Ti_4]^f.

	[Eu_5]	**[Eu_2Ti_4]**	**[Eu_2Ti_4]^f**
Empirical formula	$C_{150}H_{115}Eu_5O_{25}$	$C_{90}H_{64}Eu_2N_4O_{26}Ti_4$	$C_{90}H_{56}Eu_2F_{10}N_4O_{26}Ti_4$
Formula weight/ g·mol^{-1}	3077.3	2112.97	2294.90
Crystal dimensions/ mm^3	0.03 x 0.03 x 0.03	0.22 x 0.22 x 0.07	0.26 x 0.18 x 0.15
Crystal system	Monoclinic	Monoclinic	Triclinic
Space group	$P12_1/c1$	$P12_1/n1$	$P\bar{1}$
a, b, c/ Å	22.0525(7), 17.3193(7), 35.4127(2)	13.9453(3), 18.0677(2), 18.4614(3)	14.3255(3), 15.3467(4), 21.4722(2)
α, β, γ/ °	90.000, 101.051(2), 90.000	90, 111.648(2), 90	88.0474(14), 83.5966(14), 68.407(2)
Unit cell volume/ Å^3	13274.5(8)	4323.44(13)	4361.87(16)
Z	4	2	2
R/ %	5.69	7.67	10.7
ρ_{cal} / g cm^{-3}	1.540	1.623	1.747
No. of (independent) reflections	32579 (20307)	25097 (7096)	36896 (14154)
Temperature/ K	293	302.6(6)	303.3(4)
Absorption coefficient, μ/ mm^{-1}	2.399	13.893	13.999
F(000)	6120	2108	2272
Radiation type, λ/ Å	Mo Kα, 0.71073	Cu Kα, 1.54184	Cu Kα, 1.54184
θ_{min}, θ_{max}/ °	0.941, 24.093	3.552, 65.087	3.626, 65.089
Miller indexes range	$-25 \le h \le 25$; $-18 \le k \le 19$;$-40 \le \ell \le 40$	$-16 \le h \le 15$; $-21 \le k \le 21$; $-21 \le \ell \le 21$	$-16 \le h \le 16$;$-17 \le k \le 18$;$-21 \le \ell \le 25$
R_{int}	0.051	0.0498	0.0682
No. of observed data [$I > 2\sigma(I)$]	11062	5730	8847
N_{ref}, N_{par}, N_{rest}	10326, 1621, 0	7096, 503, 231	14154, 1255, 1346
R_1^{all}, $wR_2^{obs.(all)}$	0.1112, 0.0569 (0.0592)	0.0923, 0.2174 (0.2040)	0.1772, 03602 (0.2742)
GOF on F^2 (S)	1.0834	1.033	1.157
$\Delta\rho_{max}$, $\Delta\rho_{min}$/ e Å^{-3}	1.28, -1.49	1.954, -0.967	3.433, -5.273

Table II. Selected bond lengths and angles for [Eu_5].

Bond lengths/ *Å*							
(μ_4-OH)		Eu3–O25	2.451(8)	Eu2–O1–Eu4	89.6(2)	O1–Eu2–O25	69.0(3)
Eu1–O1	2.580(8)	Eu3–O163	2.381(9)	Eu2–O1–Eu3	86.1(2)	O1–Eu3–O25	65.0(3)
Eu2–O1	2.583(8)	Eu4–O73	2.425(8)	Eu1–O1–Eu3	86.0(2)	O1–Eu3–O163	63.1(3)
Eu3–O1	2.774(8)	Eu4–O146	2.508(8)	O1–Eu1–O12	67.6(3)	O1–Eu1–O163	64.9(3)
Eu4–O1	2.538(8)	(DBM)		O1–Eu1–O14	70.9(3)	O11–Eu5–O12	70.0(3)
(μ_3-OH)		Eu1–O142	2.364(9)	O1–Eu2–O11	68.4(3)	O12–Eu5–O14	69.9(3)
Eu1–O12	2.384(8)	Eu1–O176	2.337(8)	O1–Eu2–O13	69.5(3)	O14–Eu5–O13	69.7(3)
Eu1–O14	2.357(8)	Eu1–O180	2.304(8)	O1–Eu3–O13	66.9(3)	O13–Eu5–O11	68.6(3)
Eu2–O11	2.361(9)	Eu2–O21	2.382(9)	O1–Eu3–O14	67.6(2)	O176–Eu1–O180	73.8(3)
Eu2–O13	2.395(8)	Eu2–O55	2.294(8)	O1–Eu4–O11	68.7(3)	O142–Eu1–O146	72.9(3)
Eu3–O13	2.341(8)	Eu2–O59	2.365(8)	O1–Eu4–O12	69.0(3)	O55–Eu2–O59	74.2(3)
Eu3–O14	2.343(8)	Eu3–O38	2.340(9)	O11–Eu5–O12	70.0(3)	O21–Eu2–O25	72.2(3)
Eu4–O11	2.397(8)	Eu3–O42	2.318(10)	O12–Eu5–O14	69.9(3)	O38–Eu3–O42	72.0(3)
Eu4–O12	2.337(8)	Eu3–O159	2.401(9)	O13–Eu5–O14	69.7(3)	O159–Eu3–O163	72.2(3)
Eu5–O11	2.446(8)	Eu4–O77	2.348(8)	O11–Eu5–O13	68.6(3)	O91–Eu4–O95	73.4(3)
Eu5–O12	2.456(8)	Eu4–O91	2.323(9)	Eu1–O12–Eu4	100.1(3)	O73–Eu4–O77	73.3(3)
Eu5–O13	2.418(9)	Eu4–O95	2.325(8)	Eu1–O14–Eu3	102.0(3)	O125–Eu5–O129	72.4(3)
Eu5–O14	2.476(7)	Eu5–O108	2.378(8)	Eu2–O13–Eu3	101.2(3)	O108–Eu5–O112	73.2(3)
(μ-DBM)		Eu5–O112	2.343(9)	Eu2–O11–Eu4	98.7(3)		
Eu1–O146	2.410(8)	Eu5–O125	2.344(9)	O1–Eu1–O146	69.0(3)		
Eu1–O163	2.478(9)	Eu5–O129	2.397(8)	O1–Eu4–O146	68.2(3)		
Eu2–O25	2.391(8)	Bond angles/ °		O1–Eu4–O73	71.0(3)		
Eu2–O73	2.480(8)	Eu1–O1–Eu4	90.0(3)	O1–Eu2–O73	69.5(3)		

Table III. Selected bond lengths and angles for [Eu_2Ti_4].

Bond lengths/ *Å*					
Eu1–N1	2.64(1)	C18–O7	1.26(1)	O7–C18–O6	125(1)
Eu1–N2	2.569(9)	C25–O8	1.26(1)	O13–C39–O12	124(1)
Eu1–O1	2.366(5)	C25–O9	1.25(1)	Ti1–O5–C11	133.7(6)
Eu1–O2	2.346(6)	C32–O10	1.25(1)	Ti1–O7–C18	125.3(7)
Eu1–O4	2.401(7)	C32–O11	1.28(1)	Ti1–O8–C25	128.4(7)
Eu1–O9	2.398(8)	C39–O12	1.25(1)	Ti2–O6–C18	125.4(7)
Eu1–O10	2.393(7)	C39–O13	1.26(1)	Ti2–O11–C32	132.8(6)
Eu1–O13	2.376(7)	Bond angles/ °		Ti2–O12–C39	129.7(7)
Ti1–O1	1.917(5)	N1–Eu1–N2	61.7(3)	Ti1–O1–Ti2	96.9(3)
Ti1–O2	1.879(6)	O1–Eu1–O2	80.6(2)	Ti1–O2–Ti2	99.4(3)
Ti1–O3	1.812(7)	O1–Eu1–O9	76.8(2)	Ti1–O3–Ti2	143.3(4)
Ti1–O5	2.018(6)	O1–Eu1–O13	76.0(2)	O1–Ti1–O8	94.0(3)
Ti1–O7	2.111(8)	O2–Eu1–O9	106.0(2)	O1–Ti2–O12	92.8(2)
Ti1–O8	2.040(7)	O2–Eu1–O10	71.2(2)	O2–Ti1–O5	89.6(3)
Ti2–O1	1.912(6)	O4–Eu1–O10	83.1(3)	O2–Ti2–O11	91.9(2)
Ti2–O2	1.879(5)	O4–Eu1–O13	72.1(2)		
Ti2–O3	1.816(8)	Eu1–O4–C11	136.4(6)		
Ti2–O6	2.099(8)	Eu1–O9–C25	143.8(7)		
Ti2–O11	2.040(6)	Eu1–O10–C32	132.1(7)		
Ti2–O12	2.049(5)	Eu1–O13–C39	142.8(7)		
C11–O4	1.25(1)	O4–C11–O5	124.3(9)		
C11–O5	1.27(1)	O8–C25–O9	125(1)		
C18–O6	1.26(1)	O10–C32–O11	126(1)		

Table IV. Selected bond lengths and angles for $[Eu_2Ti_4]^f$.

Bond lengths/ *Å*					
Eu1–N10	2.68(2)	C1B–O10	1.28(2)	O18–C17–O2	124(2)
Eu1–N25	2.53(2)	C3–O1	1.25(2)	O23–C1A–O7	127(2)
Eu1–O3	2.37(1)	C3–O27	1.31(2)	Ti3–O7–C1A	127(1)
Eu1–O4	2.42(2)	C10–O4	1.23(3)	Ti3–O18–C17	125(1)
Eu1–O5	2.44(1)	C10–O8	1.27(3)	Ti3–O10–C1B	134(1)
Eu1–O13	2.38(1)	C17–O2	1.22(3)	Ti4–O1–C3	127(1)
Eu1–O23	2.39(2)	C17–O18	1.30(2)	Ti4–O2–C17	127(1)
Eu1–O27	2.28(1)	Bond angles/ °		Ti4–O8–C10	136(1)
Ti3–O3	1.83(1)	N10–Eu1–N25	61.5(6)	Ti3–O15–Ti4	143.8(8)
Ti3–O7	2.05(1)	O3–Eu1–O4	72.6(5)	Ti3–O3–Ti4	100.3(6)
Ti3–O10	2.02(1)	O3–Eu1–O5	70.9(4)	Ti3–O13–Ti4	97.5(5)
Ti3–O13	1.91(1)	O3–Eu1–O23	107.6(5)	O1–Ti4–O13	93.2(5)
Ti3–O15	1.82(2)	O4–Eu1–O5	82.1(5)	O3–Ti4–O8	90.9(5)
Ti3–O18	2.12(2)	O5–Eu1–O27	72.0(4)	O7–Ti3–O13	95.1(5)
Ti4–O1	2.03(1)	O13–Eu1–O23	76.4(5)	O3–Ti3–O10	89.2(5)
Ti4–O2	2.14(2)	O27–Eu1–O13	72.2(4)		
Ti4–O3	1.91(1)	Eu1–O4–C10	137(1)		
Ti4–O8	2.05(1)	Eu1–O5–C1B	130(1)		
Ti4–O13	1.91(1)	Eu1–O23–C1A	144(1)		
Ti4–O15	1.80(2)	Eu1–O27–C3	145(1)		
C1A–O7	1.25(2)	O1–C3–O27	124(2)		
C1A–O23	1.22(2)	O4–C10–O8	123(2)		
C1B–O5	1.28(3)	O5–C1B–O10	126(2)		

II. Chapter III, Paragraph 3.1.6: UV-Visible absorption spectra

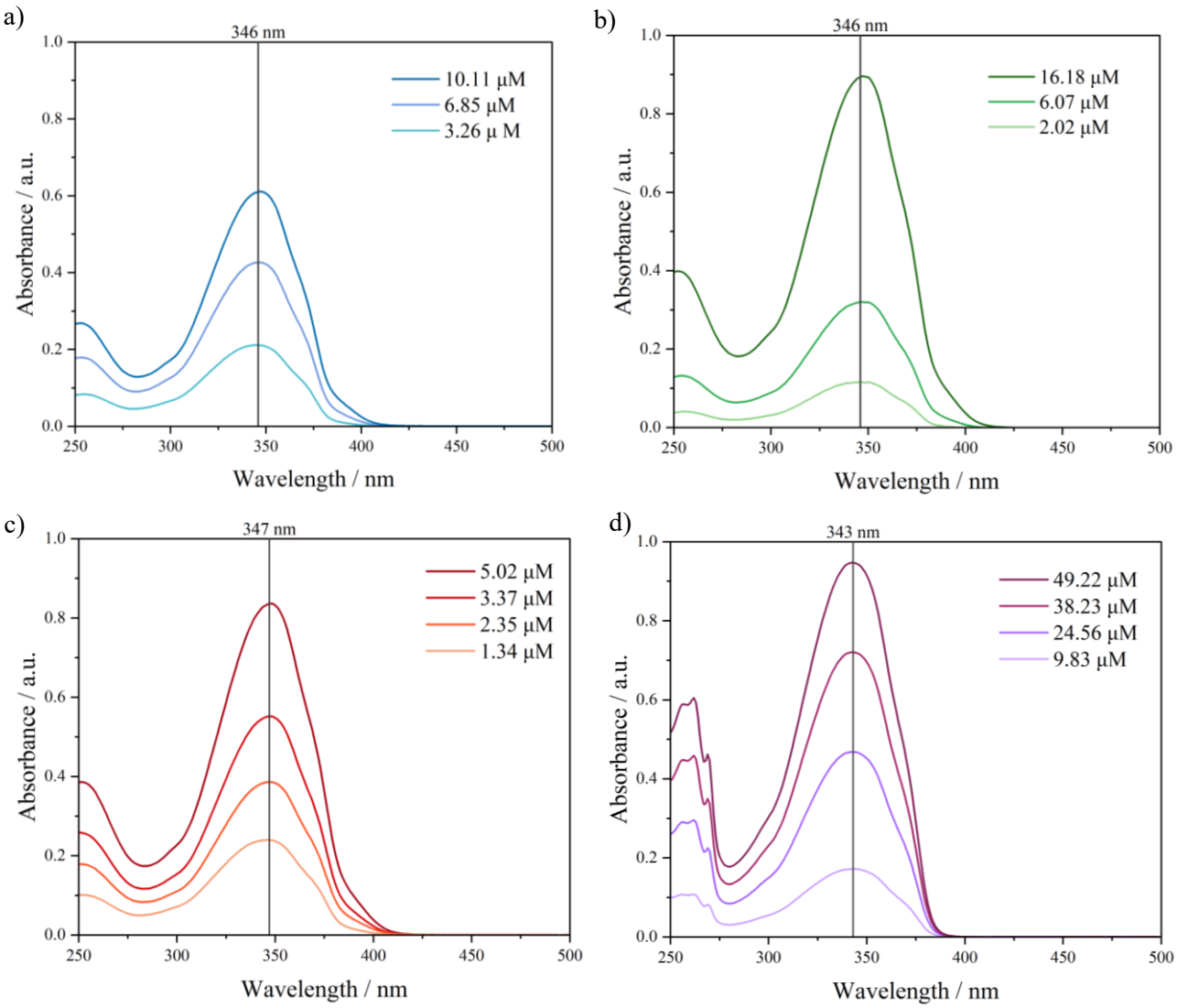

Figure II. Absorption spectra of a) $[Eu]_5$, b) Eu^w, c) Eu^g and d) HDBM at different concentrations, used to evaluate the molar extinction coefficients.

III. Chapter III, Paragraph 3.3.1: Room-temperature photophysical measurements

Table V. Luminescence lifetimes, τ, collected from the $^5D_0$ decay curves for all the casted films.

Sample	τ / µs	*Sample*	τ / µs	*Sample*	τ / µs
Eu^{w05}	221	Eu^{g05}	231	$[Eu_5]^{05}$	193
Eu^{w1}	183	Eu^{g1}	199	$[Eu_5]^{1}$	215
Eu^{w2}	182	Eu^{g2}	185	$[Eu_5]^{2}$	199

IV. Chapter III, Paragraph 3.3.2: Thermometric analysis

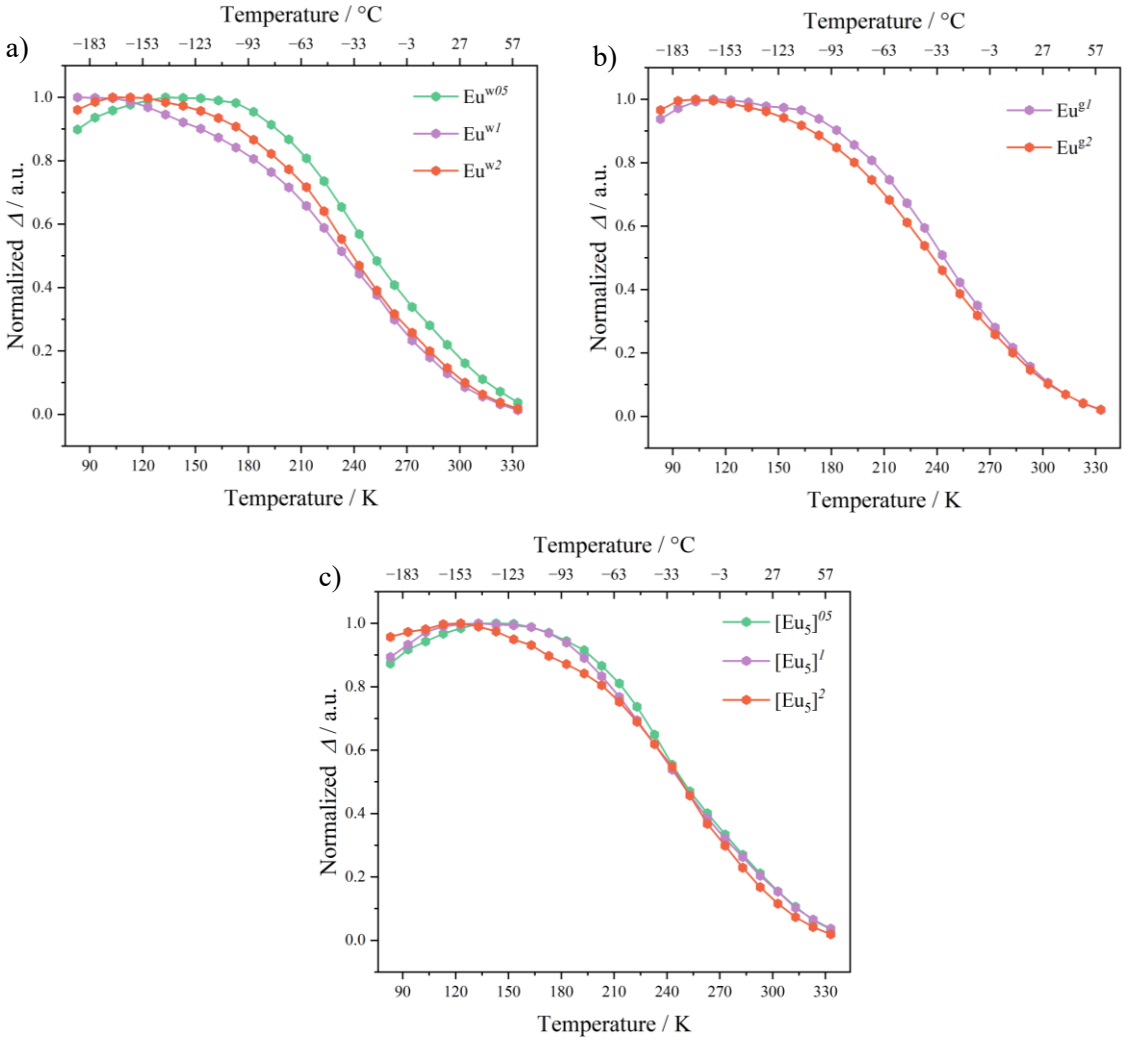

Figure VI. Thermometric parameter, *Δ*, *versus* temperature plots, normalized for the maximum intensity of luminescence.

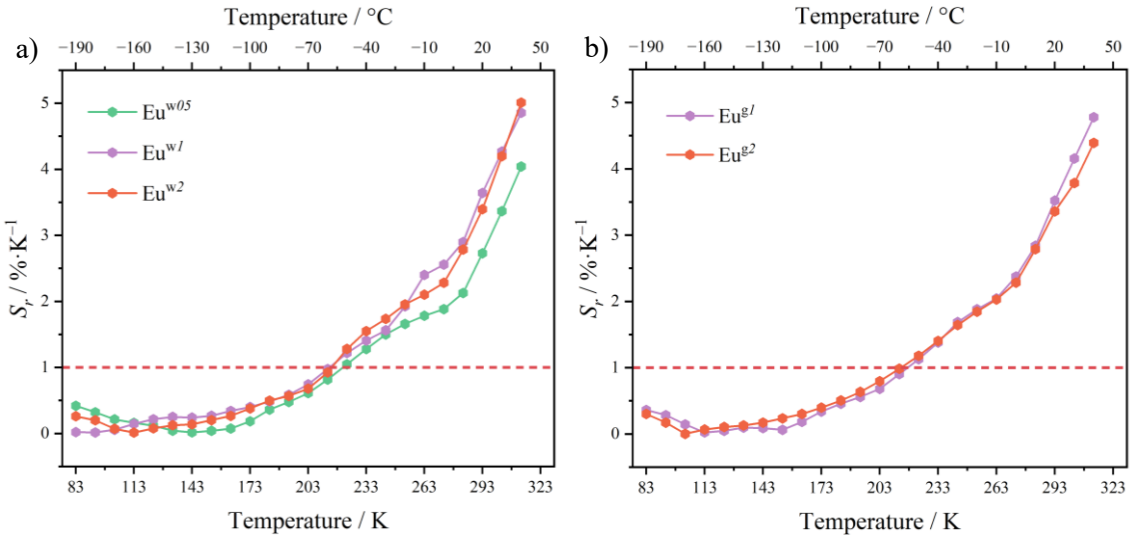

Figure VII. Variable temperature emission spectra of a) Eu^{w} and b) Eu^{g} (λ_{ex} = nm) changing the weight content.

V. Chapter III, Paragraph 3.3.3: Solar cell parameters

Photovoltaic devices are universally characterized and compared using specific working metrics, e.g. the short-circuit current (I_{SC}), the open-circuit voltage (V_{OC}) and the fill factor (*FF*), determined from their current-voltage (I-V) characteristic curve. The typical shape of the I-V chart of an illuminated solar cell is illustrated in Figure VIII, along with its derived power-voltage (P-V) characteristic curvature, where the electrical power is obtained as the product between voltage and current.

The overall current that can be extracted from a solar cell derive from the superposition of the normal dark currents in the diode and the light-generated one.[176]

Under the validity of the Ohm's law $\left(R_L = \frac{V}{I}\text{, where } R_L \text{ is a load resistance}\right)$, the working points of I_{SC} and V_{OC} can be identified when R_L is zero or infinitely high, respectively, and there is no electrical power delivered.[177]

The I-V plot's intercept with the vertical axis corresponds to the I_{SC} value, which is the largest current that a solar cell can emit under short-circuited, namely zero-voltage, operating modality and relates with the generation and collection of light-produced carriers. If dissipative mechanisms are restrained, an ideal PV cell furnishes an I_{SC} equal to the current produced thanks to sunlight interaction.[176]

When the net current is measured null, it is possible to establish the V_{OC} value which is the maximum voltage available from a solar cell and indicates the amount of electron-hole recombination events which are at play.

The power-voltage correlation curve reaches a maximum point, P_{max}, where the PV module should operate to supply the greatest power output, occurring parallelly at the V_{max} and I_{max} values. The utmost power of a solar cell is conventionally computed from the FF parameter, specified as the ratio between the P_{max}, which can be also express by the V_{max} x I_{max} product, and the V_{OC} x I_{SC} multiplication.

$$FF = \frac{P_{max}}{V_{OC} \text{ x } I_{SC}} = \frac{A_1}{A_2} \qquad \textit{Eq. A.1}$$

As intuitive from Figure VIII, the filling factor reveals the graphical *squareness* of the characteristic I-V diagram and represents the area of the light-blue rectangle (A_2) fitting those such very curve;[176] the highest this factor the best the overall performance of the PV system.

Another relevant electrical metric is the performance of the solar cell connected with an LSC device in terms of the fraction of incoming power that it is effectively transformed into electricity by the cell. It can be defined according to the power conversion efficiencies (*PCE*) relative to the PV-coupled edges, and represented by the ratio of the peak power extracted from the cell to the incident light power (P_{in}).

$$PCE = \frac{P_{max}}{P_{in}} \qquad \textit{Eq. A.2}$$

By normalizing the output power for the area of the PV cell (P_{in} is generally reported as an irradiance, in $W \cdot m^{-2}$) and replacing the equation *A.1* in *A.2*, the experimental expression (*Eq. A.3*) for the *PCE* utilized for the data presented in Chapter 3.3.3 is so obtained.

$$PCE = \frac{J_{LSC} \text{ x } V_{OC} \text{ x } FF}{P_{in}} \qquad \textit{Eq. A.3}$$

It is remarkable that PV technologies are conceived as a broad family of devices, including either classical single solar cells and the ones combined with luminescent

concentrators. Therefore, the just elucidated parameters can actually be applied to these innovative LSC systems in order to estimate their advantages over traditional PV units.

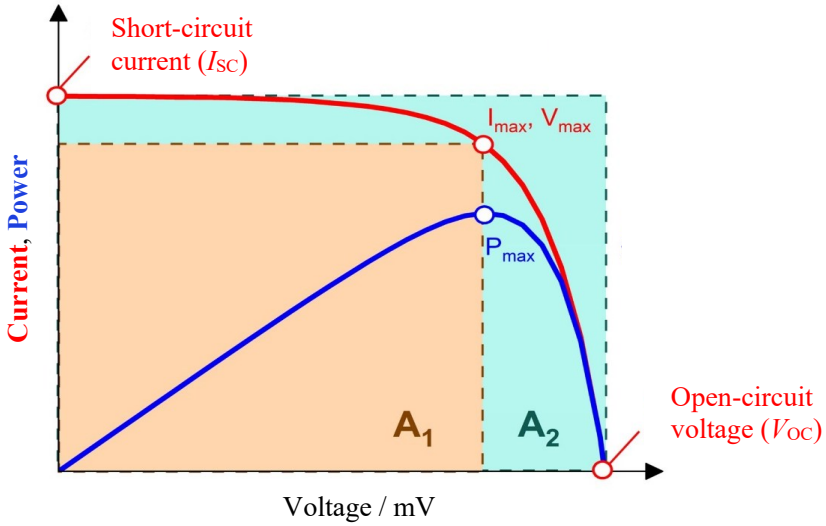

Figure VIII. Exemplificative scheme of the cell output current (red line) and power (blue line) as a function of voltage, showing the main parameters defining the PV device operation.

References

[1] Armelao, L.; Quinci, S.; Barigelletti, F.; Accorsi, G.; Bottaro, G.; Cavazzini, M.; Tondello, E. Design of luminescent lanthanide complexes: from molecules to highly efficient photo-emitting materials. *Coord. Chem. Rev.* **2010**, *254*, 487–505.

[2] Binnemans, K. Lanthanide-based luminescent hybrid materials. *Chem. Rev.* **2009**, *109*, 4283–4374.

[3] Wagner, A. T.; Roesky, P. W. Rare-earth metal oxo/hydroxo clusters – synthesis, structures, and applications. *Eur. J. Inorg. Chem.* **2016**, *2016*, 782–791.

[4] Zheng, Z. Cluster compounds of rare-earth elements. In *Handbook of physics and chemistry of rare earths*; Gschneidner Jr., K. A.; Bünzli, J-C. G.; Pecharsky, V. K., Ed.; Elsevier, Vol. 40, 2010; pp. 109–239.

[5] Zhang, Z.; Zhang, Y.; Zheng, Z. Lanthanide hydroxide cluster complexes via ligand-controlled hydrolysis of the lanthanide ions. In *Recent development in clusters of rare earths and actinides: chemistry and materials. Structure and bonding*; Zheng, Z., Ed.; Springer, Berlin, Heidelberg, Vol. 173, 2016; pp. 1–49.

[6] a) Gálico, D. A.; Kitos, A. A.; Ovens, J. S.; Sigoli, F. A.; Murugesu, M. Lanthanide-based molecular cluster-aggregates: optical barcoding and white-light emission with nanosized $\{Ln_{20}\}$ compounds. *Angew. Chem. Int. Ed.* **2021**, *60*, 6130–6136. b) Virender; Chauhan, A.; Kumar, A.; Singh, G.; Solovev, A. A.; Xiong, J.; Liu, X.; Mohan, B. Photonic properties and applications of multi-functional organo-lanthanide complexes: recent advances. *J. Rare Earths.* **2024**, *42*, 16–27.

[7] a) Gálico, D. A.; Murugesu, M. Inside-out/outside-in tunability in nanosized lanthanide-based molecular cluster-aggregates: modulating the luminescence thermometry performance via composition control. *ACS Appl. Mater. Interfaces*. **2021**, *13*, 47052–47060. b) Gálico, D. A.; Murugesu, M. Boosting the sensitivity with time-gated luminescence thermometry using a nanosized molecular cluster aggregate. *Nanoscale.* **2023**, *15*, 5778–5785.

[8] a) Thielemann, D. T.; Wagner, A. T.; Rösch, E.; Kölmel, D. K.; Heck, J. G.; Rudat, B.; Neumaier, M.; Feldmann, C.; Schepers, U.; Bräse, S.; Roesky, P. W. Luminescent cell-penetrating pentadecanuclear lanthanide clusters. *J. Am. Chem. Soc.* **2013**, *135*, 7454–7457. b) De, A.; Bala, S.; Saha, S.; Das, K. S.; Akhtar, S.; Adhikary, A.; Ghosh, A.; Huang, G-Z.; Chowdhuri, S. P.; Das, B. B.; Tong, M-L.; Mondal, R. Lanthanide clusters of phenanthroline containing a pyridine-pyrazole based ligand: magnetism and cell imaging. *Dalton Trans.* **2021**, *50*, 3593–3609.

[9] a) Zheng, X-Y.; Kong, X-J.; Zheng, Z.; Long, L-S.; Zheng, L-S. High-nuclearity lanthanide-containing clusters as potential molecular magnetic coolers. *Acc. Chem. Res.* **2018**, *51*, 517–525. b) Bala, S.; Bishwas, M. S.; Pramanik, B.; Khanra, S.; Fromm, K. M.; Poddar, P.; Mondal, R. Construction of polynuclear lanthanide (Ln = Dy^{III}, Tb^{III}, and Nd^{III}) cage complexes using pyridine-pyrazole-based ligands: versatile molecular topologies and SMM behavior. *Inorg. Chem.* **2015**, *54*, 8197–8206.

[10] Huang, W.; Liu, Q.; Chen, W.; Feng, M.; Zheng, Z. Recent advances in the catalytic applications of lanthanide-oxo clusters. *Magnetochemistry.* **2021**, *7*, 161.

[11] a) Zheng, X-Y.; Xie, J.; Kong, X-J.; Long, L-S.; Zheng, L-S. Recent advances in the assembly of high-nuclearity lanthanide clusters. *Coord. Chem. Rev*. **2019**, *378*, 222–236. b) Zheng, X-Y.; Jiang, Y-H.; Zhuang, G-L.; Liu, D-P.; Liao, H-G.; Kong, X-J.; Long, L-S.; Zheng, L-S. A gigantic molecular wheel of {Gd_{140}}: a new member of the molecular wheel family. *J. Am. Chem. Soc*. **2017**, *139*, 18178–18181.

[12] Gálico, D. A.; Calado, C. M. S.; Murugesu, M. Lanthanide molecular cluster-aggregates as the next generation of optical materials. *Chem. Sci*. **2023**, *14*, 5827–5841.

[13] Zheng, Z. Ligand-controlled self-assembly of polynuclear lanthanide-oxo/hydroxo complexes: from synthetic serendipity to rational supramolecular design. *Chem. Commun.* **2001**, 2521–2529.

[14] Andrews, P. C.; Gee, W. J.; Junk, P. C.; Massi, M. Variation of structural motifs in lanthanoid hydroxo clusters by ligand modification. *New J. Chem*. **2013**, *37*, 35–48.

[15] Kong, X-J.; Wu, Y.; Long, L-S.; Zheng, L-S.; Zheng, Z. A chiral 60-metal sodalite cage featuring 24 vertex-sharing [$Eu_4(\mu_3\text{-}OH)_4$] cubanes. *J. Am. Chem. Soc*. **2009**, *131*, 6918–6919.

[16] Li, X-L.; He, L-F.; Feng, X-L.; Song, Y.; Hu, M.; Han, L-F.; Zheng, X-J.; Zhang, Z-H.; Fang, S-M. Two chiral tetradecanuclear hydroxo-lanthanide clusters with luminescent and magnetic properties. *CrystEngComm.* **2011**, *13*, 3643–3645.

[17] Li, X-L.; Li, F-C.; Zhang, X-L.; Liu, Y-F.; Wang, A-L.; Tian, J-F.; Xiao, H-P. Synthesis, crystal structures and magnetic properties of two tetranuclear lanthanide-hydroxo cubane clusters. *Synth. Met.* **2015**, *209*, 220–224.

[18] Baskar, V.; Roesky, P. W. Synthesis and structural characterization of a series of tetranuclear lanthanide clusters. *Z. Anorg. Allg. Chem.* **2005**, *631*, 2782–2785.

[19] Datta, S.; Baskar, V.; Li, H.; Roesky, P. W. Synthesis and structural characterization of tetra- and pentanuclear lanthanide hydroxide clusters. *Eur. J. Inorg. Chem.* **2007**, *2007*, 4216–4220.

[20] Andrews, P. C.; Beck, T.; Fraser, B. H.; Junk, P. C.; Massi, M.; Moubaraki, B.; Murray, K. S.; Silberstein, M. Functionalised *β*-diketonate polynuclear lanthanoid hydroxo clusters: synthesis, characterization, and magnetic properties. *Polyhedron.* **2009**, *28*, 2123–2130.

[21] Chen, X-Y.; Yang, X.; Holliday, B. J. Metal-controlled assembly of near-infrared-emitting pentanuclear lanthanide *β*-diketone clusters. *Inorg. Chem.* **2010**, *49*, 2583–2585.

[22] Gamer, M. T.; Lan, Y.; Roesky, P.W.; Powell, A. K.; Clérac, R. Pentanuclear dysprosium hydroxy cluster showing single-molecule-magnet behavior. *Inorg. Chem.* **2008**, *47*, 6581–6583.

[23] King, T. L.; Palomero, O. E.; Bard, A. B.; Espinoza Jr., J. A.; Guo, H.; Schipper, D.; Yang, X.; Depue, L. J.; Que, E. L.; Jones, R. A. Visible luminescent Ln_{42} nanotorus coordination clusters. *J. Coord. Chem.* **2021**, *74*, 92–101.

[24] Dubé, T.; Conoci, S.; Gambarotta, S.; Yap, G. P. A. Divalent and mixed-valence samarium clusters supported by dipyrrolide ligand. *Organometallics.* **2000**, *19*, 1182–1185.

[25] Alexandropoulos, D. I.; Mukherjee, S.; Papatriantafyllopoulou, C.; Raptopoulou, C. P.; Psycharis, V.; Bekiari, V.; Christou, G.; Stamatatos, T. C. A new family of nonanuclear lanthanide clusters displaying magnetic and optical properties. *Inorg. Chem.* **2011**, *50*, 11276–11278.

[26] Wang, R.; Song, D.; Wang, S. Toward constructing nanoscale hydroxo-lanthanide clusters: syntheses and characterizations of novel tetradecanuclear hydroxo-lanthanide clusters. *Chem. Commun.* **2002**, 368–369.

[27] Wang, R.; Zheng, Z.; Jin, T.; Staples, R. J. Coordination chemistry of lanthanides at "high" pH: synthesis and structure of the pentadecanuclear complex of europium(III) with tyrosine. *Angew. Chem. Int. Ed.* **1999**, *38*, 1813–1815.

[28] Kong, X-J.; Long, L-S.; Zheng, L-S.; Wang, R.; Zheng, Z. Hydrolytic synthesis and structural characterization of lanthanide hydroxide clusters supported by nicotinic acid. *Inorg. Chem*. **2009**, *48*, 3268–3273.

[29] Wu, Y.; Morton, S.; Kong, X.; Nichol, G. S.; Zheng, Z. Hydrolytic synthesis and structural characterization of lanthanide-acetylacetonato/hydroxo cluster complexes – A systematic study. *Dalton Trans.* **2011**, *40*, 1041–1046.

[30] Aromí, G.; Gamez, P.; Reedijk, J. Poly beta-diketones: prime ligands to generate supramolecular metalloclusters. *Coord. Chem. Rev*. **2008**, *252*, 964–989.

[31] Roesky, P. W.; Canseco-Melchor, G.; Zulys, A. A pentanuclear yttrium hydroxo cluster as an oxidation catalyst. Catalytic oxidation of aldehydes in the presence of air. *Chem. Commun.* **2004**, 738–739.

[32] Xiong, R-G.; Zuo, J-L.; Yu, Z.; You, X-Z.; Chen, W. $Eu_5(\mu_4\text{-}OH)(\mu_3\text{-}OH)_4(\mu\text{-}DBM)_4(DBM)_6$ (DBM = dibenzoylmethide): a novel Eu_5 square-pyramid polynuclear complex with a rare μ_4-OH bridging mode. *Inorg. Chem. Commun.* **1999**, *2*, 490–494.

[33] Hauser, C. P.; Thielemann, D. T.; Adlung, M.; Wickleder, C.; Roesky, P. W.; Weiss, C. K. Luminescent polymeric dispersions and films based on oligonuclear lanthanide clusters. *Macromol. Chem. Phys.* **2011**, *212*, 286–296.

[34] Petit, S.; Baril-Robert, F.; Pilet, G.; Reber, C.; Luneau, D. Luminescence spectroscopy of europium(III) and terbium(III) penta-, octa- and nonanuclear clusters with *β*-diketonate ligands. *Dalton Trans.* **2009**, 6809–6815.

[35] Andrews, P. C.; Beck, T.; Forsyth, C. M.; Fraser, B. H.; Junk, P. C.; Massi, M.; Roesky, P. W. Templated assembly of a $\mu_6\text{-}CO_3^{2-}$ dodecanuclear lanthanum dibenzoylmethanide hydroxide cluster with concomitant formation of phenylglyoxylate. *Dalton Trans.* **2007**, 5651–5654.

[36] Andrews, P. C.; Deacon, G. B.; Gee, W. J.; Junk, P. C.; Urbatsch. Synthesis and characterization of thiophene-functionalised lanthanoid diketonate clusters with solvent-modulated europium luminescence. *Eur. J. Inorg. Chem*. **2012**, *2012*, 3273–3282.

[37] Thielemann, D. T.; Fernández, I.; Roesky, P. W. New amino acid ligated yttrium hydroxy clusters. *Dalton Trans.* **2010**, *39*, 6661–6666.

[38] Andrews, P. C.; Bousrez, G.; Junk, P. C.; Thielemann, T.; Werrett, M. V. Synthesis and characterisation of heterobimetallic lanthanoid O-based cluster/cages. *Eur. J. Inorg. Chem*. **2017**, 679–684.

[39] Xu, L-J.; Xu, G-T.; Chen, Z-N. Recent advances in lanthanide luminescence with metal-organic chromophores as sensitizers. *Coord. Chem. Rev*. **2014**, *273-274*, 47–62.

[40] a) Chen, R.; Hong, Z-F.; Zhao, Y-R.; Zheng, H.; Li, G-J.; Zhang, Q-C.; Kong, X-J.; Long, L-S.; Zheng, L-S. Ligand-dependent luminescence properties of lanthanide-titanium oxo clusters. *Inorg. Chem.* **2019**, *58*, 15008–15012. b) Shu, X-P.; Luo, W.; Wang, H-Y.; Fu, M-Y.; Zhu, Q-Y.; Dai, J. Eu-phen bonded titanium oxo-clusters, precursors for a facile preparation of high luminescent materials and films. *Inorg. Chem*. **2020**, *59*, 10422–10429. c) Wang, S.; Su, H-C.; Yu, L.; Zhao, X-W.; Qian, L-W.; Zhu, Q-Y.; Dai, J. Fluorescence and energy transfer properties of heterometallic lanthanide-titanium oxo clusters coordinated with anthracenecarboxylate ligands. *Dalton Trans.* **2015**, *44*, 1882–1888.

[41] Zhao, Y-R.; Zheng, H.; Che, L-Q.; Chen, H-J.; Kong, X-J.; Long, L-S.; Zheng, L-S. The effect on the luminescent properties in lanthanide-titanium oxo clusters. *Inorg. Chem*. **2019**, *58*, 10078–10083.

[42] Zheng, H.; Deng, Y-K.; Ye, M-Y.; Xu, Q-F.; Kong, X-J.;Long, L-S.; Zheng, L-S. Lanthanide-titanium oxo clusters as the luminescence sensor for nitrobenzene detection. *Inorg. Chem.* **2020**, *59*, 12404–12409.

[43] Lu, F-D.; Hong, Z-F.; Xie, J.; Kong, X-J.; Long, L-S.; Zheng, L-S. High-nuclearity lanthanide-titanium oxo clusters as molecular thermometers with high quantum yields. *Inorg. Chem.* **2017**, *56*, 12186–12192.

[44] Li, N.; Subramanian, G. S.; Matthews, P. D.; Xiao, J.; Chellappan, V.; Rosser, T. E.; Reisner, E.; Luo, H.-K.; Wright, D. S. Energy transfer and photoluminescence properties of lanthanide-containing polyoxotitanate cages coordinated by salicylate ligands. *Dalton Trans*. **2018**, *47*, 5679−5686.

[45] Andrews, P. C.; Brown, D. H.; Fraser, B. H.; Gorham, N. T.; Junk, P. C.; Massi, M.; St Pierre, T. G.; Skelton, B. W.; Woodward, R. C. Multifunctional hybrid materials based on transparent poly(methylmethacrylate) reinforced by lanthanoid hydroxo clusters. *Dalton Trans*. **2010**, *39*, 11227–11234.

[46] Hauser, C. P.; Thielemann, D. T.; Adlung, M.; Wickleder, C.; Roesky, P. W.; Weiss, C. K. Luminescent polymeric dispersions and films based on oligonuclear lanthanide clusters. *Macromol. Chem. Phys.* **2011**, *212*, 286–296.

[47] Knyazev, A. A.; Krupin, A. S.; Galyametdinov, Y. G. Luminescence behaviour of PMMA films doped with Tb(III) and Eu(III) complexes. *J. Lumin*. **2022**, *242*, 118609.

[48] Al Sabea, H.; Norel, L.; Galangau, O.; Roisnel, T.; Maury, O.; Riobé, F.; Rigaut, S. Efficient photomodulation of visible Eu(III) and invisible Yb(III) luminescences using DTE photochromic ligands for optical encryption. *Adv. Funct. Mater.* **2020**, *30*, 2002943.

[49] Shahi, P. K.; Singh, A. K.; Singh, S. K.; Rai, S. B.; Ullrich, B. Revelation of the technological versatility of the $Eu(TTA)_3Phen$ complex by demonstrating energy harvesting, ultraviolet light

detection, temperature sensing, and laser applications. *ACS Appl. Mater. Interfaces*. **2015**, *7*, 18231–18239.

[50] Feng, J.; Zhang, H. Hybrid materials based on lanthanide organic complexes: a review. *Chem. Soc. Rev.* **2013**, *42*, 387–410.

[51] Bünzli, J-C.; Comby, S.; Chauvin, A-S.; Vandevyver, C. D. B. New opportunities for lanthanide luminescence. *J. Rare Earth.* **2007**, *25*, 257–274.

[52] Cotton, S. *Lanthanides and Actinide Chemistry*, John Wiley & Sons Ltd, England, 2006.

[53] Sorace, L.; Gatteschi, D. Electronic Structure and Magnetic Properties of Lanthanide Molecular Complexes. In *Lanthanides and Actinides in Molecular Magnetism*; Layfield, R. A.; Murugesu, M., Ed.; Wiley-VCH Verlag GmbH & Co. KGaA, 2015; pp. 1–26.

[54] Bünzli, J-C.; Eliseeva, S. V. Basics of lanthanide photophysics. In *Lanthanide Luminescence: Photophysical, Analytical and Biological Aspects*; Hänninen, P.; Härmä, H., Ed.; Springer Berlin Heidelberg: Berlin, Heidelberg, Germany, Vol. 7, 2010; pp 1−45.

[55] Binnemans, K. Interpretation of europium(III) spectra. *Coord. Chem. Rev.* **2015***, 295*, 1–45.

[56] Weissman, S. I. Intramolecular energy transfer. The fluorescence of complexes of Europium. *J. Chem. Phys.* **1942**, *10*, 214–217.

[57] a) Ma, Y.; Wang, Y. Recent advances in the sensitized luminescence of organic europium complexes. *Coord. Chem. Rev.* **2010**, *254*, 972–990. b) Ward, M. D. Transition-metal sensitized near-infrared luminescence from lanthanides in d-f heteronuclear arrays. *Coord. Chem. Rev.* **2007**, *251*, 1663−1677.

[58] Latva, M.; Takalo, H.; Mukkala, V-M.; Matachescu, C.; Rodríguez-Ubis, J. C.; Kankare, J. Correlation between the lowest triplet state energy level of the ligand and lanthanide(III) luminescence quantum yield. *J. Lumin.* **1997***, 75*, 149–169.

[59] Crosby, G. A.; Whan, R. E.; Alire, R. M. Intramolecular Energy Transfer in Rare Earth Chelates. Role of the Triplet State. *J. Chem. Phys.* **1961***, 34*, 743–748.

[60] a) Mara, M. W.; Tatum, D. S.; March, A-M.; Doumy, G.; Moore, E. G.; Raymond, K. N. Energy transfer from antenna ligand to europium(III) followed using ultrafast optical and X-ray spectroscopy. *J. Am. Chem. Soc.* **2019**, *141*, 11071–11081. b) Ward, M. D. Mechanisms of sensitization of lanthanide(III)-based luminescence in transition metal/lanthanide and anthracene/lanthanide dyads. *Coord. Chem. Rev.* **2010**, *254*, 2634–2642.

[61] Bodman, S. E.; Butler, S. J. Advances in anion binding and sensing using luminescent lanthanide complexes. *Chem. Sci.* **2021**, *12*, 2716–2734.

[62] a) Kleinerman, M. Energy Migration in Lanthanide Chelates. *J. Chem. Phys.* **1969**, *51*, 2370–2381. b) Yang, C.; Fu, L.M.; Wang, Y.; Zhang, J. P.; Wong, W. T.; Ai, X.C.; Qiao, Y. F.; Zou, B. S.; Gui, L. L. A highly luminescent europium complex showing visible-light-sensitized red emission: direct observation of the singlet pathway. *Angew. Chemie Int. Ed.* **2004**, *43*, 5009–5013.

[63] Miyazaki, S.; Miyata, K.; Sakamoto, H.; Suzue, F.; Kitagawa, Y.; Hasegawa, Y.; Onda K. Dual energy transfer pathways from an antenna ligand to lanthanide ion in trivalent europium complexes with phosphine-oxide bridges. *J. Phys. Chem. A.* **2020**, *124*, 6601–6606.

[64] D'Aléo, A.; Pointillart, F.; Ouahab, L.; Andraud, C.; Maury, O. Charge transfer excited states sensitization of lanthanide emitting from the visible to the near-infra-red. *Coord. Chem. Rev.* **2012**, *256*, 1604–1620.

[65] Blasse, G.; Sabbatini, N. The quenching of rare-earth ion luminescence in molecular and non-molecular solids. *Mater. Chem. Phys.* **1987**, *16*, 237–252.

[66] Beeby, A.; Clarkson, I. M.; Dickins, R. S.; Faulkner, S.; Parker, D.; Royle, L.; de Sousa, A. S.; Williams, J. A. G.; Woods, M. Non-radiative deactivation of the excited states of europium, terbium and ytterbium complexes by proximate energy-matched OH, NH and CH oscillators: an improved luminescence for establishing solution hydration states. *J. Chem. Soc., Perkin Trans. 2.* **1999**, 493–504.

[67] Osawa, M.; Hoshino, M.; Wada, T.; Hayashi, F.; Osanai, S. Intra-complex energy transfer of europium(III) complexes containing anthracene and phenanthrene moieties. *J. Phys. Chem. A.* **2009**, *113*, 10895–10902.

[68] Parker, D.; Fradgley, J. D.; Wong, K-L. The design of responsive luminescent lanthanide probes and sensors. *Chem. Soc. Rev.* **2021**, *50*, 8193–8213.

[69] a) Beeby, A.; Faulkner, S.; Parker, D.; Williams, J. A. G. Sensitised luminescence from phenanthridine appended lanthanide complexes: analysis of triplet mediated energy transfer processes in terbium, europium and neodymium complexes. *J. Chem. Soc. Perkin Trans. 2*. **2001**, 1268–1273. b) Barry, D. E.; Caffrey, D. F.; Gunnlaugsson, T. Lanthanide-directed synthesis of luminescent self-assembly supramolecular structures and mechanically bonded systems from acyclic coordinating organic ligands. *Chem. Soc. Rev.* **2016**, *45*, 3244–3274.

[70] Kovacs, D.; Mathieu, E.; Kiraev, S. R.; Wells, J. A. L.; Demeyere, E.; Sipos, A.; Borbas, E. Coordination environment-controlled photoinduced electron transfer quenching in luminescent europium complexes. *J. Am. Chem. Soc.* **2020**, *142*, 13190–13200.

[71] Parker, D.; Fradgley, J. D.; Delbianco, M.; Starck, M.; Walton, J. W.; Zwier, J. M. Comparative analysis of lanthanide excited state quenching by electronic energy and electron transfer processes. *Faraday Discuss.* **2022**, *234*, 159–174.

[72] Hasegawa, Y.; Wada, Y.; Yanagida, S. Strategies for the design of luminescent lanthanide(III) complexes and their photonic applications. *J. Photochem. Photobiol. C: Photochem. Rev.* **2004**, *5*, 183–202.

[73] Bünzli, J-C. On the design of highly luminescent lanthanide complexes. *Coord. Chem. Rev.* **2015**, *293-294*, 19–47.

[74] Sabbatini, N.; Guardigli, M.; Manet, I.; Ungaro, R.; Casnati, A.; Ziessel, R.; Ulrich, G.; Asfari, Z.; Lehn, J-M. Lanthanide complexes of encapsulating ligands: luminescent devices at the molecular level. *Pure & Appl. Chem.* **1995**, *67*, 135–140.

[75] Janicki, R.; Mondry, A.; Starynowics, P. Carboxylates of rare earth elements. *Coord. Chem. Rev.* **2017**, *340*, 98–133.

[76] Petoud, S.; Cohen, S. M.; Bünzli, J-C. G.; Raymond, K. N. Stable lanthanide luminescence agents highly emissive in aqueous solution: multidentate 2-hydroxyisophthalamide complexes of Sm^{3+}, Eu^{3+}, Tb^{3+} Dy^{3+}. *J. Am. Chem. Soc.* **2003**, *125*, 13324–13325.

[77] Nehra, K.; Dalal, A.; Hooda, A.; Bhagwan, S.; Saini, R. K.; Mari, B.; Kumar, S.; Singh, D. Lanthanides β-diketonate complexes as energy-efficient emissive materials: a review. *J. Mol. Struct*. **2022**, *1249*, 131531.

[78] De Sá, G. F.; Malta, O. L.; de Mello Donegá, C.; Simas, A. M.; Longo, R. L.; Santa-Cruz, P. A.; da Silva Jr., E. F. Spectroscopic properties and design of highly luminescent lanthanide coordination complexes. *Coord. Chem. Rev*. **2000**, *196*, 165–195.

[79] Lima, N. B. D.; Gonçalves, S. M. C.; Júnior, S. A.; Simas, A. M. A comprehensive strategy to boost the quantum yield of luminescence of europium complexes. *Sci Rep.* **2013**, *3*, 2395.

[80] Yang, C.; Fu, L-M.; Wang, Y.; Zhang, J-P.; Wong, W-T.; Ai, X-C.; Qiao, Y-F.; Zou, B-S.; Gui, L-L. A highly luminescent europium complex showing visible-light-sensitized red emission: direct observation of the singlet pathway. *Angew. Chem. Int. Ed.* **2004**, *43*, 5010–5013.

[81] Zhang, K.; Zhang, X.; Zhou, J.; Fu, G.; He, Y.; Li, B.; Lü, X. Luminescence homoleptic cyclic tetranuclear $[Ln_4(BTFA)_{10}(\mu_3\text{-}OH)_2(H_2O)_4]$ complexes (Ln = Eu or Tb). *Inorg. Chem. Commun*. **2018**, *95*, 139–143.

[82] Arrué, L.; Santoyo-Flores, J.; Pizarro, N.; Zarate, X.; Páez-Hernández, D.; Schott, E. The role played by structural and energy parameters of β-diketones derivatives as antenna ligands in Eu(III) complexes. *Chem. Phys. Lett.* **2021**, *773*, 138600.

[83] a) Babetto, L.; Carlotto, S.; Carlotto, A.; Rancan, M.; Bottaro, G.; Armelao, L.; Casarin, M. Antenna triplet DFT calculations to drive the design of luminescent Ln^{3+} complexes. *Dalton Trans.* **2020**, *49*, 14556–14563. b) Carlotto, S.; Babetto, L.; Rancan, M.; Bottaro, G.; Casarin, M.; Armelao, L. How to get deeper insights into the optical properties of lanthanide systems: a computational protocol from ligand to complexes. *Pure Appl. Chem.* **2023**, *95*, 671–682.

[84] Bünzli, J-C. G.; Piguet, C. Taking advantage of luminescent lanthanide ions. *Chem. Soc. Rev.* **2005**, *34*, 1048–1077.

[85] Heffern, M. C.; Matosziuk, L. M.; Meade, T. J. Lanthanide probes for bioresponsive imaging. *Chem. Rev.* **2014**, *114*, 4496–4539.

[86] Aigouy, L.; Tessier, G.; Mortier, M.; Charlot, B. Scanning thermal imaging of microelectronic circuits with a fluorescent nanoprobe. *Appl. Phys. Lett*. **2005**, *87*, 184105.

[87] Brites, D. S.; Balabhadra, S.; Carlos, L. D. Lanthanide-based thermometers: at the cutting-edge of luminescence thermometry. *Adv. Optical. Mater*. **2018**, 1801239.

[88] Brites, C. D. S.; Lima, P. P.; Silva, N. J. O.; Millán, A.; Amaral, V. S.; Palacio, F.; Carlos, L. D. Thermometry at the nanoscale. *Nanoscale.* **2012**, *4*, 4799–4829.

[89] Miyagawa, T.; Fujie, T.; Ferdinandus, Doan, T. T. V.; Sato, H.; Takeoka, S. Glue-Free Stacked Luminescent Nanosheets Enable High-Resolution Ratiometric Temperature Mapping in Living Small Animals. *ACS Appl. Mater. Interfaces.* **2016**, *8*, 33377–33385.

[90] Jaque, D.; Vetrone, F. Luminescence nanothermometry. *Nanoscale.* **2012**, *4*, 4301–4326.

[91] Wang, X-d.; Wolfbeis, O. S.; Meier, R. J. Luminescent probes and sensors for temperature. *Chem. Soc. Rev.* **2013**, 42, 7834–7869.

[92] Uchiyama, S.; Kawai, N.; de Silva, A. P.; Iwai, K. Fluorescent polymeric AND logic gate with temperature and pH as inputs. *J. Am. Chem. Soc*. **2004**, *126*, 3032–3033.

[93] Brites, C. D. S.; Millán, A.; Carlos, L. D. Lanthanides in luminescent thermometry. In *Handbook on the physics and chemistry of rare earths*; Bünzli, J-C., Pecharsky, V. K., Ed.; Elsevier, Vol.49, 2016; pp. 339–427.

[94] Katagiri, S.; Manseki, K.; Tsukahara, Y.; Mitsuo, K.; Wada, Y. Luminescent polymer film containing tetranuclear Eu(III) complex as temperature-sensing device. *J. Alloys Compd*. **2008**, *453*, L1–L3.

[95] Basu, B. B. J.; Vasantharajan, N. Temperature dependence of the luminescence lifetime of a europium complex immobilized in different polymer matrices. *J. Lumin.* **2008**, *128*, 1701–1708.

[96] Carlotto, A.; Babetto, L.; Carlotto, S.; Miozzi, M.; Seraglia, R.; Casarin, M.; Bottaro, G.; Ranca, M.; Armelao, L. Luminescent thermometers: from a library of Eu(III)-β-diketonates to a general model for predicting the thermometric behaviour of europium-based coordination systems. *ChemPhotoChem*. **2020**, *4*, 674–684.

[97] Bellucci, L.; Bottaro, G.; Labella, L.; Marchetti, F.; Samaritani, S.; Belli Dell'Amico, D.; Armelao, L. 1D-Zigzag Eu^{3+}/Tb^{3+} coordination chains as luminescent ratiometric thermometers endowed with multicolour emission. *Materials.* **2021**, *14*, 6445.

[98] Nexha, A.; Carvajal, J. J.; Pujol, M. C.; Díaz, F.; Aguiló, M. Lanthanide doped luminescence nanothermometers in the biological windows: strategies and applications. *Nanoscale.* **2021**, *13*, 7913–7987.

[99] Kolodner, P.; Tyson, J. A. Remote thermal imaging with 0.7-μm spatial resolution using temperature-dependent fluorescent thin films. *Appl. Phys. Lett.* **1983**, *42*, 117–119.

[100] Hasegawa, Y.; Kitagawa, Y. Thermo-sensitive luminescence of lanthanide complexes, clusters, coordination polymers and metal–organic frameworks with organic photosensitizers. *J. Mater. Chem. C.* **2019**, *7*, 7494–7511.

[101] Katagiri, S.; Tsukahara, Y.; Hasegawa, Y.; Wada, Y. Energy-transfer mechanism in photoluminescent Terbium(III) complexes causing their temperature-dependence. *Bull. Chem. Soc. Jpn.* **2007**, *80*, 1492–1503.

[102] Khalil, G. E.; Lau, K.; Phelan, G. D.; Carlson, B.; Gouterman, M.; Callis, J. B.; Dalton, L. R. Europium beta-diketonate temperature sensors: effects of ligands, matrix, and concentration. *Rev. Sci. Instrum.* **2004**, 75, 192–206.

[103] Sato, S.; Wada, M. Relations between intramolecular energy transfer efficiencies and triplet energies in rare earth β-diketone chelates. *Bull. Chem. Soc. Jpn*. **1970**, *43*, 1955–1962.

[104] Rocha, J.; Brites, C. D. S.; Carlos, L. D. Lanthanide organic framework luminescent thermometers. *Chem. Eur. J*. **2016**, *22*, 14782–14795.

[105] Guo, X-Q.; Zhou, L-P.; Cai, L.X.; Sun, Q-F. Self-assembled bright luminescent lanthanide-organic polyhedra for ratiometric temperature sensing. *Chem. Eur. J*. **2018**, *24*, 6936–6940.

[106] Liu, X.; Akerboom, S.; de Jong, M.; Mutikainen, I.; Tanase, S.; Meikerink, A.; Bouwman, E. Mixed-lanthanoid metal-organic framework for ratiometric cryogenic temperature sensing. *Inorg. Chem.* **2015**, *54*, 11323–11329.

[107] Cui, Y.; Zou, W.; Song, R.; Yu, J.; Zhang, W.; Yang, Y.; Qian, G. A ratiometric and colorimetric luminescent thermometer over a wide temperature range based on a lanthanide coordination polymer. *Chem. Commun.* **2014**, *50*, 719–721.

[108] Miyata, K.; Konno, Y.; Nakanishi, T.; Kobayashi, A.; Kato, M.; Fushimi, K.; Hasegawa, Y. Chamaleon luminophore for sensing temperatures: control of metal-to-metal and energy back transfer in lanthanide coordination polymers. *Angew. Chem. Int. Ed.* **2013**, *52*, 1–5.

[109] Li, X-Y.; Jing, Y.; Zheng, J.; Ding, H.; Li, Q.; Yu, M-H.; Bu, X-H. Two luminescent high-nuclearity lanthanide clusters Ln_{48} (Ln = Eu and Tb) with a nanopillar structure. *Cryst. Growth Des*. **2020**, *20*, 5294–5301.

[110] Liu, W-D.; Li, G-J.; Xu, H.; Du, M-H.; Long, L-S.; Zheng, L-S.; Kong, X-J. Photoluminescence of lanthanide-titanium-oxo clusters Eu_9Ti_2 and Tb_9Ti_2 based on β-diketone ligand. *Inorg. Chem.* **2022**, *61*, 9849–9854.

[111] Meng, F.; Liu, W-D.; Li, G-J.; Deng, J.; Kong, X-J. Synthesis, structure and luminescence characterizations of pyramid-like lanthanide-titanium-oxo clusters $EuTi_9$ and $TbTi_9$. *Inorg. Chem. Commun*. **2022**, *141*, 109565.

[112] Monge, A.; D'Vries, R. F.; Snejko, N.; de Andres, A.; Gutierrez-Puebla, E.; Alvarez, S.; Bausa, L. Multimetal rare-heart MOFs for lighting and thermometry: tailoring color and optimal temperature range through enhanced disulfobenzoic triplet phosphorescence. *J. Mater. Chem. C.* **2013**, *1*, 6316–6324.

[113] Kolodner, P.; Tyson, J. A. Microscopic fluorescent imaging of surface temperature profiles with 0.01 °C resolution *Appl. Phys. Lett.* **1982**, *40*, 782–784.

[114] Stich, M. I. J.; Nagl, S.; Wolfbeis, O. S.; Henne, U.; Schaeferling, M. A dual luminescent sensor material for simultaneous imaging of pressure and temperature on surfaces. *Adv. Funct. Mater*. **2008**, *18*, 1399–1406.

[115] Green, M. A.; Dunlop, E. D.; Hohl-Ebinger, J.; Yoshita, M.; Kopidakis, N.; Hao, X. Solar cell efficiency tables (version 57) *Prog. Photovolt. Res. Appl*. **2021**, *29*, 3–15.

[116] Ghosh, A. Potential of building integrated and attached/applied photovoltaic (BIPV/BAPV) for adaptive less energy-hungry building's skin: A comprehensive review. *J. Clean. Prod*. **2020**, *276*, 123343.

[117] Castelletto, S.; Boretti, A. Luminescence solar concentrators: a technology update. *Nano Energy.* **2023**, *109*, 108269.

[118] Daigle, Q.; O'Brien, P. G. Heat generated using luminescent solar concentrators for building energy applications. *Energies,* **2020**, *13*, 5574.

[119] Correia, S. F. H.; de Zea Bermudez, V.; Ribeiro, S. J. L.; André, P. S.; Ferreira, R. A. S.; Carlos, L. D. Luminescent solar concentrators: Challenges for lanthanide-based organic-inorganic hybrid materials. *J. Mater. Chem. A* **2014***, 2*, 5580–5596.

[120] Batchelder, J. S.; Zewail, A. H.; Cole, T. Luminescent solar concentrators. 1: Theory of operation and techniques for performance evaluation. *Appl. Opt.* **1979***, 18*, 3090–3110.

[121] Meinardi, F.; Bruni, F.; Brovelli, S. Highly efficient luminescent solar concentrators based on earth-abundant indirect-bandgap silicon quantum dots. *Nat. Photonics* **2017***, 11*, 177–185.

[122] Purcell-Milton, F. Gun'ko, Y. K. Quantum dots for Luminescent Solar Concentrators. *J. Mater. Chem.* **2012***, 22*, 16687–16697.

[123] a) Hernández-Rodríguez, M. A.; Correia, S. F. H.; Ferreira, R. A. S.; Carlos, L. D. A perspective on sustainable luminescent solar concentrators. *J. Appl. Phys.* **2022**, *131*, 140901. b) Arrigo, A.; Gangemi, C. M. A.; Barattucci, A.; Bonaccorsi, P. M.; Greco, V.; Giuffrida, A.; Genovese, S.; Campagna, S.; Nastasi, F.; Puntoriero, F. Highly efficient luminescent solar concentrators based on BODIPY derivatives. *Adv. Mater. Interfaces*. **2024**, *11*, 2400114.

[124] Wang, X.; Wang, T.; Tian, X.; Wang, L.; Wu, W.; Luo, Y.; Zhang, Q. Europium complex doped luminescent solar concentrators with extended absorption range from UV to visible region. *Solar Energy*. **2011**, *85*, 2179–2184.

[125] Yang, C.; Zhang, J.; Peng, W-T.; Sheng, W.; Liu, D.; Kuttipillai, P. S.; Young, M.; Donahue, M. R.; Levine, B. G.; Borhan, B.; Lunt, R. R. Impact of stokes shift on the performance of near-infrared harvesting transparent luminescent solar concentrators. *Sci. Rep.* **2018***, 8*, 1–10.

[126] Griffini, G. Host matrix materials for luminescent solar concentrators: recent achievements and forthcoming challenges. *Front. Mater.* **2019***, 6*, 1–8.

[127] Wang, T.; Zhang, J.; Ma, W.; Luo, Y.; Wang, L.; Hu, Z.; Wu, W.; Wang, X.; Zou, G.; Zhang, Q. Luminescent solar concentrator employing rare earth complex with zero self-absorption loss. *Sol. Energy.* **2011**, *85*, 2571–2579.

[128] Li, Y.; Zhang, X.; Zhang, Y.; Dong, R.; Luscombe, C. K. Review on the role of polymers in luminescent solar concentrators. *J. Polym. Sci. Part A Polym. Chem.* **2019***, 57*, 201–215.

[129] Shahi, P. K.; Singh, P.; Rai, S. B. Sunlight activated lanthanide complex for luminescent solar collector applications: effect of waveguide matrix. *J. Phys. D: Appl. Phys.* **2017**, *50*, 075501.

[130] Motta, I.; Bottaro, G.; Rando, M.; Rancan, M.; Seraglia, R.; Armelao, L. Transparent and colour-neutral luminescent solar concentrators using bright Eu^{3+} supramolecular cages towards photovoltaic windows. *J. Mater. Chem. A.* **2024**, *12*, 22516–22527.

[131] Bagherzadeh-Khajehmarjan, E.; Nikniazi, A.; Olyaeefar, B.; Ahmadi-Kandjani, S.; Nunzi, J. M. Bulk luminescent solar concentrators based on organic-inorganic $CH_3NH_3PbBr_3$ perovskite fluorophores. *Sol. Energy Mater. Sol. Cells.* **2019***, 192*, 44–51.

[132] Roncali, J. Luminescent solar concentrators: quo vadis? Adv. Energy Mater. 2020, 10, 2001907.

[133] Ferreira, R. A. S.; Correia, S. F. H.; Georgieva, P.; Fu, L.; Antunes, M.; André, P. S. A comprehensive dataset of photonic features on spectral converters for energy harvesting. Sci. *Data.* **2024**, *11*.

[134] Kim, K.; Nam, S. K.; Cho, J.; Moon, J. H. Photon upconversion-assisted dual-band luminescence solar concentrators coupled with perovskite solar cells for highly efficient semi-transparent photovoltaic systems. *Nanoscale.* **2020**, *12*, 12426–12431.

[135] Zhang, B.; Lyu, G. Kelly, E. A.; Evans, R. C. Förster resonance energy transfer in luminescent solar concentrators. *Adv. Sci.* **2022**, *9*, 2201160–2201186.

[136] Devi, R.; Rajendran, M.; Singh, K.; Pal, R.; Vaidyanathan, S. Smart luminescent molecular europium complexes and their versatile applications. *J. Mater. Chem. C.* **2021**, *9*, 6618–6633.

[137] Andres, J.; Hersch, R. D.; Moser, J-E.; Chauvi, A-S. A new anti-counterfeiting feature relying on invisible luminescent full color images printed with lanthanide-based inks. *Adv. Funct. Mater.* **2014**, *24*, 5029–5036.

[138] Zanella, S.; Hernández-Rodríguez, M. A.; Ferreira, R. A. S.; Brites, C. D. S. Lanthanide-based logic: a venture for the future of molecular computing. *Chem. Commun*. **2023**, *59*, 7863–7874.

[139] Pilch, M.; Ortyl, J.; Chachaj-Brekiesz, A.; Galek, M.; Popielarz, R. Europium-based luminescent sensors for mapping pressure distribution on surfaces. *Sens. Actuators B Chem.* **2020**, *305*, 127409.

[140] Spangler, C., Schäferling, M. Luminescent Chemical and Physical Sensors Based on Lanthanide Complexes. In *Lanthanide Luminescence. Springer Series on Fluorescence*; Hänninen, P., Härmä, H., Ed.; Springer, Berlin, Heidelberg, Vol. 7, 2010; pp. 235–262.

[141] Reinders, A.; Kishore, R.; Slooff, L.; Eggink, W. Luminescent solar concentrator photovoltaic designs. *Jpn. J. Appl. Phys*. **2018**, *57*, 08RD10-1–08RD10-10.

[142] Yang, C.; Xu, J.; Ma, J.; Zhu, D.; Zhang, Y.; Liang, L.; Lu, M. The effect of two additional Eu^{3+} luminophors in two novel trinuclear europium complexes on their photoluminescent properties. *Photochem. Photobiol. Sci*. **2013**, *12*, 330–338.

[143] Zhao, Y.; Lunt, R. R. Transparent luminescent solar concentrators for large-area solar windows enabled by massive Stokes-shift nanocluster phosphors. *Adv. Energy Mater.* **2013**, *3*, 1143–1148.

[144] Liu, W-D.; Li, G-J.; Xu, H.; Deng, Y-K.; Du, M-H.; Long, L-S.; Zheng, L-S.; Kong, X-J. Circularly polarized luminescence and performance modulation of chiral europium-titanium (Eu_2Ti_4)-oxo clusters. *Chem. Commun.* **2023**, *59*, 346–349.

[145] Sukhikh, T. S.; Kolybalov, D. S.; Pylova, E. K.; Bashirov, D. A.; Komarov, V. Y.; Kuratieva, N. V.; Smolentsev, A. I.; Fitch, A. N.; Konchenko, S. N. A fresh look at the structural diversity of dibenzoylmethanide complexes of lanthanides. *New J. Chem.* **2019**, *43*, 9934–9942.

[146] Li, X-L.; Zhu, C.; Zhang, X-L.; Hu, M.; Wang, A-L.; Xiao, H-P. Two lanthanide-hydroxo clusters with different nuclearity: synthesis, structures, luminescent and magnetic properties. *J. Mol.Struct.* **2017**, *1128*, 30–35.

[147] Sukhikh, T. S.; Bashirov, D. A.; Kuratieva, N. V.; Smolentsev, A. I.; Konchenko, S. N. Crysyal structures of $[Ln_5(dbm)_{10}(OH)_5]\cdot n CH_2Cl_2$ (Ln = Yb, n = 2, Ln = Er, n = 6). *J. Struct. Chem.* **2014**, *55*, 1437–1441.

[148] Chen, R.; Chen, C-L.; Zhang, H.; Wang, Z-H.; Sun, F-L.; Du, M-H.; Zhuang, G-L.; Wang, C.; Long, L-S.; Zheng, L-S.; Kong, X-J. Molecular solid solution of lanthanide-titanium-oxo clusters with enhanced photocatalytic hydrogen evolution. *Sci China Chem.* **2024**, *67*, 529–535.

[149] Jiang, X.; Wu, Y.; He, C. Rare earth dibenzoylmethane complexes for potential application as high-density recordable optical recording materials. *Mater. Lett.* **2008**, *62*, 286–288.

[150] a) Wang, D.; Pi, Y.; Zheng, C.; Fan, L.; Hu, Y.; Wei, X. Preparation and photoluminescence of some europium (III) ternary complexes with β-diketone and nitrogen heterocyclic ligands. *J. Alloys Compd.* **2013**, *574*, 54–58. b) Singh, D.; Bhagwan, S.; Dalal, A.; Nehra, K.; Saini, R. K.; Singh, K.; Simantilleke, A. P.; Kumar, S.; Singh, I. Oxide ancillary ligand-based europium β-diketonate complexes and their enhanced luminosity. *Rare Met.* **2021**, *40*, 2873–2881.

[151] Hasan, N.; Iftikhar, K. Synthesis, crystal structure and photoluminescence studies of $[Eu(dbm)_3(impy)]$ and its polymer-based hybrid film. *New J. Chem.* **2019**, *43*, 2479–2489.

[152] Campello, M. P. C.; Palma, E.; Correia, I.; Paulo, P. M. R., Matos, A.; Rino, J.; Coimbra, J.; Pessoa, J. C. Gambino, D.; Paulo, A.; Marques, F. Lanthanide complexes with phenanthroline-based ligands: insights into mechanisms of cell death by imaging tools. *Dalton Trans.* **2019**, *48*, 4611–4624.

[153] a) Andreeva, A. Y.; Sukhikh, T. S.; Kozlova, S. G.; Konchenko, S. N. Exchange interactions and XPS O1s spectra in polynuclear lanthanide complexes with dibenzoylmethanide and 4-hydroxy-2,1,3-benzothiadiazole. *J. Mol. Struct.* **2018**, *1166*, 190–194. b) Korochentsev, V. V.; Vovna, V. I.; Kalinovskaya, I. V.; Komissarov, A. A.; Dotsenko, A. A.; Shurygin, A. V.; Mirochnik, A. G.; Sergienko, V. I. Electronic structure of tris-dibenzoylmethanates of Sc, Y, La rare-earth elements from the results of studies by X-ray photoelectron spectroscopy and density functional theory. *J. Struct. Chem.* **2014**, *55*, 1057–1066.

[154] Moulder, J. F.; Stickle, W. F.; Sobol P. W.; Bomben, K. D. *Handbook of X-ray Photoelectron Spectroscopy*, Perkin-Elmer, Eden Prairie, MN, 1992.

[155] Briggs, D.; Seah, M. *Practical Surface Analysis*, Wiley: Chichester, 1990.

[156] Mercier, F.; Alliot, C.; Bion, L.; Thromat, N.; Toulhoat, P. XPS study of Eu(III) coordination compounds: core levels binding energies in solid mixed-oxo-compounds $Eu_mX_xO_y$. *J. Electron Spectros. Relat. Phenomena.* **2006**, *150*, 21–26.

[157] Shukla, P.; Sudarsan, V.; Vatsa, R. K.; Nayak, S. K.; Chattopadhyay, S. Effect of symmetric substitution on the phenyl groups of Eu^{3+}-dibenzoylmethane complexes on their luminescence properties. *J. Lumin.* **2010**, *130*, 1952–1957.

[158] Li, H-F.; Li, G-M.; Chen, P.; Sun, W-B.; Yan, P-F. Highly luminescent lanthanide complexes with novel bis-*β*-diketone ligand: synthesis, characterization and photoluminescent properties. *Spectrochim. Acta A Mol. Biomol. Spectrosc.* **2012**, *97*, 197–201.

[159] Debije, M. G.; Evans, R. C.; Griffini, G. Laboratory protocols for measuring and reporting the performance of luminescent solar concentrators. *Energy Environ. Sci.* **2021**, *14*, 293–301.

[160] Motta, I. Tesi di Laurea Magistrale. *Design and development of lanthanoid-based luminescent solar concentrators.* Università degli Studi di Padova, 2021.

[161] Wilson, L. R.; Rowan, B. C.; Robertson, N.; Moudam, O.; Jones, A. C.; Richards, B. S. Characterization and reduction of reabsorption losses in luminescent solar concentrators. *Appl. Opt.* **2010**, *49*, 1651–1661.

[162] Kaliramna, S.; Dhayal, S. S.; Kumar, N. Fabrication of PMMA thin film and its optical and photocatalytic activity. *Mater. Today Proc*. **2022**, *69*, 42–46.

[163] Roitershtein, D. M.; Puntus, L. N.; Lyssenko, K. A.; Taidakov, I. V.; Varaksina, E. A.; Minyaev, M. E.; Gerasin, V. A.; Guseva, M. A.; Vinogradov, A. A.; Savchenko, M. S.; Nifant'ev, I. E. An efficient route for design of luminescent composite materials based on polyethylene containing europium dibenzoylmethanate. *New J. Chem.* **2017**, *41*, 13663–13672.

[164] El-Kalla, E. H.; Sayyah, S. M.; Afifi, H. H.; Saeed, A. F. Ultraviolet-visible spectroscopic studies of poly(methyl methacrylate) doped with some luminescent materials. *Acta Polym. 1989,* **40**, 349–351.

[165] Mano, E. B.; Durao, L. A. Review of laboratory methods for the preparation of polymer films. *J. Chem. Educ. 1973,* **50**, 228–232.

[166] Richardson, F. Terbium(III) and europium(III) ions as luminescent probes and strains for biomolecular systems. *Chem. Rev.* **1982**, *82*, 541–552.

[167] Singh, A. K.; Singh, S. K.; Mishra, H.; Prakash, R.; Rai, S. B. Structural, thermal, and fluorescence properties of $Eu(DBM)_3Phen_x$ complex doped in PMMA. *J. Phys. Chem. B* **2010**, *114*, 13042–13051.

[168] Knyazev, A. A.; Krupin, A. S.; Galyametdinov, Y. G. Luminescence behaviour of PMMA films doped with Tb(III) and Eu(III) complexes. *J. Lum.* **2022**, *242*, 118609.

[169] Shehata, A.; Ali, M.; Schuch, R.; Mohamed, T. Experimental investigations of nonlinear optical properties of soda-lime glasses and theoretical study of self-compression of fs laser pulses. *Opt. Laser Technol.* **2019**, *116*, 276–283.

[170] Bellucci, L.; Bottaro, G.; Labella, L.; Causin, V.; Marchetti, F.; Samaritani, S.; Belli Dell'Amico, D.; Armelao, L. Composition-thermometric properties correlations in homodinuclear Eu^{3+} luminescent complexes. *Inorg. Chem.* **2020**, *59*, 18156–18167.

[171] Warner, T.; Ghiggino, K. P.; Rosengarten, G. A critical analysis of luminescent solar concentrator terminology and efficiency results. *J. Sol. Energy.* **2022**, *246*, 119–140.

[172] Yang, C.; Liu, D.; Bates, M.; Barr, M. C.; Lunt, R. R. How to accurately report transparent solar cells. *Joule.* **2019**, *3*, 1803–1809.

[173] Traverse, C. J.; Pandey, R.; Barr, M. C.; Lunt, R. R. Emergence of highly transparent photovoltaics for distributed applications. *Nat. Energy.* **2017**, *2*, 849–860.

[174] Yang, C.; Barr, M. C.; Lunt, R. R. Analysis of the aesthetics of semitransparent, colorful, and transparent luminescent solar concentrators. *Phys. Rev. Applied.* **2022**, *17*, 0340054-1–17.

[175] Ostos, F. J.; Iasilli, G.; Carlotti, M.; Pucci, A. High-performance luminescent solar concentrators based on poly(cyclohexylmethacrylate) (PCHMA) films. *Polymers*. **2020**, *12*, 2898.

[176] https://www.pveducation.org (Appendix, Paragraph V. Last access: September 2024).

[177] Dittrich, T. Basic Characteristics and Characterization of Solar Cells. in *Materials Concepts for Solar Cells.* **2018***,* 3–43.